10:34:57 OCA PAD AMENDMENT - PROJECT HEADER INFORMATION 10/02/95

Active

Project #: E-25-X49 Cost share #: Rev #: 6
Center # : 10/24-6-R7619-0A0 Center shr #: OCA file #:
Work type : RES
Contract#: F49620-92-J-0518 Mod #: P00003 Document : GRANT
Prime #: Contract entity: GTRC

Subprojects ? : N CFDA: 12.800
Main project #: PE #: 61102F

Project unit: MECH ENGR Unit code: 02.010.126
Project director(s):
GLEZER A MECH ENGR (404)894-3262

Sponsor/division names: AIR FORCE / BOLLING AFB, DC
Sponsor/division codes: 104 / 001

Award period: 920915 to 960229 (performance) 960430 (reports)

| Sponsor amount | New this change | Total to date |
|---|---|---|
| Contract value | 0.00 | 364,867.00 |
| Funded | 0.00 | 364,867.00 |
| Cost sharing amount | | 0.00 |

Does subcontracting plan apply ?: Y

Title: NOVEL DIAGNOSTIC TECHNIQUES & ACTUATOR TECHNOLOGY FOR TURBULENT SHEAR FLOWS

PROJECT ADMINISTRATION DATA

OCA contact: Anita D. Rowland 894-4820

Sponsor technical contact

DR. JAMES M. MCMICHAEL
(202)767-4987

AFOSR/NA
110 DUNCAN AVENUE
SUITE B115
BOLLING AFB, DC 20332-0001

Sponsor issuing office

JENNIFER K. BELL
(202)404-4064

AFOSR/PKA
110 DUNCAN AVENUE
SUITE B115
BOLLING AFB, DC 20332-0001

Security class (U,C,S,TS) : U ONR resident rep. is ACO (Y/N): N
Defense priority rating : NA NA supplemental sheet
Equipment title vests with: Sponsor GIT X
TITLE <5,000 WITH GIT AT ACQUISITION.
Administrative comments -
P-3 AWARDS A NCE THRU 2.29.96

GEORGIA INSTITUTE OF TECHNOLOGY
OFFICE OF CONTRACT ADMINISTRATION

NOTICE OF PROJECT CLOSEOUT

Closeout Notice Date 08/05/96

Project No. E-25-X49 Center No. 10/24-6-R7619-0A0

Project Director GLEZER A School/Lab MECH ENGR

Sponsor AIR FORCE/BOLLING AFB, DC

Contract/Grant No. F49620-92-J-0518 Contract Entity GTRC

Prime Contract No. _____

Title NOVEL DIAGNOSTIC TECHNIQUES & ACTUATOR TECHNOLOGY FOR TURBULENT SHEAR FLO

Effective Completion Date 960229 (Performance) 960430 (Reports)

| Closeout Actions Required: | Y/N | Date Submitted |
|---|---|---|
| Final Invoice or Copy of Final Invoice | Y | |
| Final Report of Inventions and/or Subcontracts | Y | |
| Government Property Inventory & Related Certificate | N | |
| Classified Material Certificate | N | |
| Release and Assignment | N | |
| Other _____ | N | |

Comments_____

Subproject Under Main Project No. _____

Continues Project No. _____

Distribution Required:

| | |
|---|---|
| Project Director | Y |
| Administrative Network Representative | Y |
| GTRI Accounting/Grants and Contracts | Y |
| Procurement/Supply Services | Y |
| Research Property Managment | Y |
| Research Security Services | N |
| Reports Coordinator (OCA) | Y |
| GTRC | Y |
| Project File | Y |
| Other _____ | N |
| _____ | N |

NOTE: Final Patent Questionnaire sent to PDPI.

SECURITY CLASSIFICATION OF THIS PAGE

# REPORT DOCUMENTATION PAGE

| | |
|---|---|
| 1a. REPORT SECURITY CLASSIFICATION: Unclassified | 1b. RESTRICTIVE MARKINGS |
| 2a. SECURITY CLASSIFICATION AUTHORITY | 3. DISTRIBUTION/AVAILABILITY OF REPORT: Approved for public release; distribution is unlimited |
| 2b. DECLASSIFICATION/DOWNGRADING SCHEDULE | |
| 4. PERFORMING ORGANIZATION REPORT NUMBER(S): Annual Technical 1 | 5. MONITORING ORGANIZATION REPORT NUMBER(S) |
| 6a. NAME OF PERFORMING ORGANIZATION: GTRC; 6b. OFFICE SYMBOL (If applicable) | 7a. NAME OF MONITORING ORGANIZATION: AFOSR |
| 6c. ADDRESS (City, State and ZIP Code): Atlanta, GA 30332 | 7b. ADDRESS (City, State and ZIP Code): AFOSR/NA Bldg. 410, Bolling AFB, DC 20332-6440 |
| 8a. NAME OF FUNDING/SPONSORING ORGANIZATION: AFOSR; 8b. OFFICE SYMBOL (If applicable) | 9. PROCUREMENT INSTRUMENT IDENTIFICATION NUMBER: F4962092J0518 |
| 8c. ADDRESS (City, State and ZIP Code): AFOSR/NA Bldg. 410, Bolling AFB DC 20332-6440 | 10. SOURCE OF FUNDING NOS. |

| PROGRAM ELEMENT NO. | PROJECT NO. | TASK NO. | WORK UNIT NO |
|---|---|---|---|
| PE-61102F | PR-2307 | SA-BS | G-AFOSR F4962092 J0518 |

11. TITLE (Include Security Classification): Novel Diagnostic Techniques & Actuator Technology for Turbulent Shear Flows

12. PERSONAL AUTHOR(S): A. Glezer

| 13a. TYPE OF REPORT | 13b. TIME COVERED | 14. DATE OF REPORT (Yr., Mo., Day) | 15. PAGE COUNT |
|---|---|---|---|
| Annual Progress | FROM Sept 92 TO Sept 93 | | |

16. SUPPLEMENTARY NOTATION

| 17. COSATI CODES | | | 18. SUBJECT TERMS (Continue on reverse if necessary and identify by block number) |
|---|---|---|---|
| FIELD | GROUP | SUB GR. | Actuators, optical, ultrasound, shear layer mixing, surface jets |
| | | | |
| | | | |

19. ABSTRACT (Continue on reverse if necessary and identify by block number)

Turbulent chemically reacting flows present a formidable task for the development of schemes to control their evolution because they require 3-D field measurements and suitable actuators for the effective assessment and manipulation of the flow state, respectively. To this end, the present research focuses on the development of novel diagnostic methods for nonintrusive vorticity and concentrations measurements and new actuator technology for flow control via vorticity micro-manipulation. The diagnostic methods include the utilization of ultrasound scattering as a nonintrusive probe for direct field measurements of vorticity and energy spectra. This technique is tested in a low-speed swirling air jet because of its relevance to the formation and breakdown of streamwise vortices in free and wall-bounded shear flows. Highly-resolved concentration fields of conserved passive scalars are optically measured in a plane shear layer using a thermal analog. In contrast to measurements of dye concentration, the thermal measurements can be compared with mixing processes in gases where the Schmidt number is approximately 1, because the relevant thermal diffusion parameter, the Prandtl number, is approximately 7. The development of actuator technology has focused on flows near surface actuators such as the formation of small round turbulent jets normal to, and at the center of submerged resonantly driven piezoceramic actuators. These surface flows are of particular interest from the standpoint of actuator technology because they are produced without mass injection and can be manipulated on relatively short time scales.

| 20. DISTRIBUTION/AVAILABILITY OF ABSTRACT | 21. ABSTRACT SECURITY CLASSIFICATION |
|---|---|
| UNCLASSIFIED/UNLIMITED ☒ SAME AS RPT ☐ DTIC USERS ☐ | |

| 22a. NAME OF RESPONSIBLE INDIVIDUAL | 22b. TELEPHONE NUMBER (Include Area Code) | 22c. OFFICE SYMBOL |
|---|---|---|
| Dr. J.M. McMichael | (202) 767-4936 | AFOSR/NA |

DD FORM 1473, 83 APR EDITION OF 1 JAN 73 IS OBSOLETE.



SECURITY CLASSIFICATION OF THIS PAGE

**Research Progress and Forecast Report**

# NOVEL DIAGNOSTIC TECHNIQUES AND ACTUATOR TECHNOLOGY FOR TURBULENT SHEAR FLOWS

**AFOSR Grant F49620-92-J-0518**

**Submitted to**

Air Force Office of Scientific Research
Bolling Air Force Base, Building 410
Washington, D.C. 20332

**by**

A. Glezer
Woodruff School of Mechanical Engineering
Georgia Institute of Technology
Atlanta, GA 30332-0405

# Table of Contents

# NOVEL DIAGNOSTIC TECHNIQUES AND ACTUATOR TECHNOLOGY FOR TURBULENT SHEAR FLOWS

## I. Introduction

The present research program has two primary objectives. The first objective is to develop and demonstrate the utility of novel diagnostic methods for nonintrusive measurements of vorticity and concentrations of passive scalars in free shear flows. The second objective is to implement new actuator technology for flow control via micro-manipulation of vorticity. The successful accomplishment of these objectives will yield sensor and actuator technologies suitable for the implementation of real time feedback control of mixing in free shear flows.

The study of the mechanisms which lead to mixing in shear flows is crucial to technological applications in combustion processes. These processes involve chemical reaction between two or more species within free turbulent shear flows, and depend critically on mixing of the flow streams. Thus, the development of methods for enhancement and control of mixing through flow manipulation will have a direct impact on the performance of propulsion systems from the standpoint of efficient combustion and controllable thrust. Because these flows are extremely receptive to and rapidly amplify low-level disturbances that are introduced at the flow boundaries, mixing can be substantially modified with relatively low power input. For combustion processes such excitation may influence the overall reaction rate, as well as the spatial and temporal distribution of heat release and reaction products.

Turbulent chemically reacting flows present a formidable task for the development of schemes to control their evolution because they require 3-D field measurements and suitable actuators for the effective assessment and manipulation of the flow state, respectively. To this end, we have begun to develop in parallel under the present AFOSR Grant novel optical and ultrasound field diagnostics and actuator technologies for the measurement and control of mixing in a plane shear layer.

Recent theoretical and experimental investigations have shown that ultrasound scattering can be used as a non intrusive spectral probe of vorticity with potential applications to *direct nonintrusive measurements of vorticity and energy spectra.* Some aspects of this technique have been tested in a low-speed swirling air jet and are reported in section II of this report. This flow has been selected for this investigation because of its relevance to the formation and breakdown of streamwise vortices in free and wall-bounded shear flows.

The formation of small round turbulent jets that are produced normal to, and at the center of submerged resonantly driven piezoceramic actuators has been investigated experimentally and is reported in section III of this report. These surface flows are of particular interest from the standpoint of actuator technology because they produced without mass injection and are comprised entirely of radially entrained fluid and because they can be manipulated on relatively short time scales.

Optical technique for highly-resolved field measurements of concentration conserved passive scalars in a plane shear layer in water is also under development. The temperature distribution between two streams maintained at different constant temperatures is a thermal analog to the concentration measurements normally performed in conventional blow-down chemically reacting shear layer facilities. The study of mixing in water by exploiting temperature as a passive scalar is of particular interest because the relevant diffusion parameter, the Prandtl number, is approximately 7. Hence a reasonable comparison can be made with mixing and combustion processes in gases where the relevant diffusion parameter, the Schmidt number, is approximately 1 (the Schmidt number in water is approximately 1000). Some aspects of this work are described in section IV of the present report.

## II. Vorticity Measurements Using Ultrasound Scattering

### II.1. Overview

The propagation of sound waves through turbulent flow fields results in phase and amplitude distortions of the wave fronts and wave scattering (e.g., Monin and Yaglom 1980). In the atmosphere, for example, the distortion and scattering of sound waves is primarily effected by variations in the speed of sound due to turbulent temperature and velocity fluctuations and can be analyzed as for electromagnetic waves with proper modification of the medium refractive index. Lighthill (1953) and Kraichnan (1953) obtained a relation between the scattering cross-section $d\Sigma$ in any direction $\hat{r}$ of a volume $V$ that contains the turbulence (i.e., the energy flux scattered by the volume $V$ into a solid angle element $d\Omega$ around $\hat{r}$ normalized by the energy flux density of the incident wave) and the correlation function of the refractive index that depends on Correlations of temperature and velocity fluctuations.

Most investigations to date (Baerg and Schwarz 1965, Ho and Kovasznay 1976, Korman and Beyer 1988) have been primarily concerned with the determination of the scattering cross-section of a turbulent flow from measurements of the velocity field. As was noted by Monin and Yaglom, because *the scattered waves contain information regarding the scattering turbulent medium, they may be useful for remote probing of the characteristics of that medium.* In particular, the inverse problem which is to obtain the velocity field of an unknown flow from measurements of scattered sound has been noted in the literature (e.g., Engler 1989, Englar and Schmidt 1989). More recently, a new analysis of the scattering of acoustic waves by vorticity concentrations that is based on the framework of classical field theory has been developed by Lund and his co-workers (1989). This analysis makes use of the analogy between the interactions of electromagnetic radiation with charged particles and of sound with vorticity concentrations. The latter applies when the sound frequency is high compared to the inverse of the characteristic time scale associated with the evolution of the vorticity concentrations.

The work of Lund and his co-workers has shown that when a plane acoustic wave of angular frequency $\nu_0$ propagates through a rotational flow field (laminar or turbulent) there is a linear relationship between the Fourier component at a frequency $\nu$ of the scattered acoustic pressure in a given direction $\hat{r}$ and the Fourier transform, in space and time, of the vorticity component that is normal to the plane defined by the wave vectors of the incident and scattered acoustic waves at frequency $\nu - \nu_0$. The three wavenumber components of the Fourier transform of the vorticity vector are determined by the frequencies and wavevectors of the incident and scattered acoustic waves so that by varying the frequency of the incident wave and $\hat{r}$, all three components of the wave vector of the

measured Fourier component can be resolved. This means that in principle the amplitude of the Fourier transforms, in space and time, of all three components of the vorticity field can be measured non-intrusively thus suggesting a powerful means for studying vorticity scales and energy cascades between them in various shear flows. Such data are extremely difficult to measure using conventional measurement techniques.

The present experiments are concerned with the scattering of ultrasound from a stationary vortex having a fixed diameter and a nominally uniform axial vorticity distribution, the magnitude of which can be varied continuously over a broad range. This vortex forms downstream of the nozzle of a swirling jet and its circulation (and hence the swirl number of the jet) are carefully controlled by the angular velocity of a four-blade paddle that is placed in the jet plenum. The axial (streamwise) and tangential velocity distributions of the jet are measured using X-wire anemometery.

## II.2. Theoretical Background

Lighthill and Kraichnan analyzed the scattering of a plane acoustic wave, having an incident wave vector $\bar{k}_0$ and angular frequency $\nu_0$, by a turbulent medium. In particular they considered an adiabatic flow with density $\rho_0 + \rho(\bar{x},t)$ (where $\rho(\bar{x},t) << \rho_0$), where $\nu_0$ is much larger than any frequency associated with the turbulence and viscous effects are negligible. They showed that the acoustic energy per unit time that is scattered into a solid angle element in a direction $\hat{r}$ at an angular frequency $\nu$ is

$$P(\hat{r},\nu) = \frac{2\pi I \nu^4 \cos^2\theta}{c^6} \hat{r}_i \hat{r}_j F_{ij}(\bar{q}, \nu - \nu_0) \tag{1}$$

where $I$ is the acoustic energy flux of the incident wave, $c$ is the speed of sound, $\theta$ the scattering angle (between unit vectors in the incident and scattered directions), $\bar{q} = (\nu\hat{r}/c) - \bar{k}_0$ is the difference between scattered and incident wave vectors with magnitude $q = (2\nu_0/c)\sin(\theta/2)$, and $F_{ij} = \tilde{u}_i \tilde{u}_j^*$ where $\tilde{u}_i$ is the complex Fourier transform (in time and space) of the velocity component and the star denotes its complex conjugate. If the turbulence is statistically stationary, homogeneous and isotropic, the average acoustic differential cross section is

$$\langle \sigma(\hat{r}) \rangle = \frac{\pi I \nu_0^4 \sin^2 2\theta}{16 c^6 \sin^2(\theta/2)} \left\langle E\left(\frac{2\nu_0}{c}\sin\frac{\theta}{2}\right)\right\rangle \tag{2}$$

where $E(k)$ is the energy spectrum.

That sound is scattered by vorticity is demonstrated by considering the effect of a plane sound wave on a point vortex whose axis is normal to the wave vector. The passage of the wave induces time-harmonic motion of fluid particles and, in particular, of fluid particles that are on vortex lines. The unsteady vorticity distribution results in far-field pressure fluctuations (Mohring, 1978) that can be interpreted as scattering of the incident sound wave. This fundamental mechanism can be extended to three dimensions and to vorticity distributions in finite domains.

In three dimensions, consider a vortex filament of circulation $\Gamma$ along $X(\sigma,t)$, where $\sigma$ is a Lagrangean parameter labeling points along the filament. As shown by Lund 1989), the far-field acoustic pressure radiated by such a vortex filament is, to leading order,

$$p(\bar{r},t)=\frac{\Gamma\varepsilon_{ijk}\hat{r}_i}{4\pi c|\bar{r}|}\frac{\partial}{\partial t}\oint d\sigma\,\dot{X}_j X_k' \tag{3}$$

where

$$\dot{X}_j \equiv \frac{\partial X_j}{\partial t}$$

is the velocity of the filament,

$$X_j' \equiv \frac{\partial X_j}{\partial \sigma}$$

is the tangent to the filament and the right hand side of (3) is evaluated at time $t_{ret}=t-|\bar{r}|/c$. If the vortex is in the domain of propagation of an incident plane sound wave having velocity amplitude $v_j^0$, a wave vector $\bar{k}_0$, and angular frequency $\nu_0$ that is high in comparison with the inverse of any time scale associated with the self-induced motion of the vortex, then each point of the vortex oscillates with the local particle velocity induced by the wave

$$\dot{X}_j = v_j^0 e^{i(\bar{k}_0\cdot\bar{X}-\nu_0 t)}.$$

As shown in Eqn. (3), this oscillatory motion generates far field sound pressure, thus providing the basic mechanism for the scattering of sound by vorticity.

A continuous distribution of vorticity $\overline{\omega}(\bar{y},t)$ within a finite domain may be treated as a concentration of tightly packed filaments, and equation (3) can be modified by the substitutions

$$\Gamma \oint d\sigma X_j' \rightarrow \int d^3 y \omega_j(\bar{y},t)$$

$$\overline{X} \rightarrow \bar{y}. \tag{4}$$

With these substitutions, and

$$f(t_{ret}) = \int dt f(t) \delta(t - t_{ret}) = \frac{1}{2\pi} \int dt f(t) \int dv e^{-iv(t-t_{ret})},$$

Lund showed that the far field acoustic pressure scattered by the vorticity $\omega$ is

$$p_{scatt}(\bar{x}, v) = \frac{p_0 v i \pi^2}{c^2 |\bar{x}|} e^{ik_0|\bar{x}|} \left(\hat{k}_0 \times \hat{x}\right) \cdot \tilde{\omega}(\bar{q}, \Delta v) \tag{5}$$

where $p_0$ is the amplitude of pressure of the incident wave field, $\Delta v = v - v_0$ is the angular frequency difference between the scattered and the incident waves, and $\tilde{\omega}$ is the Fourier transform in space and time of the vorticity. Equation (5) establishes a relationship between $p_{scatt}$ and the component of $\tilde{\omega}$ that is normal to the scattering plane (defined by $\hat{k}_0$ and $\hat{r}$). Equation (5) is valid if the particle velocity induced by the sound wave is small in comparison with the characteristic velocity of the vortical flow, which in turn is supposed to be of low Mach number, and the sound frequency is high in comparison with the inverse of the characteristic time scales of the flow. The experiments reported in the present paper verify the relationship between $p_{scatt}$ and $\tilde{\omega}$ for a uniform distribution of axial vorticity $\omega_0$ within the core of a swirling jet.

The work of Lund and Rojas (1989), in which the effect of an infinite plane wave incident on a bounded body of vorticity was considered, introduced an additional angular factor

$$h(\theta) = 1 + \frac{1}{\cos\theta - 1}.$$

This leads to an unphysical divergence at small angles, and the reasoning must be modified to take into account the finite extent of the incident wave. This we do in Appendix A, where it is shown that the result is equivalent to setting $h(\theta) = 1$.

### II.3. The Swirling Jet

The swirling jet facility and the coordinate system are shown schematically in Figure II.1. The jet issues from an axisymmetric round nozzle having an exit diameter $D = 2.54$ cm and a contraction ratio of 36:1. The swirling generator is a four-blade paddle that is placed in a 15.24 cm cylindrical tube upstream of the nozzle and is rotating about the streamwise (x) axis. The distance between the downstream edge of the blades and the jet nozzle is adjustable but is set at 60 cm in the present experiments. The paddle shaft extends through the rear wall of the jet plenum and is connected to a DC motor equipped with a speed controller. The jet is driven by four radial blowers placed symmetrically around the perimeter of the plenum. Low turbulence level in the plenum is achieved by air filters, honeycomb material, and screens.

The degree of swirl is usually characterized by the dimensionless swirl number $S_W$ which, for a given jet diameter, measures the ratio of streamwise flux of tangential and axial momentum. That is

$$Sw = \frac{2\int_0^\infty UVr^2 dr}{D\int_0^\infty \left(U^2 - V^2/2\right) r dr},$$

where $U$ and $V$ are the mean axial and azimuthal velocity components. For an axisymmetric flow, the effectiveness of the swirl generator can be measured by the linearity of the radial distribution of $V$ downstream of the jet exit plane which implies a solid body rotation with uniform distribution of axial vorticity.

Previous investigations of swirling jets have employed a variety of swirling generators with varying degrees of effectiveness. A rotating pipe swirl generator was employed by Rose (1962) in an air jet ($\mathrm{Re} = 1.5 \times 10^4$). In the absence of a converging nozzle, however, the ensuing jets had relatively low swirl numbers (the maximum swirl number is estimated to be 0.21) and nonuniform streamwise vorticity distributions near the exit plane. Tangential blowing upstream of the jet nozzle is far more effective and more commonly used for the generation of swirl. Chigier and Chervinsky(1967), for example, used four tangential slots in an air jet ($\mathrm{Re} = 3 \times 10^5$) and obtained swirl numbers as high as 0.64 and virtually uniform solid body rotation within the core of the jet. It is noted,

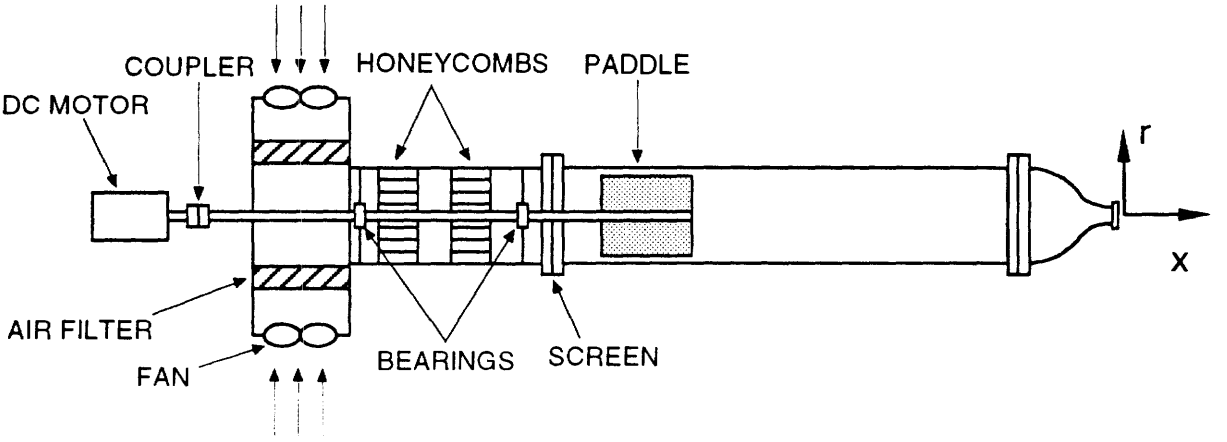
COUPLER
HONEYCOMBS
PADDLE
DC MOTOR
r
X
AIR FILTER
FAN
BEARINGS
SCREEN

Figure II.1

however, that these measurements were taken at $x/D = 4.1$, and that for $Sw > 0.4$, profiles of the streamwise velocity develop a pronounced local minimum near the jet centerline which is the precursor for the development of reversed flow along the jet centerline and the formation of a recirculation region. Tangential blowing does not allow for independent variations of the swirl number and the (mean) axial velocity and, furthermore, it does not easily lend itself to both clockwise (CW) and counterclockwise (CCW) swirl. These shortcomings have led other investigators to replace tangential blowing with fixed or adjustable vanes (Sislian and Cusworth 1984).

The present swirl generator was designed to overcome some of the disadvantages of previous designs (Rose 1962, Chigier and Chervinski 1967, and Sislian and Cusworth 1984). It allows for continuous and repeatable variation of jet swirl number and for easy clockwise or counterclockwise reversal of the swirl. In the present experiments the swirl number was kept below $Sw = 0.4$ in order to avoid the appearance of a minimum of the axial velocity near the jet centerline. Because the rotation of the paddle increases the pressure drop through the cylindrical plenum the power input to the jet blowers was increased with swirl number so that the jet volume flow rate (measured at $x/D = 0.25$) was equal to the volume flow rate in the absence of swirl at Re = $10^4$. The volume flow rate was computed from radial profiles of the streamwise velocity component.

Profiles of the mean streamwise and tangential velocity components ($U(r,x,t)$ and $V(r,x,t)$, respectively) were measured at a number of streamwise stations using an X-wire anemometer probe. The anemometer output was digitized at 1024 Hz using a Masscomp laboratory computer with 12-bit A/D converters. The measured tangential velocity at each point is affected by radial gradients of the streamwise velocity. A first-order correction term to the mean tangential velocity $V$, $(\partial U/\partial r)(\Delta l/2)$ was applied where $U$ is the mean streamwise velocity and $\Delta l$ is the distance between the wires.

Radial distributions of the streamwise and azimuthal velocity components at $x/D = 0.25$, 1, 2 and 3 are shown in each of Figures II.2(a, b) ($Sw = 0$) and II.3(a, b) ($Sw = 0.24$). These velocity components are normalized by the jet exit speed $U_0 = 6.1$ m/sec in the absence of swirl. Figure II.2a shows that in the absence of swirl the streamwise velocity distribution near the jet exit plane resembles a hat-shaped profile with a relatively thin azimuthal shear layer. The potential core of the jet is prevalent through $x/D = 3$ despite the radial increase in the width of the azimuthal shear layer. The Mach number of the flow is $M \sim 10^{-2}$ - $10^{-3}$, low enough for Eqn. (5) to apply.

As a result of the swirl, there is a noticeable increase in the magnitude of the streamwise velocity near the jet centerline, and in the radial spreading of the jet shear layer (Figures II.3a and b). Similar changes in profiles of the streamwise velocity in swirling

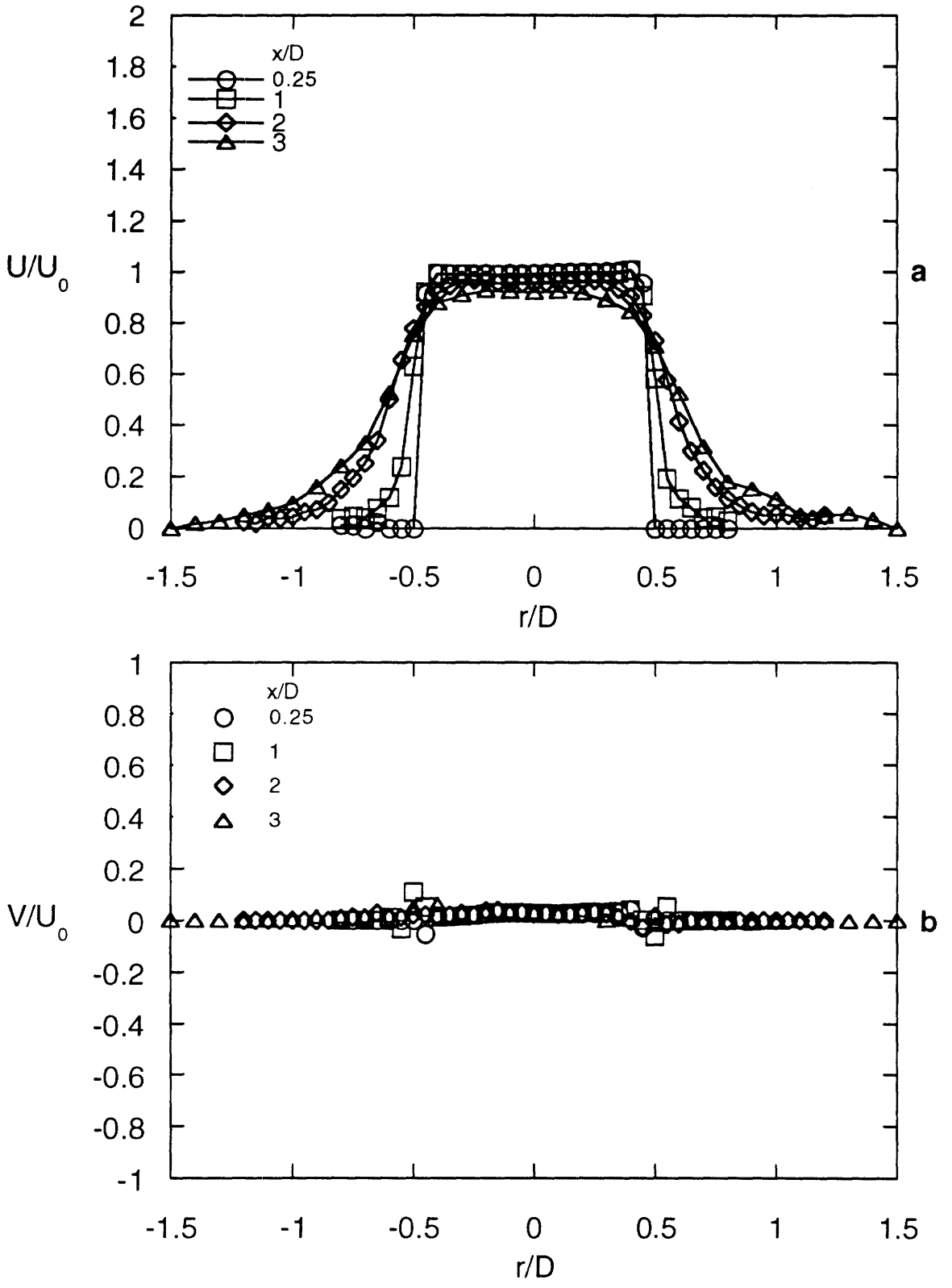


Figure II.2

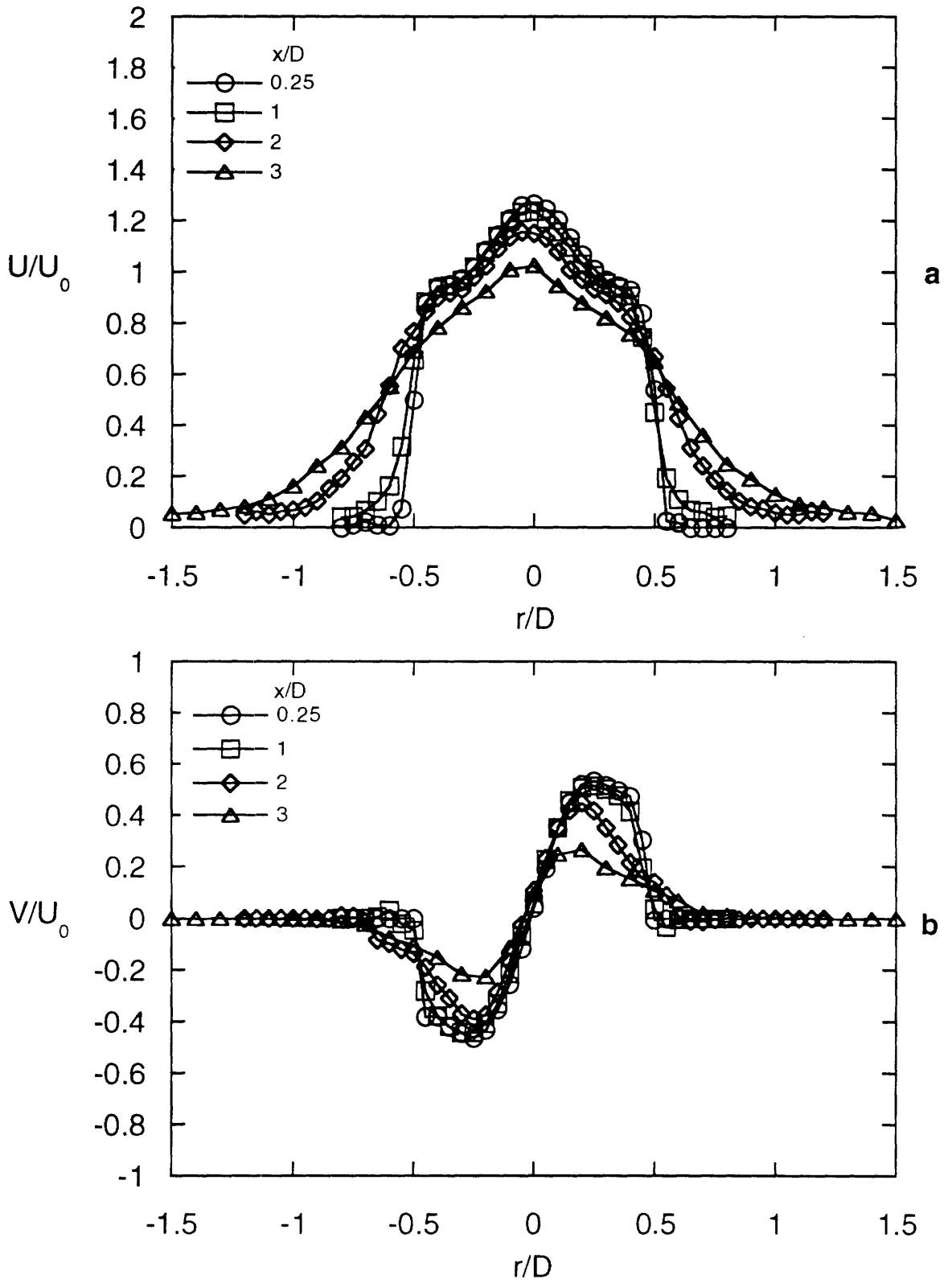


Figure II.3

jets were also reported by Rose (1962). It is noted that at $x/D = 3$, the centerline velocity is still somewhat higher than in the absence of swirl, and that the jet shear layer appears to have merged on the centerline. Figure II.3b further demonstrates that within the core of the jet, the tangential velocity varies almost linearly with $r$ thus indicating a solid body rotation with an approximately-uniform axial vorticity distribution $\omega_0$ (calculated at $r = 0$). Outside the core of the jet the tangential velocity decays exponentially in the radial direction. Figure II.4 shows that at $x/D = 0.25$ $\omega_0$ varies linearly with swirl number (negative values of $Sw$ correspond to CW rotation of the paddle).

The streamwise decay of the time-averaged centerline velocity $U_{cl}$ is shown in Figure II.5 for various swirl numbers. Because the volume flow rate of the jet is adjusted so that it is invariant with $Sw$, the centerline velocity for each curve is normalized by its magnitude at $x/D = 0.25$. Figure II.5 shows that the streamwise rate of decay of $U_{cl}$ increases substantially with swirl number and is clearly connected with the increase in the radial spreading and centerline merging of the jet shear layer (Figure 3a). The dashed line in Figure II.5 corresponds to $U_{cl}/U_{cl0} = a(x/D)^{-1}$ where $a$ is a constant (far enough downstream from the exit plane of a round turbulent jet, the centerline velocity decays like $1/x$). It is noteworthy to mention that as $Sw$ increases, $U_{cl}$ begins to decay like $1/x$ closer to the jet exit plane. At least within the range of swirl numbers considered here, similar decay rates were also measured by Rose (1962).

## II.4. Ultrasound Scattering

A nominally plane ultrasonic wavetrain is generated and propagates normal to the jet axis by a Sell-type transmitter (Anke 1974) that utilizes an electrostatically-driven thin metal-cladded polymeric membrane. The present transmitter has a square aperture measuring 16 cm on the side and its frequency bandwidth (within ±5 dB) is 5 to 100 kHz. It is similar to the transmitter used by Baudet, Ciliberto and Pinton (1991). In the present experiments the frequency of the incident wave is $f_0 = \nu_0/2\pi = 42$ kHz. The scattered ultrasound is measured by a 12 mm-diameter microphone with 6.5 mm-diameter sensing area (shown schematically in Figure II.6) that is traversed azimuthally (a distance $r$ from the centerline) at a number of streamwise stations such that its centerline intersects the jet centerlines at a right angle (the microphone output is digitized at 500 kHz). The azimuthal scattering angle between the wave vector of the incident (planar) wave field and the centerline of the microphone is $\theta$. As discussed in section 2, the measured scattered pressure field corresponds to the Fourier transform of the axial vorticity component which is normal to the plane of the incident wave vector and the centerline of the microphone. The normalized directional response of the microphone $\Phi(\varphi)$ (where $\varphi$ is the angle

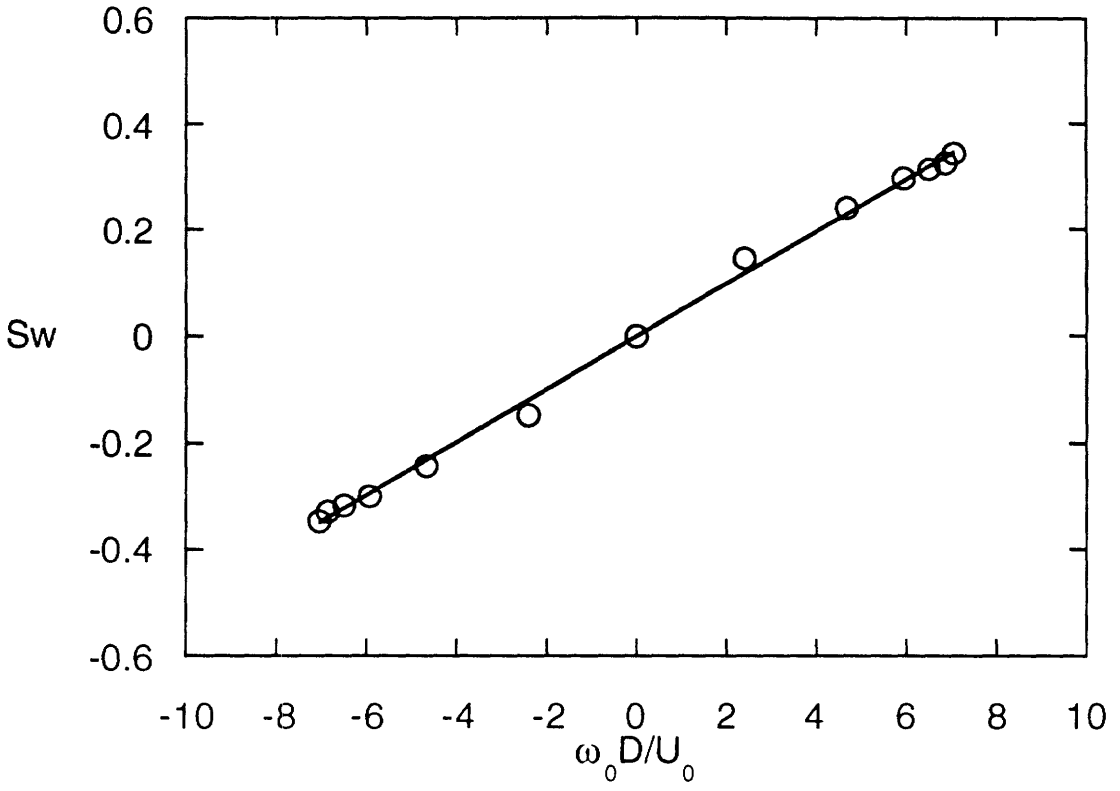


Figure II.4

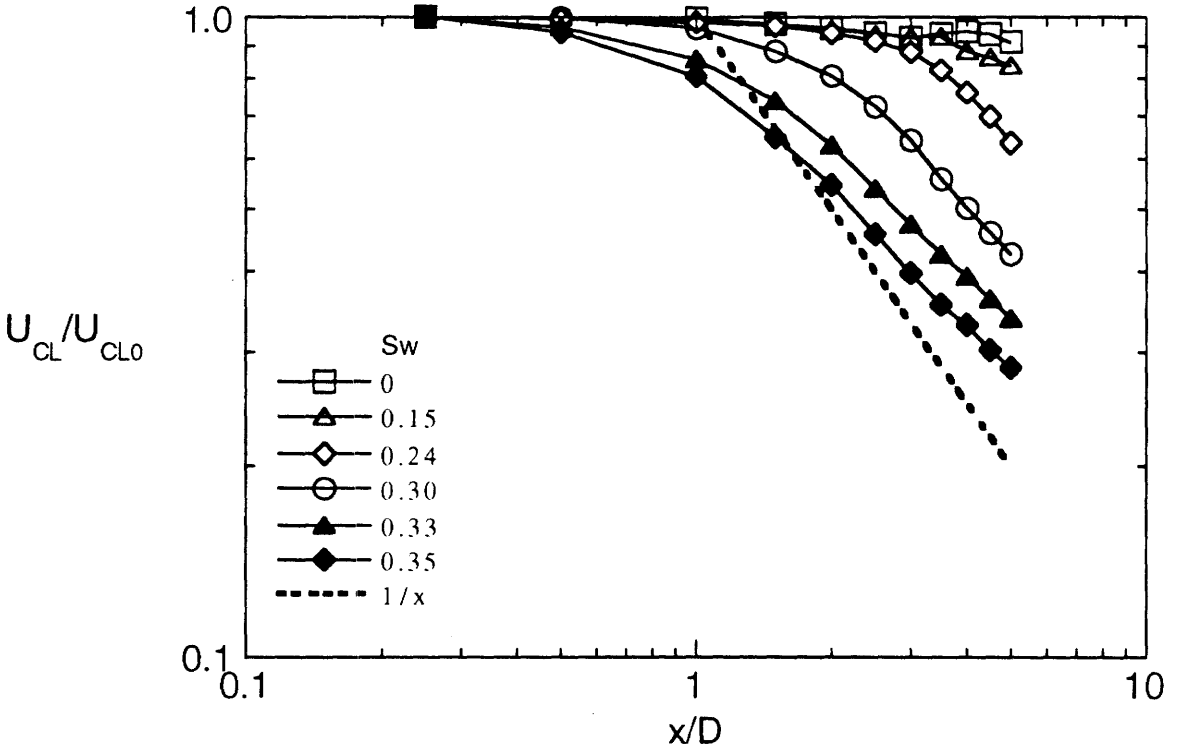


Figure II.5

between the microphone's centerline and the wave vector of an incident plane wave) is shown in Figure II.7. The microphone response is measured at the working frequency of 42 kHz and with 5° angular increment. Note that $\Phi(\varphi)$ is nearly axisymmetric, has a maximum at $\varphi = 0$, and drops to -15.5 dB at $\varphi = \pm 45°$.

A power spectrum $E_p(f)$ of the pressure field in the absence of swirl measured at $x/D = 0.25$, $r/D = 1$, and $\theta = -30°$ is shown in Figure II.8a. Because the microphone is placed in the transmitted wave field, it measures the acoustic pressure of the incident wave even when $Sw = 0$ and thus $E_p(f)$ exhibits a single spectral peak $E_p(f_0)$ at the transmitter frequency. The effect of swirl on the spectral peak at $f_0$ is demonstrated in Figures II.8b and II.8c. When the swirl is CCW ($Sw > 0$, Figure II.8b), the normalized amplitude of the spectral peak at the transmitter's frequency $\eta(f_0) = \|p\|_{MAX}/\|p\|_0 - 1 = 0.41$ (where $\|p\|_0 = E_p(f_0)^{1/2}\big|_{Sw=0}$ and $\|p\|_{MAX} = E_p(f_0)^{1/2}\big|_{Sw\neq 0}$) and when the swirl is CW (Figure II.8c), $\eta(f_0)$ = -0.45. The corresponding increase and decrease in the amplitude of the spectral peak at $f_0$ are nominally the same (±2.5%) for CW and CCW swirl. That the power spectra of the microphone signals in the absence of swirl (Figure II.8a) and when the jet is stopped (not shown) are virtually indistinguishable, suggests that in the absence of swirl the streamwise vorticity is too weak to induce measurable sound scattering. It should be noted that unlike the Karman vortices in the wake experiments of Baudet *et al.*, the streamwise vortex associated with the swirling jet has no net celerity normal to the jet axis even though streamwise vorticity is clearly advected axially and radially. Hence, there is no frequency shift between the transmitted and scattered frequencies and $\Delta\nu = \nu_0 - \nu = 0$ in Eqn. (5).

The sensitivity of $E_p(f_0)$ to the sense of the swirl (Figures II.8b and c) results from a superposition of the acoustic pressures of the incident and scattered waves by the microphone. Denote $p_i = P_i(f_0)\cdot e^{i\Psi_i}$ and $p_s = P_s(f_0)\cdot e^{i\Psi_s}$ as the respective acoustic pressures of the incident and scattered waves where $P_s << P_i$, and $P_T$ the amplitude of the pressure measured by the microphone. Then

$$P_T^2 = |p_i + p_s|^2 \approx P_i^2 + 2P_iP_s\cos(\Delta\Psi)$$

where $\Delta\Psi = \Psi_i - \Psi_S$ is the phase difference between the incident and scattered acoustic pressures. Because the frequencies of the incident and scattered waves are identical, $\Delta\Psi$ is almost invariant. Using Eqn. (5) let $P_s = \alpha\omega_0$, where $\alpha$ depends on the geometry of the transmitter-receiver configuration and the Fourier transform of the vorticity distribution normalized with $\omega_0$. As shown below, when the vorticity distribution is uniform (i.e.,

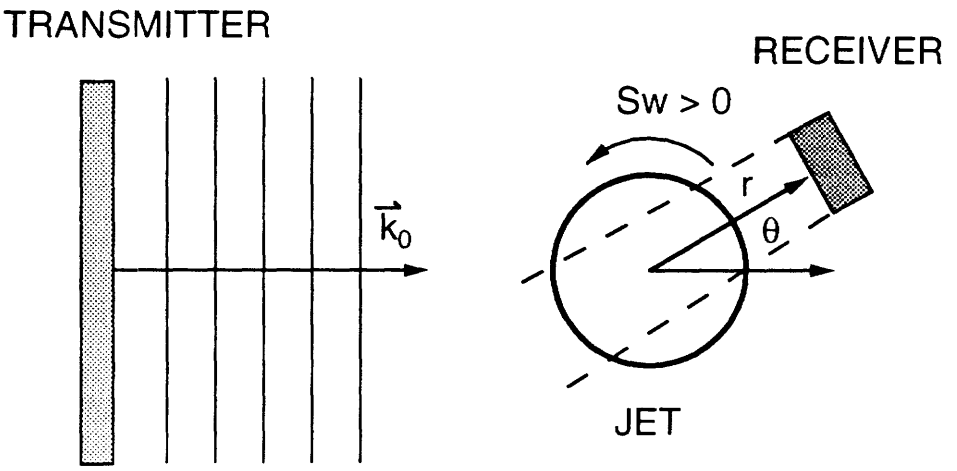


Figure II.6

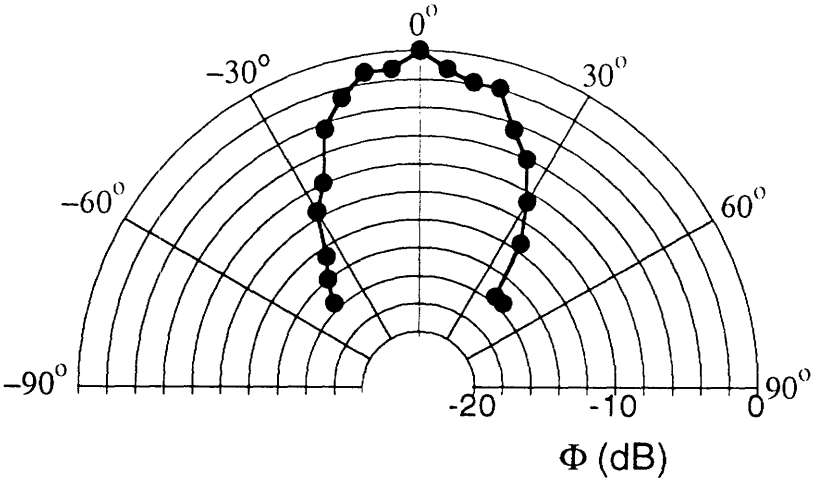


Figure II.7

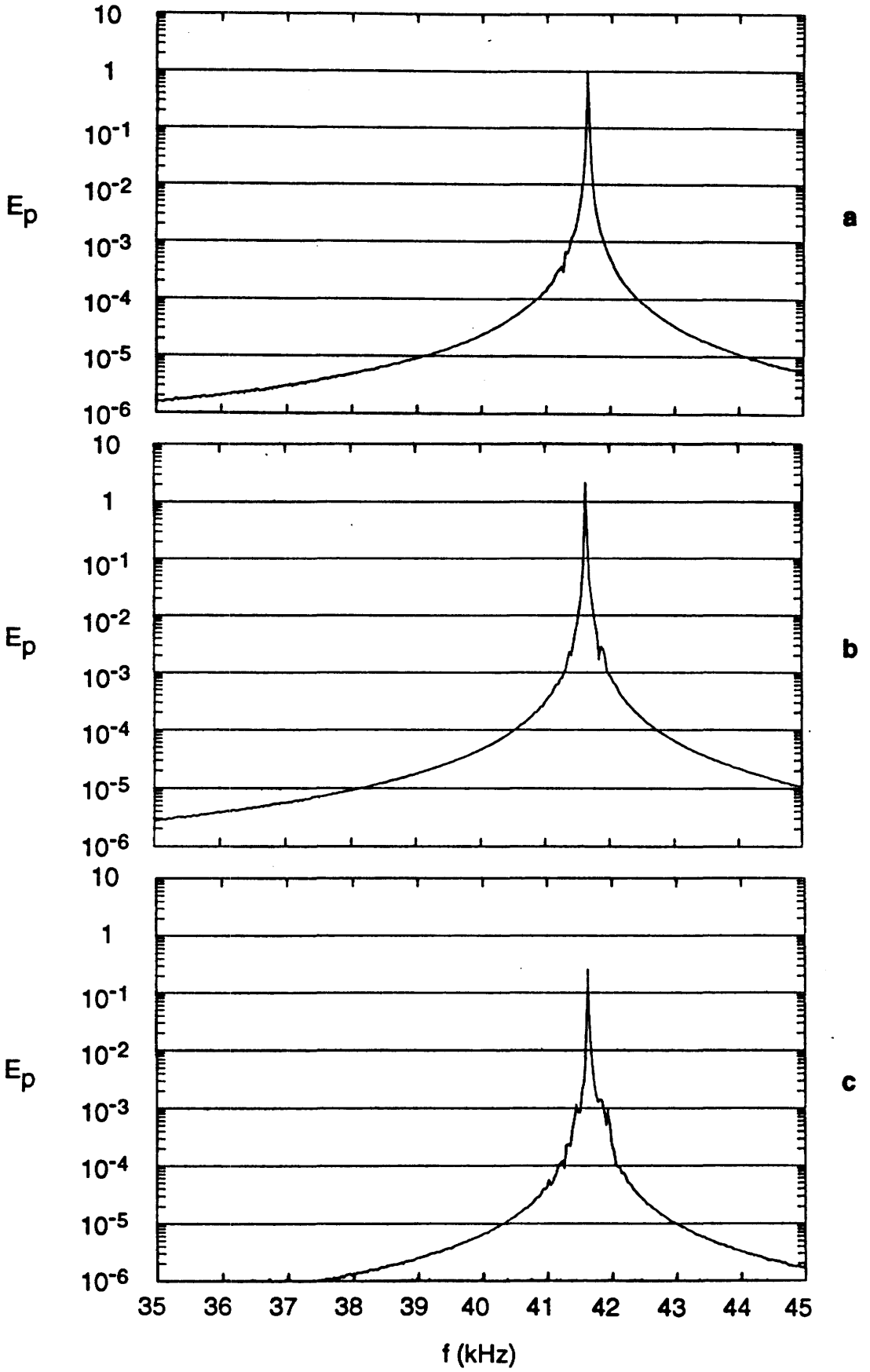
10
1
10-1
10-2
10-3
10-4
10-5
10-6
Ep
a
b
c
35
36
37
38
39
40
41
42
43
44
45
f (kHz)

Figure II.8

solid body rotation), $\alpha$ is a constant and its sign depends on the scattering angle. Hence, if the mean $\Delta\Psi$ is almost invariant (i.e., when the frequencies of the transmitted and scattered waves are identical, the effects of turbulent fluctuations are averaged, and the geometry is fixed)

$$\tilde{p} = \frac{P_T}{P_i} - 1 \approx \frac{\alpha \cos(\Delta\Psi)}{P_i} \cdot \omega_0$$

and $E_p(f_0)$ is sensitive to the sense of the swirl.

Figures II.9 and II.10 ($x/D$ = 0.25) show that for a given scattering angle ($\theta$ = $\pm 15^0$ and $\pm 30^0$), the normalized spectral peak of the scattered waves $\eta(f_0)$ varies linearly with $\omega_0$ and that $d\eta(f_0)/d\omega_0$ is independent of the amplitude (or intensity) of the incident wave field. This is also consistent with the theory presented in section 2. Consider a time-invariant, axisymmetric distribution of axial vorticity within a cylinder of radius $r_0$ the Fourier transform of which is

$$\tilde{\omega}(q) = \frac{1}{(2\pi)^2} \int_0^\infty \omega(r) r dr \int_0^{2\pi} e^{-i\bar{q}\cdot\bar{r}} = \frac{1}{2\pi} \int_0^\infty \omega(r) r dr J_0(qr).$$

If the axial vorticity near the exit plane of the swirling is approximated by

$$\omega(r) = \begin{cases} \omega_0 & 0 < r < r_0 \\ 0 & r > r_0 \end{cases}$$

then its Fourier transform is given by:

$$\tilde{\omega}(q) = \frac{\omega_0}{2\pi} \int_0^{r_o} r dr J_0(qr) = \left(\frac{\omega_0 r_0^2}{2\pi}\right)\left(\frac{J_1(qr_0)}{qr_0}\right)$$

where $J_n$ is the Bessel function of the first kind of order $n$. We note that since the celerity of $\omega$ is zero, only the zero frequency component is nonvanishing. Given the normalized directional response of the microphone $\Phi(\varphi)$ (Figure II.7) and that in the present experimental set-up $\varphi = \theta$,

$$\tilde{p} = C\omega_0 r_0^2 g(\theta) \tag{6}$$

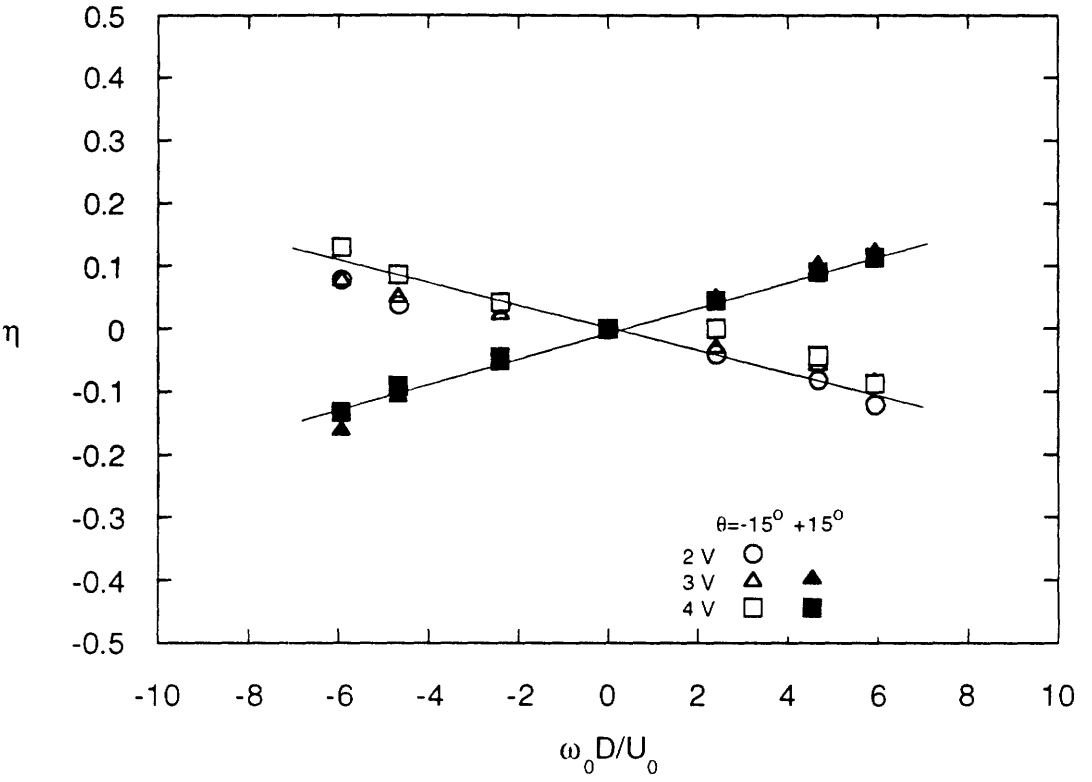


Figure II.9

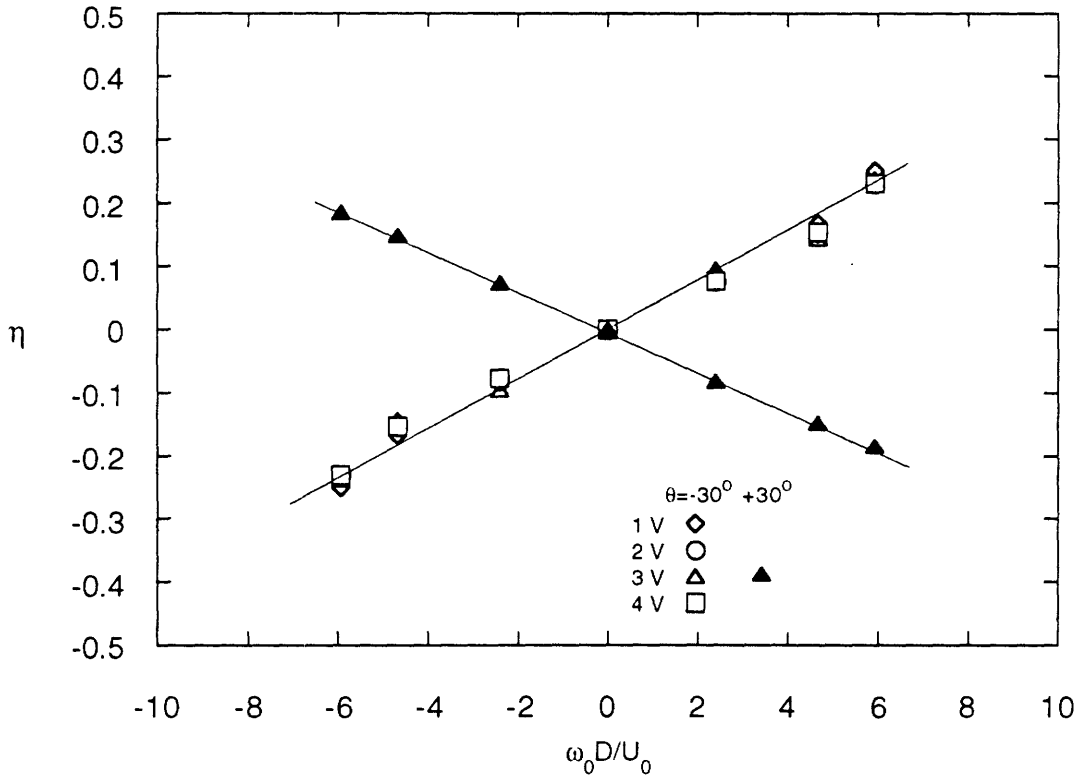


Figure II.10

where

$$C = \frac{\nu\pi\cos(\Delta\Psi)}{2|\bar{r}|c^2}$$

is a constant for a given transmitter frequency and fixed positions of the transmitter and the receiver, and

$$g(\theta) = \frac{1}{\Phi(\theta)}\sum_{\eta}\Phi(\eta)\Omega(\theta-\eta) \tag{7}$$

where

$$\Omega(\theta) = \sin(\theta)\left[\frac{J_1(qr_0)}{qr_0}\right]$$

with

$$q = \frac{4\pi f}{c}\sin(\theta/2).$$

Equation (6) shows that $\tilde{p}$ varies linearly with $\omega_0$ and that it is independent of the level of acoustic input. The latter is true independently of the vorticity distribution. The angular response of the receiver $\Phi(\theta)$ in Eqn. (7) is especially important for large $\theta$ where $\Phi(\theta)$ is usually small because it corrects for errors due to angular attenuation of the microphone. Equation (7) includes a convolution with the receiver response. This is needed because, as the microphone does not have a flat angular response, it receives scattered acoustic radiation not only from direction $\theta$ but also from other directions as indicated in Figure 7. A similar convolution with the transmitter is not necessary because our vortex lies well within the region where the angular dependence of the transmitter is flat.

Although $\eta(f_0)$ is linear with $\omega_0$, for a given scattering angle, the differential change of the normalized scattered pressure with respect to the (non-dimensional) axial vorticity $d\eta / d(\omega_0 D/U_0)$ varies substantially with $\theta$. In fact, Figures II.9 and II.10 demonstrate that $d\eta / d(\omega_0 D/U_0)$ has the same sign as $\theta$ for $\theta = \pm 15^0$ and opposite sign for $\theta = \pm 30^0$. That $d\eta / d(\omega_0 D/U_0) > 0$ ($\theta = \pm 15^0$) implies that the pressure of the

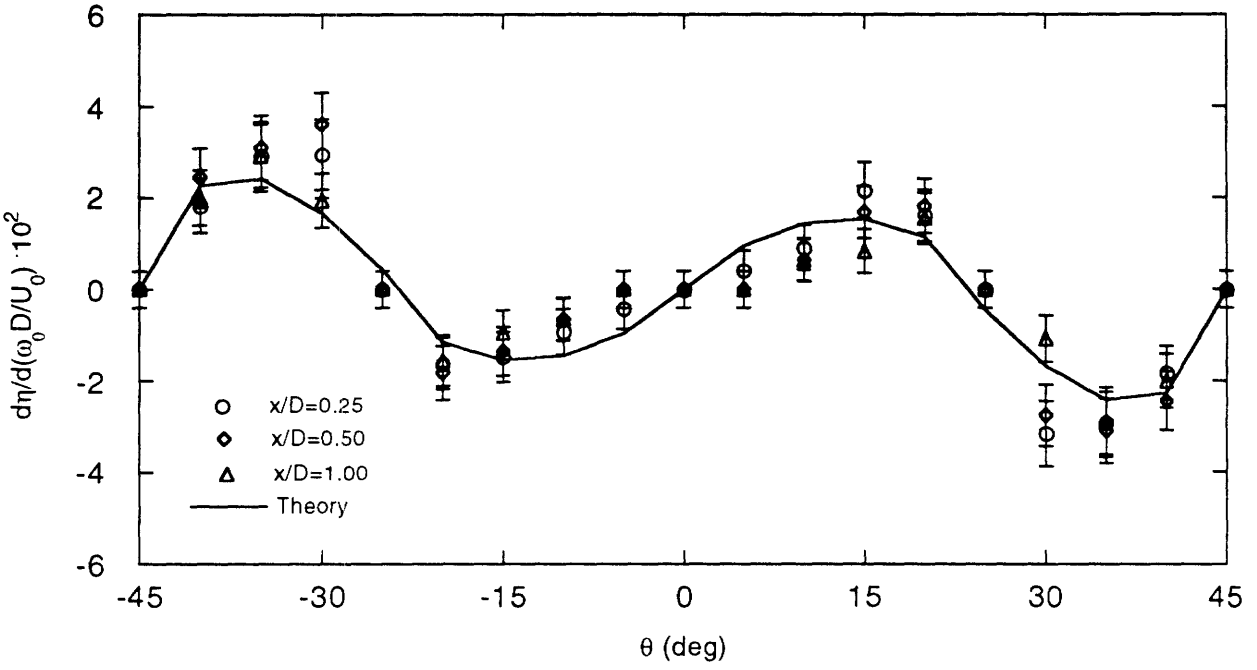
6
4
2
0
-2
-4
-6
-45
-30
-15
0
15
30
45
θ (deg)
dη/d(ω0D/U0)·10²
x/D=0.25
x/D=0.50
x/D=1.00
Theory

Figure II.11

scattered ultrasound increases when the direction of swirl is towards the receiver (cf, Figure II.6) and decreases when the jet rotates away from the receiver. However, the opposite is true for $\theta = \pm 30^0$. The variation of $d\eta / d(\omega_0 D/U_0)$ with the scattering angle for $x/D$ = 0.25, 0.5 and 1 is shown in Figure II.11 (symbols). The similarity between the three data sets indicates that the radial distribution of the axial vorticity within the jet does not vary substantially between theses streamwise stations as is evidenced by the similarity of corresponding radial profiles of the azimuthal velocity component (Figure II.3b). Figure II.11 shows that $d\eta / d(\omega_0 D/U_0)$ is antisymmetric with respect to $\theta$ and that it is positive for $0 < \theta < 25^0$ and negative for $25^0 < \theta < 45^0$. Furthermore, the pressure of the scattered sound does not vary with $\omega_0$ for $|\theta| \approx 25^\circ$ and $45^0$ (and of course for $\theta = 0$). The local extremae near $|\theta| \approx 15^0$ and $35^0$, indicate that at these angles the scattered wave is most sensitive to changes in the magnitude of the streamwise vorticity.

These features of $d\eta / d(\omega_0 D/U_0)$ can also be obtained from Eqns. (6) and (7). To begin with, the function g($\theta$) given by Eqn. (7) is odd in $\theta$ and thus antisymmetric. For $r_0$ = 1.2 cm and $f_0$ = 42 kHz the first two zeros of $J_1$ are at $qr_0$ = 3.83 and 7.02, and hence $d\eta / d(\omega_0 D/U_0)$ vanishes at $\theta = 23^0$ and $45^0$. The maximae of $d\eta / d(\omega_0 D/U_0)$ are determined from differentiation of Eqn (6) with respect to $\theta$ and are found to be at $\theta$ = $15^0$ and $32^0$ again, in good agreement with the experimental results. Figure II.11 shows the quality of the fit of g($\theta$) (solid line) when it is properly scaled to the experimental data.

A swirling jet will generate a temperature gradient that will also scatter some sound. This effect was studied in Contreras and Lund (1990) where it was established that the ratio of sound scattered at frequency $\nu$ due to temperature variations $\Delta T$ to that due to vorticity $\omega$ is of order

$$\frac{\nu \Delta T}{\omega T}$$

Our temperature fluctuations were kept below 0.1 °C so that this factor is of order $10^{-2}$ and temperature effects can safely be ignored.

Our results cannot be explained by a geometrical acoustics argument [REF. to Landau and Lifshitz (1975) and Lindsay (1948)] since we are not near the ray theory limit in which wavelengths are much smaller than the relevant space scale for vorticity variations and, in our configuration, it would give a ray deviation of about one degree without angular dependence nor amplitude change.

## II.5. Summary and Outline of Future Research

The present experiments are concerned with the measurements of a vorticity field using ultrasound scattering. More specifically, with the scattering of a plane ultrasonic wave field by an approximately uniform axial vorticity concentration within the core of a swirling jet. The dependence of the scattered pressure on the magnitude of the Fourier transform of the axial vorticity as well as on the sense of swirl and the scattering angle are measured near the exit plane of the jet. It is shown that the normalized scattered pressure varies linearly with the axial vorticity and that the sensitivity of the scattered pressure with respect to the axial vorticity depends on the scattering angle. These findings are in good agreement with theoretical predictions using a simple vortex model.

While direct measurements of the scattered pressure can be related to the Fourier transform of the vorticity component that is normal to the incident wave vector and the scattering direction, it is also desirable to obtain the vorticity distribution in physical space rather than in Fourier space. In principle, if the Fourier transform of a time-invariant vorticity distribution in Fourier domain $\tilde{\omega}(\bar{q})$ can be measured with enough resolution, its distribution in the physical domain $\omega(\bar{x})$ can be obtained from the inverse transform. To measure $\tilde{\omega}(\bar{q})$, $\bar{q} = |q| \cdot \hat{q}$ should be varied both in magnitude and direction. The magnitude of $\bar{q}$ can be varied by sweeping the transmitter's frequency while variation in the scattering angle results in changes in both $|q|$ and $\hat{q}$. Since the sensitivity of the scattered pressure with respect to the vorticity $d\eta / d(\omega_0 D/U_0)$ depends on the scattering angle, it is probably more practical to vary $f_0$ while keeping $\theta$ at the value for which $d\eta / d(\omega_0 D/U_0)$ is maximum. It should be noted that because the Fourier transform of an axisymmetric vorticity distribution has no imaginary part, both $\omega(r)$ and $\tilde{\omega}(q)$ are real functions, and the distribution of $\tilde{\omega}(q)$ can be measured, up to one scale factor (which is obtained from the calibration of the receiver), with the present experimental set-up.

During the second year of this project we will design and construct a novel radial and axial traversing mechanism for the transmitter and receiver that will allow for continuous variations of the scattering angle. By varying the frequuency and the scattering angle it will be possible to vaty the two components of the wave vector in planes that are normal to the jet's axis of symmetry. We anticipate that theses measurements will yield spectral vorticity data suitable for an inverse Fourier transform that will yield nonintrusive measurements of mean axial vorticity distributions in planes that are normal to the jet centerline.

# III. Surface Jets Produced by Piezoelectric Actuators

## III.1. Overview

Fluid motion produced by oscillating boundaries or transmission of sound that is often referred to as acoustic streaming has been the subject of a number of investigations. In a review paper, Lighthill (1978) asserts that acoustic streaming is induced by the action of Reynolds stresses, but that it is the dissipation of acoustic energy through attenuation of transmitted sound or viscous effects at an oscillating solid boundary that leads to the fluid motion.

In an analytical investigation of acoustic waves in fluids, Nyborg (1953) and Westerveldt (1953) showed that propagating and standing acoustic waves can induce steady rotational flow. In a later investigation of nonlinear acoustic streaming produced by a plane sound beam, Ostrovskii and Papilova (1974) showed that the flow velocity increases with sound attenuation although no estimate of the velocity was given. More recently, Marakov et al. (1989) experimentally investigated streaming resulting from the propagation of pulsed or continuous acoustic beams produced by a plane circular emitter operating in the megahertz range in water. Streaming velocities greater than 2 m/s were measured by analyzing flow visualization motion pictures.

A number of investigations have also been concerned with streaming associated with oscillating solid boundaries. In an analytical study of acoustic streaming produced by the time-harmonic oscillations of a cylinder normal to its axis, Stuart (1966) showed qualitative agreement with earlier experiments by Schlichting (1932) in water. Davidson and Riley (1972) investigated, analytically and experimentally, the streaming associated with an oscillating cylinder submerged in water with the same time-harmonic motion. The cylinder oscillated with an amplitude of 0.1 cm and a frequency of 45 Hz. Streaming velocities on the order of 1 cm/s were deduced from flow visualization photographs and were in agreement with the theoretical results.

In an experimental study in air, Mednikov and Novitskii (1975) produced a jet using a low frequency (10-100 Hz) oscillating plate in a resonance cavity. Average streaming velocities of up to 17 m/s were measured using a Pitot probe. Although the streaming was produced by an oscillating solid boundary, the high velocity was attributed to the presence of the resonance chamber. Acoustic streaming in air in the vicinity of orifices was studied by Lebedeva (1980). who measured velocities of up to 10 m/s when high amplitude sound waves (150dB) were transmitted through an orifice placed at the end of a tube referred to as an interferometer tube. Sheen et al.(1989) studied streaming in water due to an oscillating ultrasonic agitator consisting of a compressional transducer and a wave guide. The investigators observed both fluid streaming and cavitation on the

agitator surface and noted that streaming was present even in the absence of cavitation bubbles. An experimental investigation of streaming associated with cavitating liquid was performed by Panov and Semenova (1987) who inferred the flow velocity from motion picture analysis of hydrogen bubbles. The authors reported velocities of up to 3 m/s but noted that deceleration of the hydrogen bubbles may have led to inaccuracies in their measurements.

The present investigation is concerned with a turbulent water jet produced normal to a circular disk mounted around its perimeter and driven at its resonance frequency. The jet flow is visualized in Figure III.1b (Figure III.1a shows the undisturbed fluid in the absence of the jet). The fluid is seeded with reflective flakes (approx. 50 μm in length) and illuminated in a plane that includes the jet's axis of symmetry using a sheet of an argon Ion laser. The photograph illustrates that the jet becomes turbulent at or near the surface of the disk, and that it spreads linearly with streamwise distance. It is evident that the jet is comprised entirely of radially entrained fluid. LDA measurements have demonstrated that the streamwise velocity near the disk center exceeds 1 m/s, corresponding to a Reynolds number of approximately 2500 (based on the jet diameter of 2 mm at a distance of 2 mm from the actuator surface). The present investigation shows that the jet is produced as a result of the formation of a small cluster of cavitation bubbles near the center of the disk, which grow, become smaller and finally disappear during each excitation cycle. It is conjectured that the time-periodic formation of these bubbles displaces vorticity from the boundary layer of the actuator, and leads to the formation of vortex puffs which coalesce to form a synthesized turbulent jet.

## III.2 Experimental Apparatus and Procedure

The experiments were conducted in a small water tank measuring 26 cm x 49 cm x 29 cm. The jet is formed normal to the surface of a submerged actuator comprised of a 0.39 mm thick brass disk 18.2 mm in diameter that is driven by a concentrically mounted 0.19 mm thick piezoceramic wafer having a diameter of 11.6. The disk is soldered around its perimeter to a brass tube having an outer diameter of 19.1 and is driven at its nominal 7 kHz resonance frequency in its first axisymmetric mode of vibration using a laboratory function generator and a high voltage (max. 120 Vrms) broad band (25 Hz to 150 kHz) amplifier. The jet is formed when the excitation input to the actuator is greater than 50 Vrms, and the bulk of the measurements were taken at an excitation level of 90 Vrms. At this excitation level the amplitude of the disk displacement is approximately 10 mm (inferred from measurements of the disk surface velocity and its resonance frequency).

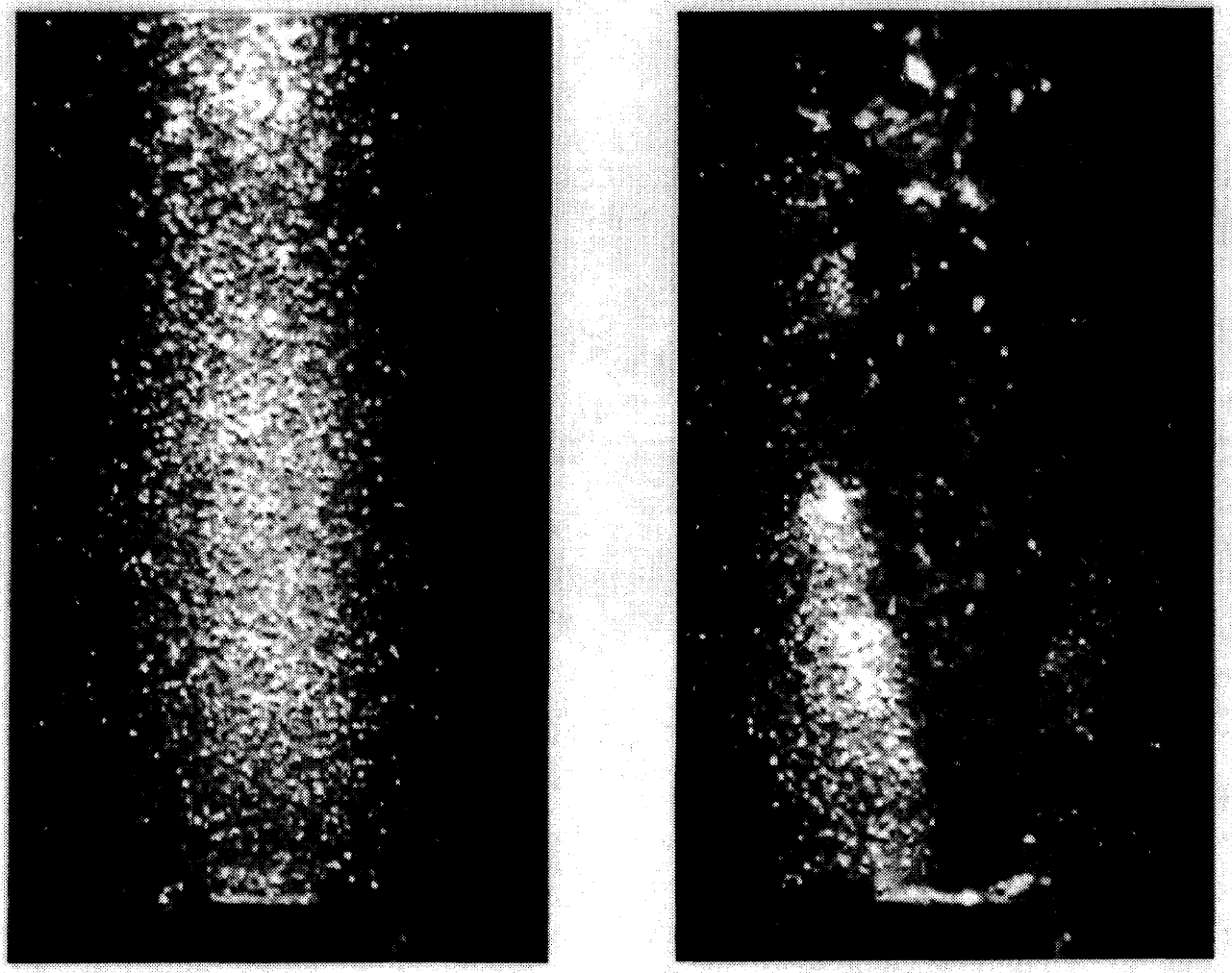

a b

Figure III.1

The transient characteristicsthe jet were studied using amplitude modulation of the input signal between 90 and 40 Vrms.

Distributions of the streamwise and radial velocity components were measured using a single component frequency-biased LDA operating in forward scatter mode (Figure III.2). The two orthogonal velocity components were measured separately by rotating the LDA optics about the optical axis of the system. The optics are mounted on a three axis computer controlled traversing mechanism allowing for easy positioning of the LDA with an accuracy of +/- 0.1 mm per 300 mm traversed. The output of the tracker type LDA processor is sampled using a PC-based data acquisition system with an 12 bit A/D converter having a maximum sample rate of 100 kHz. The velocity resolution of the data acquisition system is 1 mm/s. Radial distributions of the streamwise velocity component extending through r = 35 mm were measured at 26 equally spaced streamwise stations between x = 2 mm and x = 110 mm. Within this domain the centerline velocity decreases monotonically from 40 cm/s to 4 cm/s. At each streamwise station the measurements were taken at 35 equally spaced radial locations $0 \leq r \leq 35$ mm. In order to demonstrate the symmetry of the jet, the measurements were taken on both sides of the jet centerline. Similar distributions of the radial velocity component were also measured, but are not discussed here. Whenever an actuator was replaced in the course of the experiments, it was calibrated by adjusting the voltage input so that the streamwise velocity on the centerline at x = 4 mm remained unchanged. The velocity data was sampled at 2 kHz (a low sampling rate compared to the resonance frequency) in order to allow for long averaging time (24.5 sec.) at each measurement point. The time averaged velocity was compared with similar data sampled at 25 kHz (well above the resonance frequency), and the agreement was excellent.

## III.3 Experimental Results

Radial profiles of the time-averaged streamwise velocity for 2 mm < x < 110 mm are shown in Fig III.3 plotted in the usual similarity coordinates. Within this domain the magnitude of the streamwise velocity on the jet centerline decreases one order of magnitude from 36 cm/s to 3.5 cm/s and the jet half width increases from 1.5 to 7.9 mm. It is remarkable that virtually all profiles lie on top of one another (including those measured near the actuator surface), suggesting that the jet is self similar. A round turbulent jet typically becomes self similar several diameters downstream of the jet orifice, but in this case the self similar behavior is evident within one jet diameter suggesting rapid transition to turbulence possibly becoming turbulent at the actuator surface. The self similarity of the flow is further supported by the linear decay of the centerline velocity with streamwise

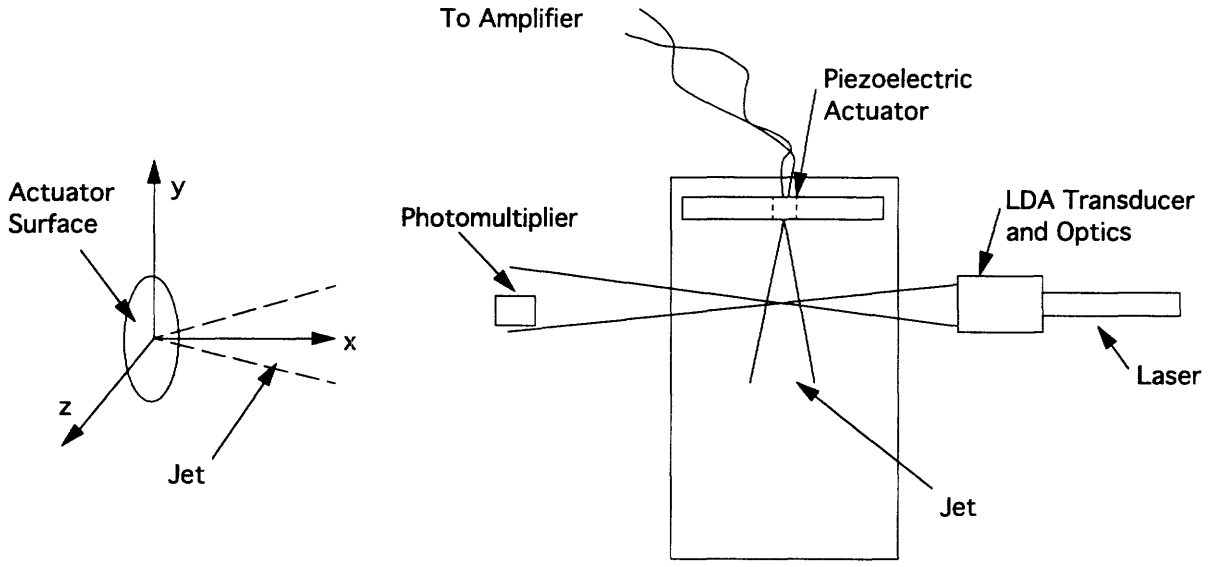


Figure III.2

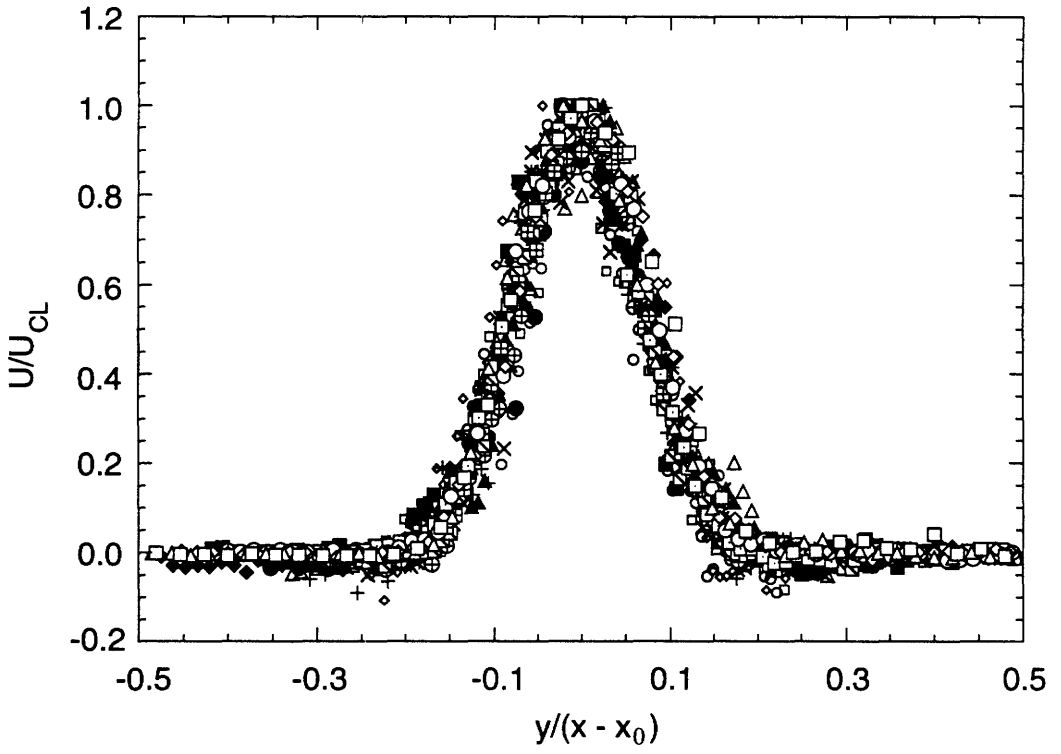


Figure III.3

distance with a slope of approximately -1 as shown in Figure III.4. It is remarkable that the synthesized turbulent jet is self similar even though it is created by the highly nonlinear oscillations of the actuator surface.

Figure III.5 shows a plot of the streamwise velocity measured on the centerline 2 mm from the actuator surface for different excitation levels. Below 50 $V_{rms}$ no jet is formed, and this level is deemed to be a threshold voltage. When the input is increased above this level, the fluid velocity increases linearly with input voltage. The surface velocity of the actuator was measured by aligning the LDA optics at a small angle relative to the actuator and placing the focal volume slightly off center on the disk surface. The measured velocity was corrected for the direction of surface motion since the angle between the optical axis and the normal to the actuator surface was known. The velocity of the surface was found to be approximately 60 cm/s which is of the same order of magnitude as the fluid velocity near the actuator surface. The disk displacement is 10 μm and is inferred from the disk velocity and frequency. Figure III.5 also shows the dependence of the disk velocity on actuator voltage. The surface velocity increases linearly until the threshold voltage is reached where the velocity levels off and remains almost constant (with some fluctuations). It is postulated that the additional energy applied to the actuator is absorbed in the production of cavitation bubbles near the center of the actuator surface as discussed below. As shown in Figure III.5, the amplitude of the spectral peak of the fluid velocity at the resonance frequency also increases linearly up to the jet threshold level where there is a sharp increase in amplitude followed by a monotonic almost linear decrease implying that above the jet threshold, the energy associated with the fluctuating component of the streamwise velocity decreases as it is transferred to the jet.

Instantaneous traces of the streamwise velocity (sampled at 80 kHz) measured on the jet centerline, 2 mm from the actuator surface for 36 Vrms and 90 Vrms are shown in Figs III.6a and III.6b, respectively. When the input excitation is below the threshold level (36 Vrms) there is no mean streamwise velocity, although an oscillatory velocity (amplitude of 20 cm/s) at the driving frequency (6.729 kHz) is clearly visible. Above the threshold level (90 Vrms) the mean velocity is approximately 60 cm/s and the amplitude of the oscillations at the resonance frequency is nominally 30 cm/s. Although the time trace in Fig III.6b is dominated by velocity fluctuations at the resonance frequency, it also exhibits lower frequencies which are presumably associated with the passage of large vortical structures.

A spectrum of the centerline (streamwise) velocity measured 20 mm downstream from the actuator surface is shown in figure III.7 The spectral component at the excitation frequency shows that the oscillatory component of the fluid velocity is prominent even in

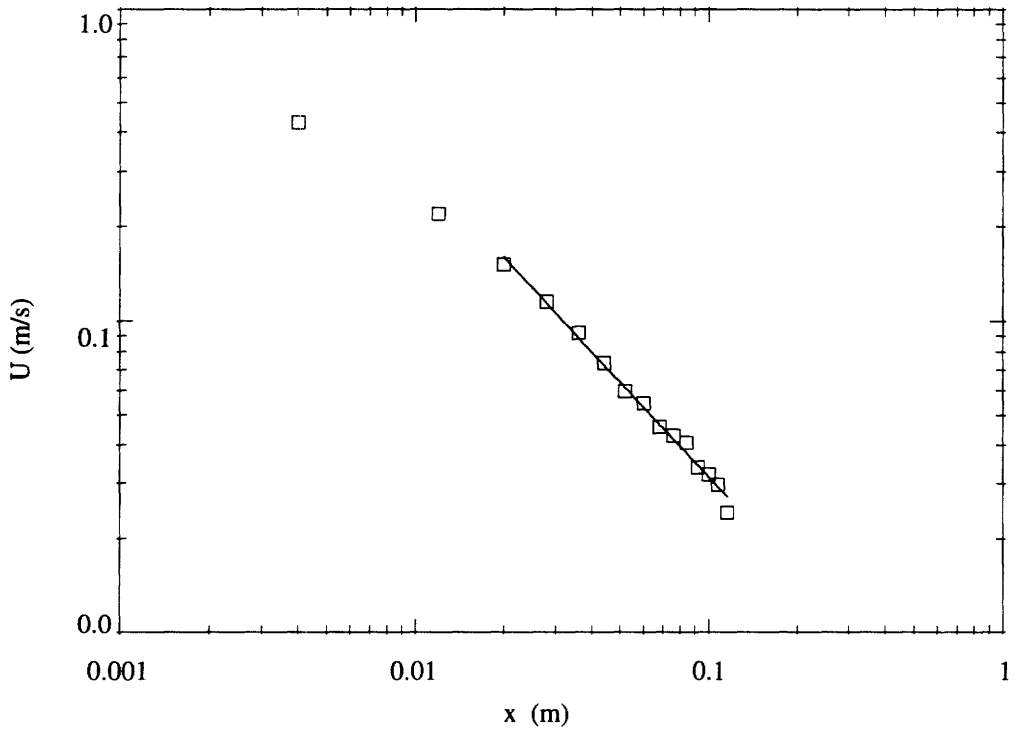


Figure III.4

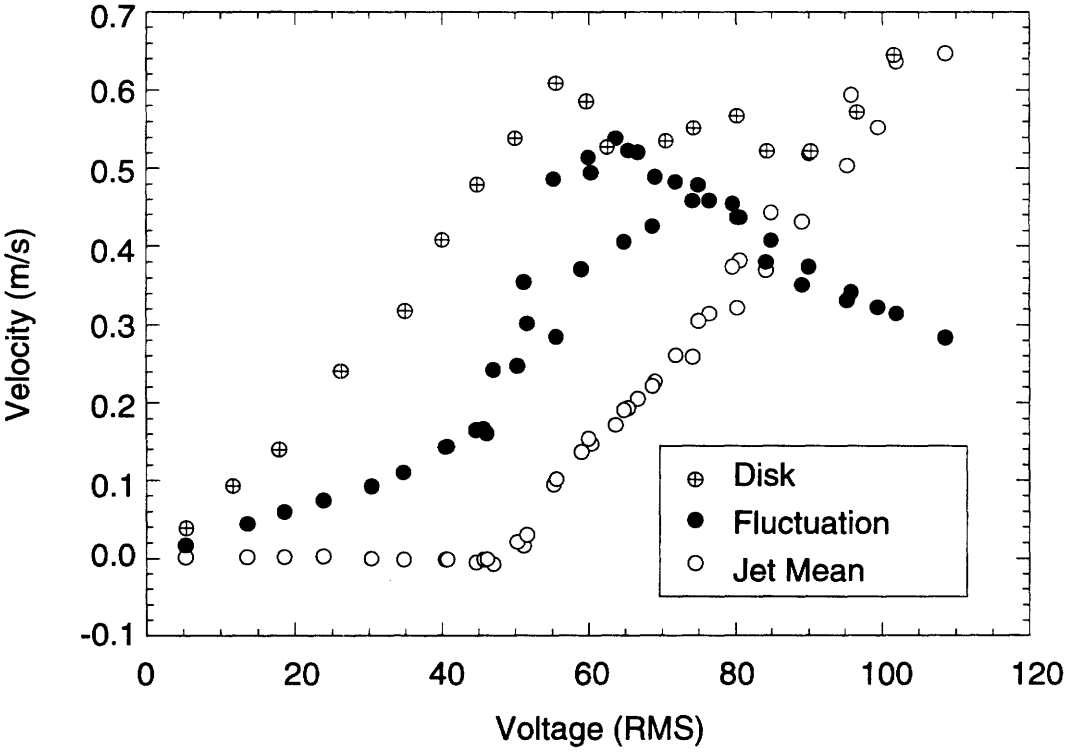


Figure III.5

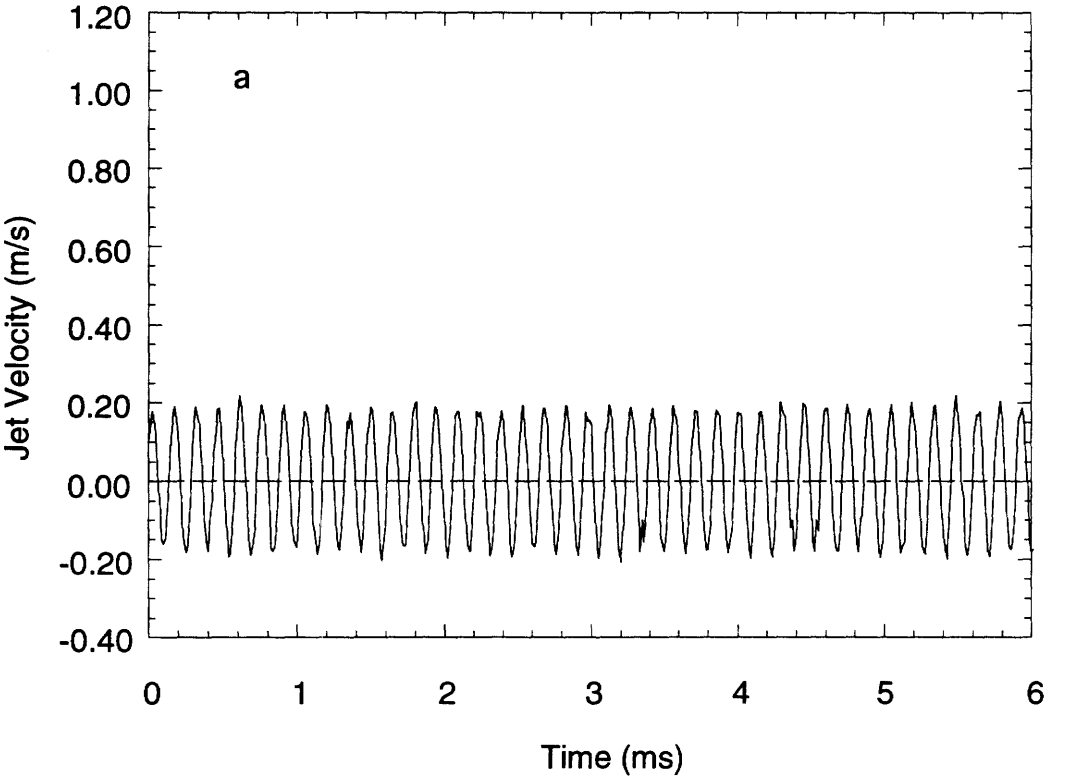
a
1.20
1.00
0.80
0.60
0.40
0.20
0.00
-0.20
-0.40
Jet Velocity (m/s)
0
1
2
3
4
5
6
Time (ms)

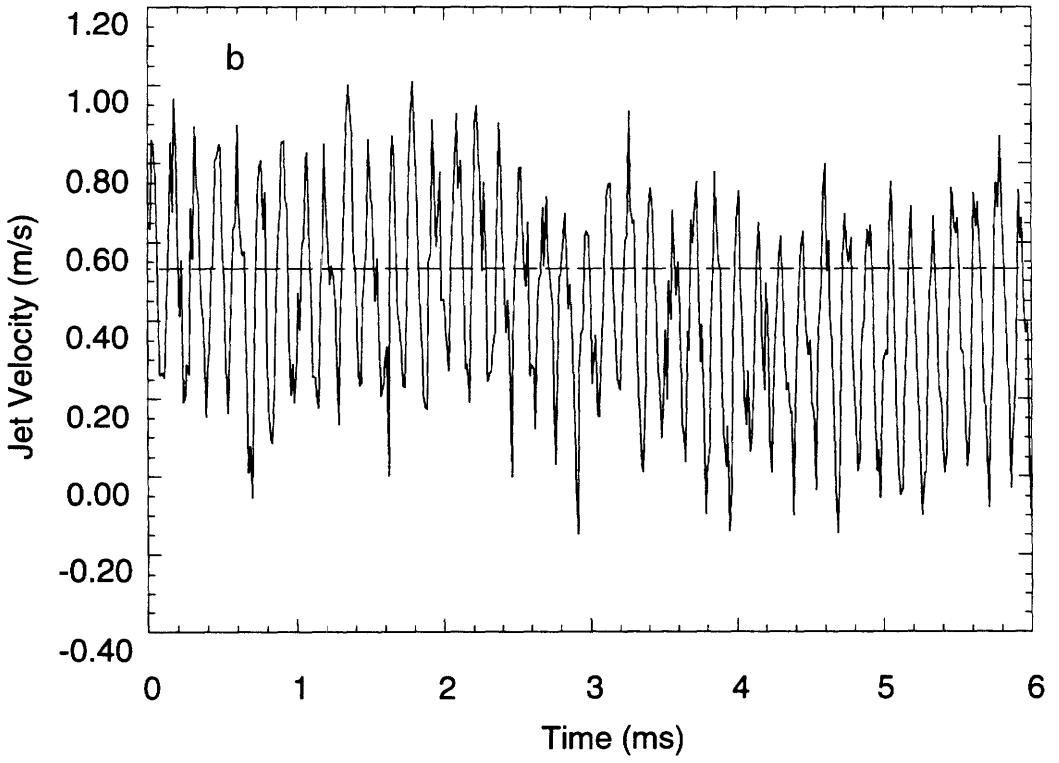
b
1.20
1.00
0.80
0.60
0.40
0.20
0.00
-0.20
-0.40
Jet Velocity (m/s)
0
1
2
3
4
5
6
Time (ms)

Figure III.6

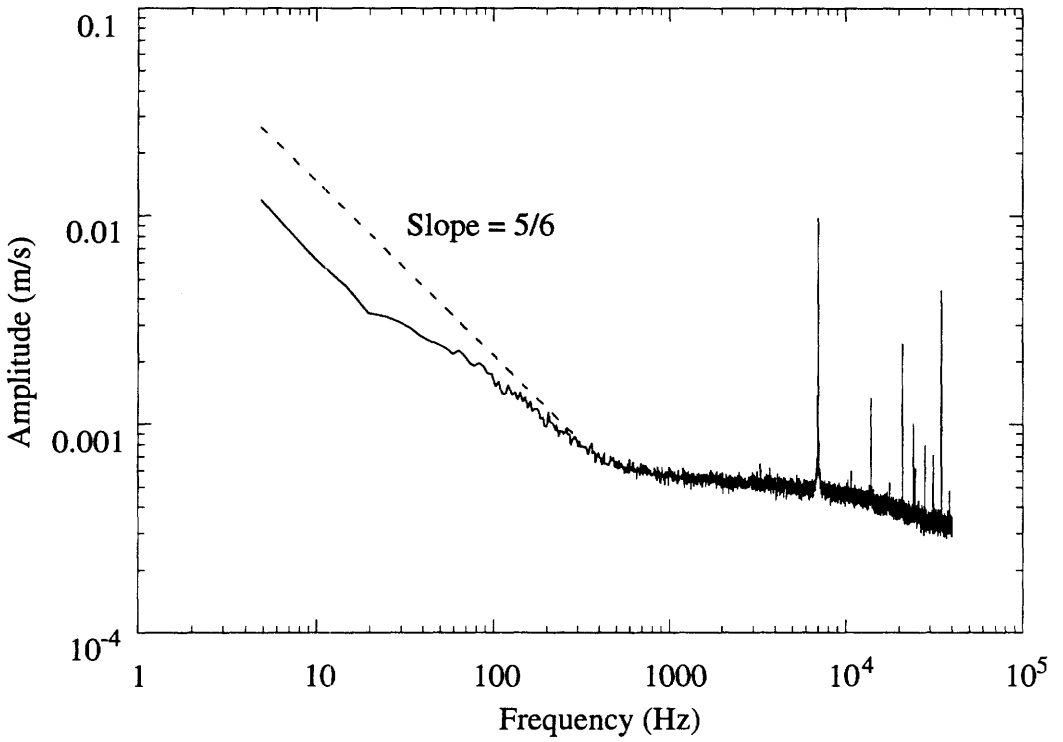


Figure III.7

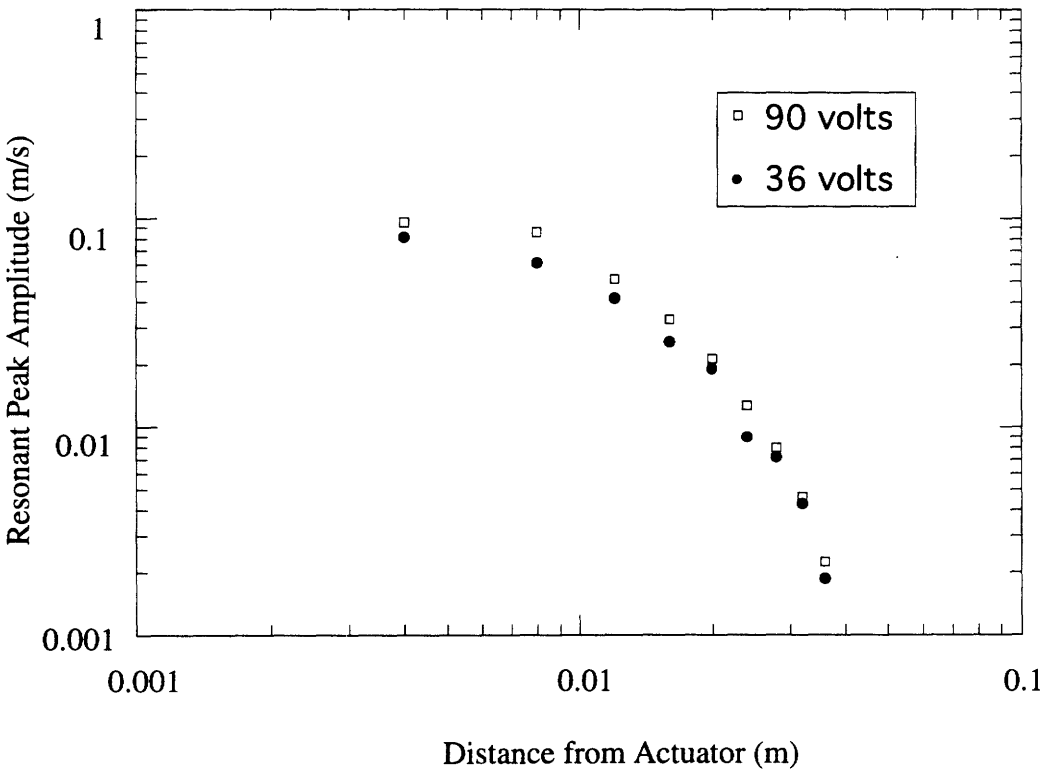


Figure III.8

the far field of the jet. It is noteworthy that the spectrum is virtually featureless below 1000 Hz and that the influence of the disk motion on the fluid flow occurs at higher frequencies. The decay of the spectral peak at the resonance frequency with streamwise distance is shown in Figure III.8 for excitation levels of 36 (below the jet threshold) and 90 volts rms. The fact that the two curves are virtually identical, indicates that the ocillatory component of the motion is merely a passive attendant to the formation of the jet.

The present investigation has demonstrated that when the excitation level of the actuator is above the jet threshold voltage, a small cluster of cavitation bubbles appear near the surface of the disk. The bubbles appear and disappear during each cycle of the disk oscillation, and their evolution was recorded in a series of photographs taken at increasing time delays relative to a zero crossing of the excitation waveform. The photographs, shown in Figure III.9, show the evolution of the bubbles at various phase angles relative to the phase angle at the instant when the disk is at $x = 0$ and moving in the streamwise direction. Figure III.9a is taken at a phase angle of 7 degrees and the phase change between successive images is 41.5 degrees. Using potential flow arguments it can be shown that the pressure on the disk is lower than ambient (but not minimum) when the disk has positive displacement since the pressure is proportional to disk acceleration. In Figure III.9b the disk displacement increases further and the local pressure near the centerline is low enough so that cavitation bubbles are formed. The bubbles continue to grow (Figure III.9c) and attain their maximum diameter of approximately 200 μm in Figure III.9d. In Figures III.9e and III.9f the disk moves in the negative x direction and as the pressure increases, the cavitation bubbles become smaller and finally disappear. The nominal bubble diameter increases to 200 μm in approximately 20 μs resulting in a growth rate of 10 m/s. That this velocity is an order of magnitude higher than the fluid velocity and the disk velocity suggests that the growth and disappearance of the cavitation bubbles play a significant role in the formation of the jet because the flow field produced near the disk surface is dominated by the higher velocity of the bubbles.

A series of tests in which the ambient pressure about the actuator was increased, were carried out to determine whether the presence of cavitation bubbles is necessary for jet formation. The actuator was placed in a pressure vessel equipped with optical windows, and the pressure on both sides of the oscillating disk was equalized to prevent net loading. The vessel was pressurized to a given level above atmospheric pressure (up to 240 kPa), and the input voltage to the actuator was slowly increased until a jet was formed. The pressure tests were repeated for various pressure levels, and it was found that the static pressure at which a jet is formed is a linear function of input voltage. Figure III.10 is a plot of the threshold voltage versus ambient pressure. Assuming the motion produced by the

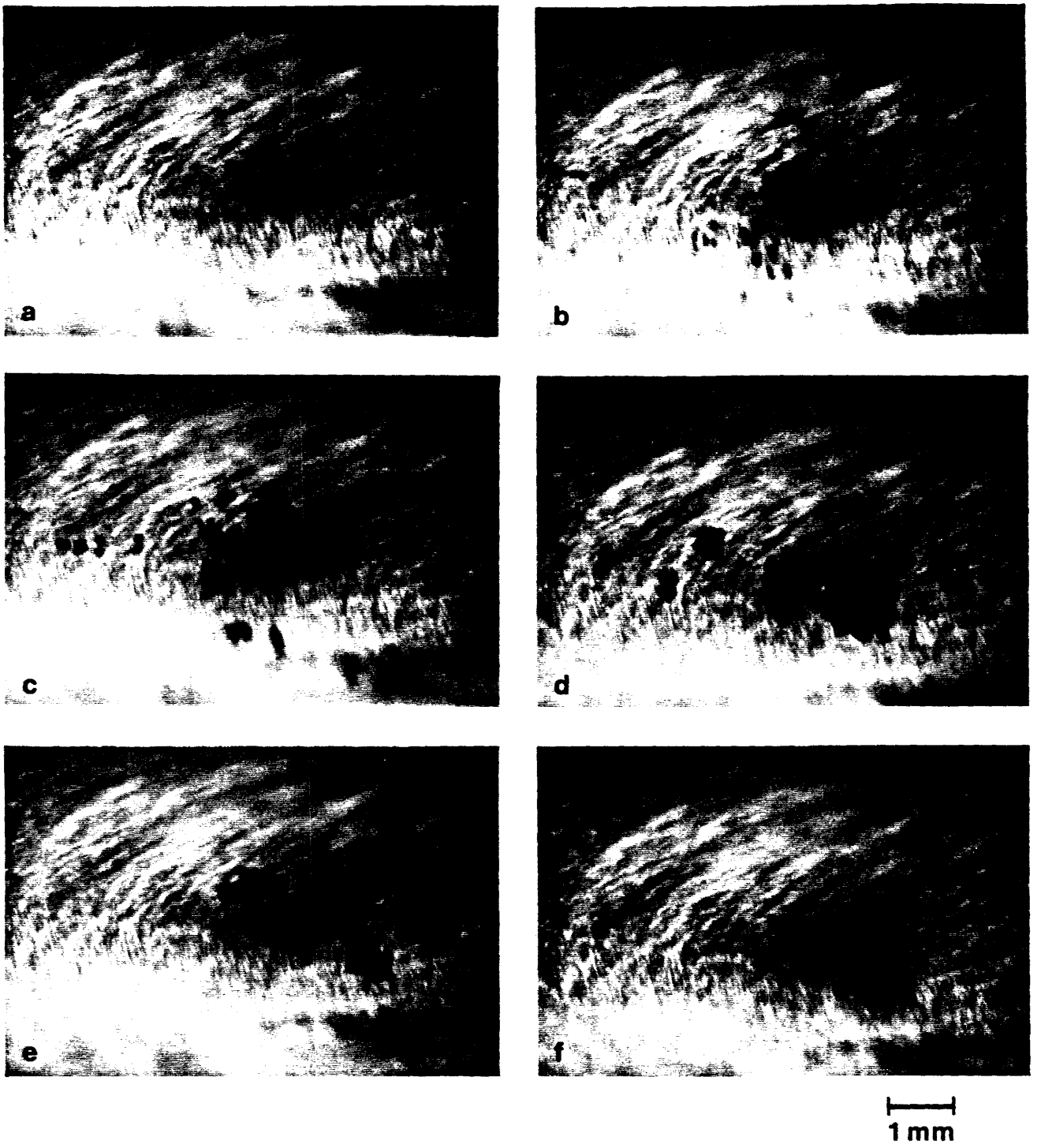


Figure III.9 . A sequence of phase delayed photographs of cavitation bubble clusters. The time delay between photographs is 18 μs, and, measuring from the time when the disk's displacement is zero and its outward velocity is positive, the phase delays are: (a) 118°, (b) 159°, (c) 201°, (d) 242°, (e) 284° and (f) 325°.

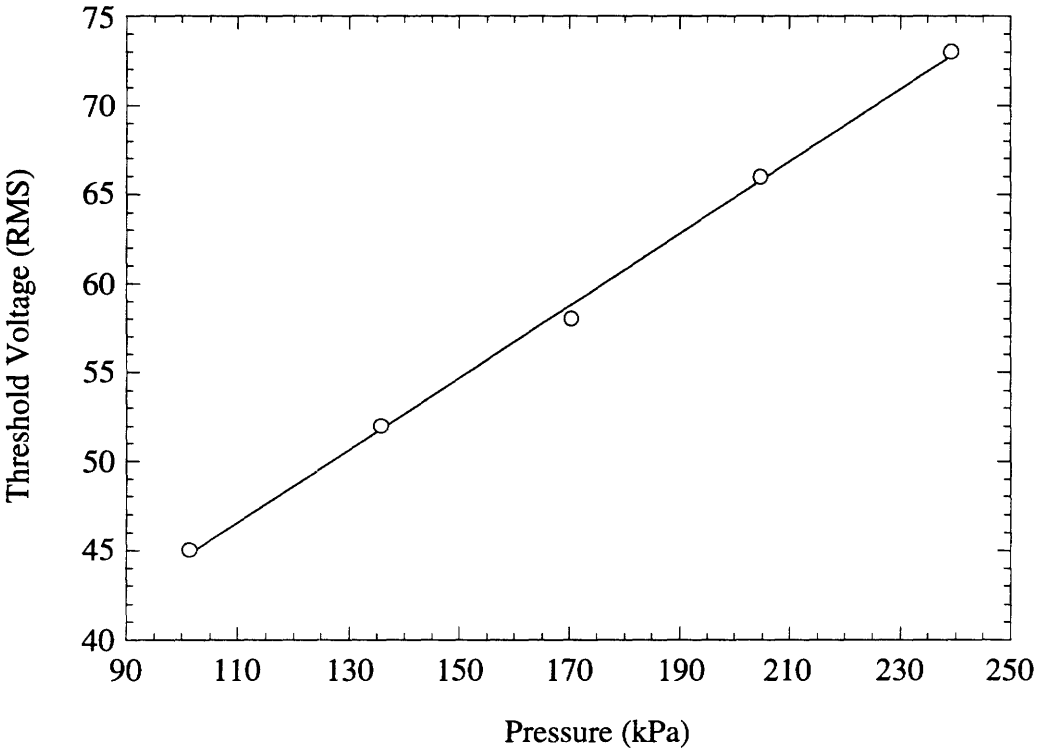


Figure III.10

vibrating disk can be modeled using potential flow theory, then the pressure on the oscillating disk at high frequency should be equal to ambient pressure plus $\rho\partial\phi/\partial t$, which is a linear function of the disk velocity ($\phi$ is the velocity potential and $\rho$ is the fluid density). The term $\partial\phi/\partial t$ is effectively the acceleration of the fluid near the disk surface and is negative when the disk is moving in the positive streamwise direction, so that as the disk moves outward the pressure near its surface is lower than ambient. As shown in Figure III.5, the fluid velocity is, for the most part, a linear function of the input voltage, and it is clear that an increase in ambient pressure can be counteracted with an increase in input voltage. The relationship between the increase in voltage and the increase of ambient pressure should be linear, and the present results are consistent with the proposed model. Furthermore, the pressure tests demonstrate that the presence of cavitation bubbles is indeed necessary for the formation of the jet.

An important feature of the present jet is that it can be turned on and off within a relatively short time. This effect is accomplished by amplitude modulation of the input signal to the actuator so that its level fluctuates above and below the threshold level necessary for jet formation. In Figures III.11a and b, the input level undergoes a step change between 40 and 90 Vrms. Time traces of the centerline velocity at x = 2 mm are presented in Figure III.11a for an "on" transition and in Figure III.11b for an "off" transition. Both traces exhibit velocity oscillations at the fundamental frequency and indicate that the average rise and fall times are about 35 cycles of the excitation frequency or about 5 ms. It should be noted that these rise and fall times include the advection time of the jet starting vortex which is approximately 2 ms; therefore, the actual transition times are on the order of 3 ms.

### III.4 Summary and Outline of Future Research

An intense turbulent jet with mean centerline velocity of up to 1 m/s is produced at the surface of an oscillating disk driven at its resonance frequency by a piezoceramic element. Although created by the strong oscillatory medium the jet behaves self similarly even within a one jet diameter from the actuator surface. While the time averaged flow appears to be self similar, the instantaneous velocity includes a strong oscillatory component at the disk frequency and turbulent fluctuations. The mean jet flow is concluded to be decoupled from and superimposed upon these fluctuating velocity components. The jet is formed when the excitation level of the actuator exceeds a given threshold. Above this level the surface oscillations of the actuator result in time-periodic low pressure and the formation and disappearance of a cluster of cavitation bubbles near the center of the actuator surface during each cycle of the excitation waveform. The fluid velocity increases linearly above the threshold input while the disk velocity remains

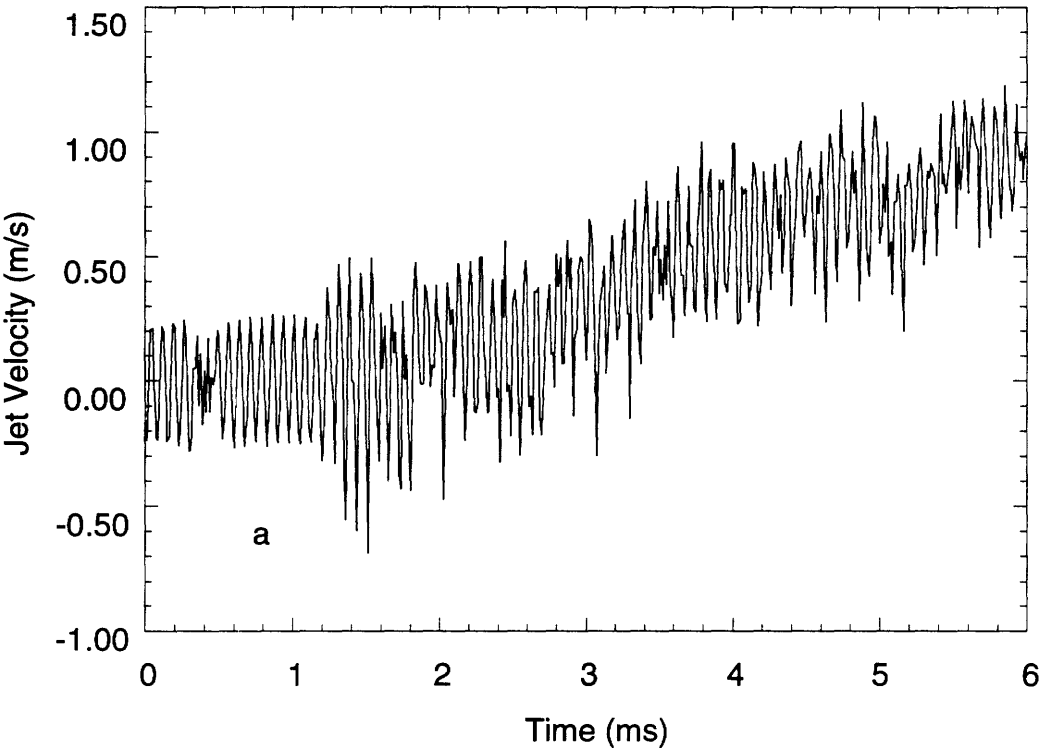


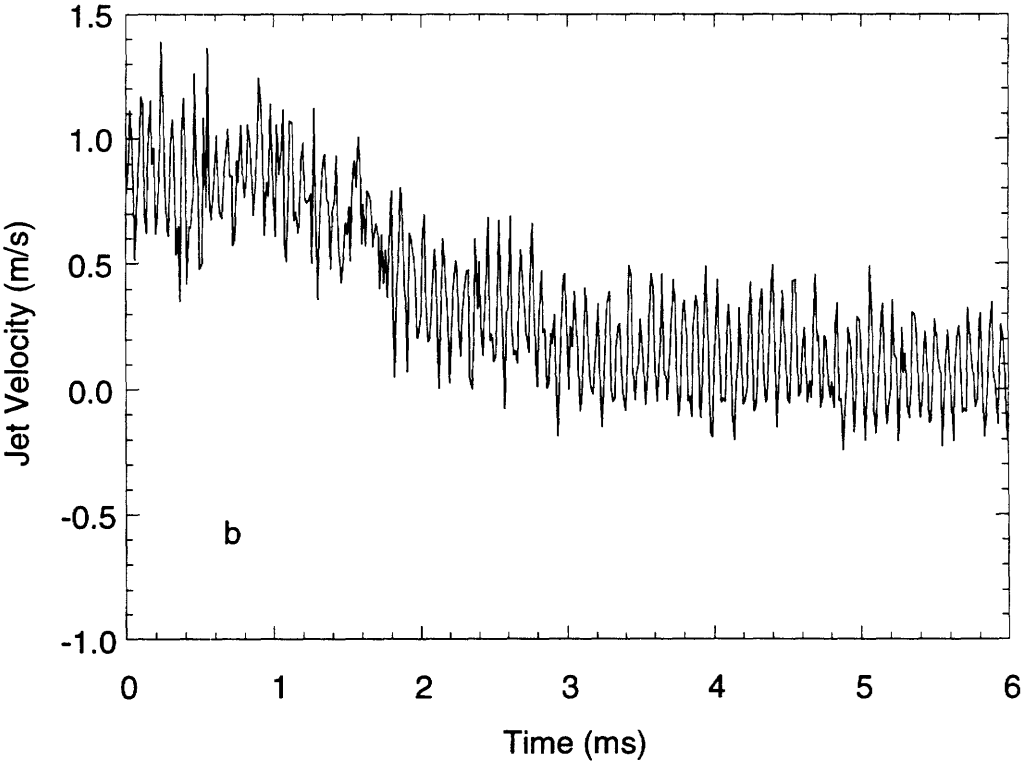


Figure III.11

constant, suggesting that the additional energy is absorbed by the growth of cavitation bubbles. It is conjectured that the cavitation bubbles displace vorticity away from the nominally axisymmetric boundary layer adjacent to the actuator surface to form vortex puffs which merge and synthesize a turbulent jet. This method of jet production distinguishes the observed phenomenon from acoustic streaming in that the jet forms not as a result of dissipated acoustic energy but as a result of the growth of the bubbles near the actuator surface. The present results also indicate that the jet can be manipulated on relatively short time scales, and this characteristic coupled with the fact that the jet is comprised entirely of radially entrained fluid suggests that the synthesized jet may be effectively utilized for the control of wall bounded shear flows.

During the second year of this Grant, we will focus on the implementation of surface jets in air. The underlying mechanism of vorticity shedding from an oscillating (Stokes) surface boundary layer is similar to that of the water experiments. In the air experiments the actuators form the bottom of a (sealed) pillbox beneath the surface, and axisymmetric or two-dimensional jets are formed at the edges of orifices through the time-periodic formation of vortical puffs at the resonance frequency of the actuator. The interaction between the surface (zero mass) jets and free shear flows will be investigated with particular emphasis on thrust vectoring and the controlled formation of streamwise vortices.

## IV. Optical Measurements of Conserved Scalars Concentrations

We have begun to develop an optical technique which will enable direct simultaneous measurements of instantaneous temperature and species concentration fields in our plane shear layer facility. The significance of these two independent measurements in water is that the relevant dimensionless diffusion parameters, namely the Prandtl number (Pr = 7) for the temperature field and the Schmidt number (Sc = 1000) for the species concentration field, differ by two orders of magnitude. Hence, these field measurements will allow for a simultaneous study of the dynamics of mixing in the forced and unforced flow for two different diffusion parameters, where one of the diffusion parameters (Pr number) is close to the diffusion parameter in air (Sc = 1 in air). Furthermore, this capability will enable us to develop performance measures for mixing for real-time open- and closed-loop control applications.

Another important attribute of the simultaneous measurements of two scalar fields having different diffusion properties is that in a nonisothermal flow in which compressible and viscous heating are negligible, the equations for conservation of mass, energy, and species concentration involve five unknowns (three velocity components, temperature and concentration). If full field measurements of two of these unknowns are available, then one can, in principle, solve for the three velocity components (Pearlstein 1991). As noted by Pearlstein, the three velocity components appear linearly in the convective terms of the energy and concentration equations. In the continuity equation u,v, and w also appear linearly in the form of their x, y, and z derivatives, respectively.

Instantaneous temperature distributions (which will enable us to compute the degree of mixedness) will be measured in planar cross sections of the shear layer using temperature-sensitive fluorescent dye such as Rhodamine B (Liu, Campbell, and Sullivan 1993). The dye is uniformly mixed in both streams of the shear layer and is excited (at 514 nm) in cross-stream or spanwise planes using a sheet of light from an argon Ion laser. The fluorescence intensity decreases approximately linearly with temperature between 0°C and 50°C. The emitted light will be wavelength-separated and simultaneously recorded by a phototrnsitor array camera equipped with standard optical filters. The laser sheet will be rapidly scanned through the flow to obtain a three-dimensional temperature field using digital image processing techniques.

A new highly-sensitive camera was designed and constructed specifically for the present real-time temperature measurements. The camera which is based on a silicon retinae, is necessary because of the relatively small variations in fluorescence intensity within the range over which temperature may be considered a passive scalar without affectting the flow due to buoyancy effects (approximatelt 5°C). Silicon retinae are not

new. Previous designs have employed sub-threshold circuits and saturating active resistive elements (grids). While these weak-inversion implementations do provide the advantage of low-power circuits, they have a number of shortcomings. Of particular note are: a) large random offsets due to exponential dependence on parameter variation accross the die, b) small signal to noise ratios due to their small dynamic range, and c) the active resistive grid suffers from spontaneous oscillations due to the massive interconnection of active elments, even though individual elements may be stable. Succesfull methods for controlling the offset have been developed (using UV, floating gate technologies, and adaptive offset compensation filters). However the two latter problems still persists.

To avoid the shorcomings of present designs, a strong inversion circuit with passive resistive grid has been designed and constructed. The offset is controlled by carefull design and layout practices.

The first generation chip is a linear array of 256 parasitic bipolar phototransistors each measuring 50μm x 50μm. The photocurrent is subsequently used to produce the voltage to a high-speed four quadrant multiplier. Due to the exponential nature of subthreshold devices, the linear output current of the phototransistors is converted to logarithmic voltage. A logarithmic response is desirable because it allows the sensors to respond over a large (8 orders of magnitude) intensity range without saturation. Once a temperaturen image is acquired, the voltage level of each synaptic capacitor is maintained despite parasitic lrakage currents by a using a refreshing circuit based on an analog-to-digital-to-analog conversion. The array aquisition time is 50ns, and the data can be clocked out at the same speed so that in principle the array can be downloaded within 13 μsec. The layout of a single sensor is shown in the figure on the next page.

In the present design, the outputs of the two groups of phototransistors 1 - 8 and 249 - 256 are (time) averaged and used as temperature references $T_C$ and $T_H$. It is noted that for the shear layer experiments $T_C$ and $T_H$ are the temperatures of the cold and hot streams, respectively. The reference temperatures are internally subtracted from the temperature measured by each phototransistor $T_i$ so that the output of the array is $T_i - T_C$ and $T_H - T_i$ along with $T_H - T_C$. This arrangement enables measurements of extremely small temperature differences relative to the reference temperature without noise contamination.

**Outline of Future Research**

Measurements of the temperature field in our mixing layer facility will be used for monitoring and control of mixing. In addition to the temperature measurements we also plan to measure the concentration field of water-soluble dye so that we are able to compute the velocity field using the algorithm developed by Pearlstein for two independent scalar

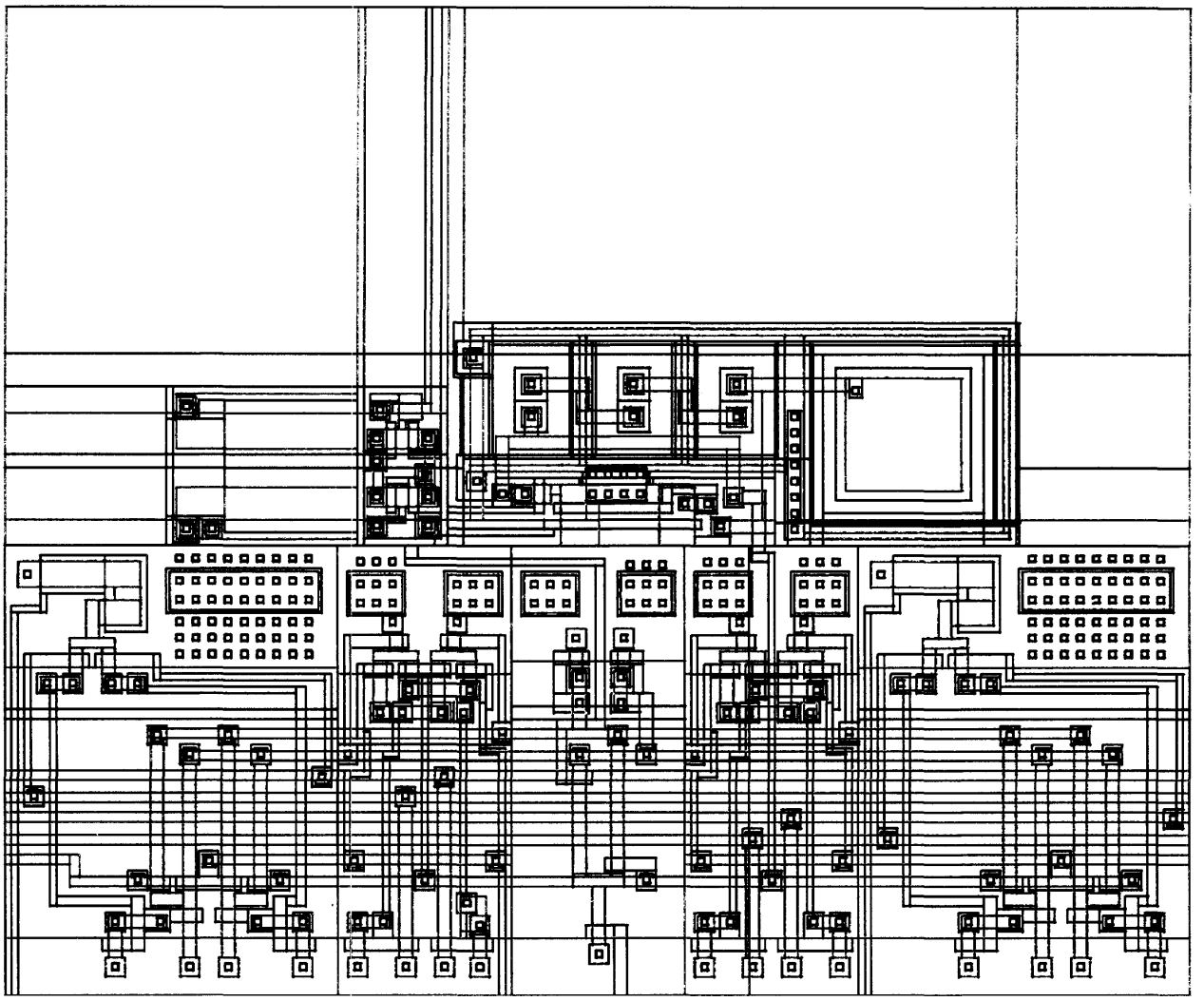

fields. Because the use of dyes to measure mixing in a closed-return facility presents obvious difficulties with time-dependent accumulation which degrades the quality of the experiment, we will employ a new technique utilizing light attenuation by photochromic dyes. These measurements will be taken concomitantly with the temperature measurements using essentially the same laser and imaging system.

## References

Anke, D., "Luftschallwandler nach dem Sell-Prinzip für Frequenzen von 50 kHz bis 100 kHz," *Acoustica* **30**, 30 (1974).

Baerg W., & W. H. Schwarz, "Measurement of the scattering of sound from turbulence," *J. Acoust. Soc. Am.*, **39**, 1125 (1965).

Baudet, C., S. Ciliberto & J. F. Pinton, "Spectral analysis of the von Karman flow using ultrasound scattering," *Phys. Rev. Lett.* **67**, 193 (1991).

Bass, H. E., L. N. Bolen, R. Raspet, W. E. McBride & J. Noble, "Acoustic propagation through a turbulent atmosphere: experimental characterization," *J. Acoust. Soc. Am.*, **90**, 3307 (1991).

Cantwell, B. J., "Viscous Starting Jets," *Journal of Fluid Mechanics*, **173**, 159-189, 1986.

Chigier N. A. & A. Chervinsky, "Experimental investigation of swirling vortex motion in jets," *J. Appl. Mech.* **34**, 443 (1967).

Contreras H. & F. Lund, "Ultrasound as a probe of turbulence II: Temperature inhomogeneities," *Phys. Lett. A* **149**, 127 (1990).

Davidson, B.J. & Riley, N., "Jets Induced by Oscillatory Motion," *Journal of Fluid Mechanics*, **53**, 287, 1972.

Engler, R. H., D. W. Schmidt & W. J. Wagner, "Nondisturbing acoustical measurements of flow fields -- new developments and applications," *J. Acoust. Soc. Am.*, **85**, 72 (1989) and references therein.

Ho, C.-M. & L. S. G. Kovasznay, "Propagation of a coherent acoustic wave through a turbulent field," *J. Acoust. Soc. Am.*, **60**, 40 (1976).

Kallistratova, M. A. "Procedure for investigating sound scattering in the atmosphere," *Sov. Phys. Acoustics*, **5**, 512 (1959).

Korman, M. S. & R. T. Beyer, "The scattering of sound by turbulence in water," *J. Acoust. Soc. Am.*, **84**, 339 (1988).

Kraichnan, R. H. "The scattering of sound in a turbulent medium," *J. Acoust. Soc. Am.*, **25**, 1096 (1953).

Landau, L. D. & E. M. Lifshitz, *Fluid Mechanics*, Pergamon Press, 1975.

Lighthill, M. J., "On the energy scattered from the interaction of turbulence with sound or shock waves," *Proc. Camb. Phil. Soc.*, **49**, 531 (1953).

Lighthill, M.J., "Acoustic Streaming," *Journal of Sound and Vibration*, **61**(3), 391-418, 1978.

Lindsay, R. B., "Compressional wave front propagation through a simple vortex," *J. Acoust. Soc. Am.* **20**, 89 (1948).

Liu, T., & B. T. Campbell, & J. P. Sullivan, "Thermal Paints for Shock/Boundary Layer Interaction," *AIAA Paper* 92-3626, 1992.

Lund, F., "Response of a filamentary vortex to sound," *Phys. Fluids A* **1, 1521-1531** (1989).

Lund, F.& C. Rojas, "Ultrasound as a probe of turbulence," *Physica D* **37**, 508 (1989).

Makarov, S.N., Semenova, N.G. and Smirnov, V.E., "Acoustic Streaming Model for an Intense Sound Beam in Free Space," *Fluid Dynamics*, **24**(6), 823-826, 1989.

McBride, W. E., H. E. Bass, R. Raspet, & K. E. Gilbert, "Scattering of sound by atmospheric turbulence: a numerical simulation above a complex impedance boundary," *J. Acoust. Soc. Am.*, **90**, 3314 (1991).

McBride, W. E., H. E. Bass, R. Raspet, & K. E. Gilbert, "Scattering of sound by atmospheric turbulence: Predictions in a refractive shadow zone," *J. Acoust. Soc. Am.*, **91**, 1336 (1992).

Mednikov, E.P. and Novitskii, B.G., "Experimental Study of Intense Acoustic Streaming," *Soviet Physics Acoustics*, **21**(2), 152-154, 1975.

Möhring, W., "On vortex sound at low Mach number," *J. Fluid Mech.* **85**, 685 (1978).

Monin, A. S. & A. M. Yaglom, *Statistical Fluid Mechanics*, MIT Press, (1980)
Rajaratnam, N., *Turbulent Jets* , Elsevier,1976.

Nyborg, W.L., "Acoustic Streaming Due to Attenuated Plane Waves," *Journal of the Acoustical Society of America*, **25**, 68-75, 1953.

Ostrovskii, L.A. and Papilova, I.A., "Nonlinear Acoustic Streaming," *Soviet Physics Acoustics*, **20** 79-86, 1974.

Rojas, C., "Scattering de Sonido por turbulencias", Magister Thesis, Universidad de Chile, 1988 (unpublished).

Rose, W. G., "A swirling round turbulent jet," *J. Appl. Mech.* **29**, 615 (1962).

Schlichting, H., "*Berechnung ebner periodisher Grenzschichtstromungen*," Phys. Z., **33**, 327-35, 1932.

Sheen, S.H., Lawrence, W.P. and Raptis, A.C., "Cavitation-Controlled Ultrasonic Agitator," *Proceedings of the IEEE 1989 Ultrasonics Symposium*, **1**, 653-656, 1989.

Sislian, J. P. & R. A. Cusworth, "Laser Doppler velocimetry measurements of mean velocity and turbulent stress tensor components in a free isothermal swirling jet," *UTIAS Report*, No. 281 (1984).

Sozou, C., "Development of the Flow Field of a Point Source in an Infinite Fluid," *Journal of Fluid Mechanics*, **91**, 541-546, 1979.

Stuart, J.T., "Double Boundary Layers in Oscillatory Viscous Flow," *Journal of Fluid Mechanics*, **24**, 673-687, 1966.

Tatarskii, V. I., "The effects of the turbulent atmosphere on wave propagation," *Natl. Tach. Inf.* Ser. TT 68-50464, Springfield, VA (1971).

Voropayev, S.I. and Afanesyev, Ya.D., "Vortex Quadrupoles and Two-Dimensional Oscillating Grid Turbulence," *Applied Scientific Research*, **51**, 475-480, 1993.

Wallace, J. M., "Methods of measuringvorticity in turbulent flows," *Exp. Fluids* **4**, 61 (1986).

Westerveldt, P.J., "The Theory of Steady Rotational Flow Generated by a Sound Field," *Journal of the Acoustical Society of America*, **25**, 60-67, 1953.

E-25-X49 2

# REPORT OF INVENTIONS AND SUBCONTRACTS

*(Pursuant to "Patent Rights" Contract Clause) (See Instructions on Reverse Side.)*

*Form Approved OMB No. 0704-0297 Expires Jun 30, 1992*



| 1a. NAME OF CONTRACTOR / SUBCONTRACTOR | c. CONTRACT NUMBER | 2a. NAME OF GOVERNMENT PRIME CONTRACTOR | c. CONTRACT NUMBER | 3. TYPE OF REPORT (X one) |
|---|---|---|---|---|
| Georgia Tech Research Corp. | F49620-92-J-0518 | | | X a. INTERIM ☐ b. FINAL |
| **b. ADDRESS (Include ZIP Code)** | **d. AWARD DATE (YYMMDD)** | **b. ADDRESS (Include ZIP Code)** | **d. AWARD DATE (YYMMDD)** | **4. REPORTING PERIOD (YYMMDD)** |
| Atlanta, GA 30332 | 920915 | | | a. FROM 930915 |
| | | | | b. TO 940914 |

## SECTION I – SUBJECT INVENTIONS

**5. "SUBJECT INVENTIONS" REQUIRED TO BE REPORTED BY CONTRACTOR / SUBCONTRACTOR (If "None," so state)**

| a. NAME(S) OF INVENTOR(S) (Last, First, MI) | b. TITLE OF INVENTION(S) | c. DISCLOSURE NO., PATENT APPLICATION SERIAL NO. OR PATENT NO. | d. ELECTION TO FILE PATENT APPLICATIONS | | | | e. CONFIRMATORY INSTRUMENT OR ASSIGNMENT FORWARDED TO CONTRACTING OFFICER | |
|---|---|---|---|---|---|---|---|---|
| | | | (1) United States | | (2) Foreign | | | |
| | | | (a) Yes | (b) No | (a) Yes | (b) No | (1) Yes | (2) No |
| | None | | | | | | | |

| f. EMPLOYER OF INVENTOR(S) NOT EMPLOYED BY CONTRACTOR / SUBCONTRACTOR | | g. ELECTED FOREIGN COUNTRIES IN WHICH A PATENT APPLICATION WILL BE FILED | |
|---|---|---|---|
| (1) (a) Name of Inventor (Last, First, MI) | (2) (a) Name of Inventor (Last, First, MI) | (1) Title of Invention | (2) Foreign Countries of Patent Application |
| (b) Name of Employer | (b) Name of Employer | | |
| (c) Address of Employer (Include ZIP Code) | (c) Address of Employer (Include ZIP Code) | | |

## SECTION II – SUBCONTRACTS (Containing a "Patent Rights" clause)

**6. SUBCONTRACTS AWARDED BY CONTRACTOR / SUBCONTRACTOR (If "None," so state)**

| a. NAME OF SUBCONTRACTOR(S) | b. ADDRESS (Include ZIP Code) | c. SUBCONTRACT NO.(S) | d. DFAR "PATENT RIGHTS" | | e. DESCRIPTION OF WORK TO BE PERFORMED UNDER SUBCONTRACT(S) | f. SUBCONTRACT DATES (YYMMDD) | |
|---|---|---|---|---|---|---|---|
| | | | (1) Clause Number | (2) Date (YYMM) | | (1) Award | (2) Estimated Completion |
| | None | | | | | | |

## SECTION III – CERTIFICATION

| 7. CERTIFICATION OF REPORT BY CONTRACTOR / SUBCONTRACTOR | (Not required if | | Small Business or | X | Non-Profit organization.) (X appropriate box) |
|---|---|---|---|---|---|
| a. NAME OF AUTHORIZED CONTRACTOR / SUBCONTRACTOR OFFICIAL (Last, First, MI) | c. I certify that the reporting party has procedures for prompt identification and timely disclosure of "Subject Inventions," that such procedures have been followed and that all "Subject Inventions" have been reported. | | | | |
| Rowland, Anita D. | | | | | |
| b. TITLE | d. SIGNATURE | | | | e. DATE SIGNED |
| Contracting Officer | | | | | 941129 |

DD Form 882, OCT 89 *Previous editions are obsolete.* 971/284

# DD FORM 882 INSTRUCTIONS

**GENERAL**

This form is for use in submitting INTERIM and FINAL invention reports to the Contracting Officer and for use in the prompt notification of the award of subcontracts containing a "Patent Rights" clause. If the form does not afford sufficient space, multiple forms may be used or plain sheets of paper with proper identification of information by Item Number may be attached.

An INTERIM report is due at least every 12 months from the date of contract award and shall include (a) a listing of "Subject Inventions" during the reporting period, (b) a certification of compliance with required invention identification and disclosure procedures together with a certification of reporting of all "Subject Inventions," and (c) any required information not previously reported on subcontracts awarded during the reporting period and containing a "Patent Rights" clause.

A FINAL report is due within 6 months if contractor is a small business firm or domestic nonprofit organization and within 3 months for all others after completion of the contract work and shall include (a) a listing of all "Subject Inventions" required by the contract to be reported, and (b) any required information not previously reported on subcontracts awarded during the course of or under the contract and containing a "Patent Rights" clause.

While the form may be used for simultaneously reporting inventions and subcontracts, it may also be used for reporting, promptly after award, subcontracts containing a "Patent Rights" clause.

Dates shall be entered where indicated in certain Items on this form and shall be entered in four or six digit numbers in the order of year and month (YYMM) or year, month and day (YYMMDD). Example: April 1986 should be entered as 8604 and April 15, 1986 should be entered as 860415.

**Item 1a.** Self-explanatory.

**Item 1b.** Self-explanatory.

**Item 1c.** If "same" as item 2c, so state.

**Item 1d.** Self-explanatory.

**Item 2a.** If "same" as item 1a, so state.

**Item 2b.** Self-explanatory.

**Item 2c.** Procurement Instrument Identification (PII) number of contract (DFAR 4.7003).

**Item 2d thru 5e.** Self-explanatory.

**Item 5f.** The name and address of the employer of each inventor not employed by the contractor or subcontractor is needed because the Government's rights in a reported invention may not be determined solely by the terms of the "Patent Rights" clause in the contract.

Example 1: If an invention is made by a Government employee assigned to work with a contractor, the Government rights in such an invention will be determined under Executive Order 10096.

Example 2: If an invention is made under a contract by joint inventors and one of the inventors is a Government employee, the Government's rights in such an inventor's interest in the invention will also be determined under Executive Order 10096, except where the contractor is a small business or nonprofit organization, in which case the provisions of Section 202 (e) of P.L. 96-517 will apply.

**Item 5g (1).** Self-explanatory.

**Item 5g (2).** Self-explanatory with the exception that the contractor or subcontractor shall indicate, if known at the time of this report, whether applications will be filed under either the Patent Cooperation Treaty (PCT) or the European Patent Convention (EPC). If such is known, the letters PCT or EPC shall be entered after each listed country.

**Item 6a.** Self-explanatory.

**Item 6b.** Self-explanatory.

**Item 6c.** Self-explanatory.

**Item 6d.** Patents Rights Clauses are located in FAR 52.227.

**Item 6e thru 7b.** Self-explanatory.

**Item 7c.** Certification not required by small business firms and domestic nonprofit organizations.

E-25-X49 #3

# NOVEL DIAGNOSTIC TECHNIQUES AND ACTUATOR TECHNOLOGY FOR TURBULENT SHEAR FLOWS

## AFOSR GRANT F49620-92-J-0518

## PROGRESS REPORT
**September 1, 1994 - August 31, 1995**

**Submitted to**

Dr. James M. McMichael
Air Force Office of Scientific Research
Bolling Air Force Base, Building 410
Washington, D.C. 20332

**submitted by**

Dr. Ari Glezer
Woodruff School of Mechanical Engineering
Georgia Institute of Technology
Atlanta, GA 30332-0405

# I. OBJECTIVES

The primary objectives of the present research are:

i. the development of novel actuator technology for flow control via vorticity micro-manipulation,

ii. a study of the interaction between these actuators and an embedding flow (e.g., thrust vectoring),

iii. a study of a new approach to mixing enhancement by *direct* manipulation of the small scales of the base flow using piezoelectric actuators,

and

iv. the development a novel diagnostic technique for nonintrusive measurements of vorticity concentrations based on ultrasound scattering.

# II. ABSTRACT OF PROGRESS

## II.1. Synthetic Jet Actuators

A new approach to the manipulation and control of shear flows using novel fluidic technology based on synthetic jets has been developed. These jets have the unique property of being *zero-mass-flux* in nature; i.e., they are synthesized from the working fluid in the flow system in which they are embedded. Although there is no net mass injection into the overall system, the jets allow momentum transfer into the embedding flow. The interaction of synthetic jets and an embedding flow near the flow boundary leads to the formation of closed recirculation regions and thus an *apparent* modification of the flow boundary. *These features enable synthetic jets to effect significant global modifications in embedding flows on scales that are one to two orders of magnitude larger than the characteristic length scale of the jets themselves.*

## II.2. Vectoring of a High Aspect Ratio Rectangular Air Jet

The vectoring of a 7 m/sec, 7.62 x 1.27 cm rectangular jet by co-flowing, millimeter-scale control jets is investigated using flow visualization and hot wire anemometry. The control jets which are based on synthetic flow technology and have an orifice width of 0.5 mm span the entire width of the primary jet nozzle and are placed along each of the long sides and near the exit plane of the primary jet. The ratio of the momentum flux in the cross-stream plane between each control jet and the primary jet is 1:35. The present experiments have demonstrated that each control jet can vector the primary jet at angles exceeding $\pm 30^{o}$ without an appreciable increase in the cross-stream spreading of the primary jet. A unique feature of the synthetic jet actuators is that *vectoring can be directed either towards or away from the actuator.* Thus, when the two control are operated in concert, the primary jet is vectored at angles exceeding $\pm 80^{o}$. Strong instabilities of the jet column are excited when the control jets are amplitude-modulated resulting in substantial increase in small scale motions and entrainment into the primary jet and thus increased levels of mixedness.

## II.3. Direct Excitation of Small-Scale Motions in Turbulent Shear Flows

Control of small-scale mixing in free shear flows by manipulation of global two- and three-dimensional instability modes and the ensuing vortical structures, depends on the classical cascading mechanism to transfer control influence to the scales at which molecular mixing occurs. Thus, mixing at the smallest scales in fully turbulent flows is *indirect* and only *weakly coupled* to the control input. The concept of direct excitation of the small

scales that bypasses the conventional energy cascade is demonstrated by forcing a shear layer segment near the exit plane of an air jet emanating from a square conduit (3.81 x 3.81 cm, 6.5 m/sec) near the passage frequency of the Kolmogorov scale. Distributions of the streamwise velocity component are measured upstream of the interaction of the four shear layer segments using hot wire anemometry. It is found that when the flow is forced, the dissipation increases by more than an order of magnitude relative to the unforced flow. Moreover, the rate of decay of turbulent kinetic energy is increased, along with energy transfer from the large scales to the small scales. Excitation of a number of discrete wavenumbers within the dissipation range of the jet shear layer, using amplitude modulation of the excitation waveform, leads to the emergence of discrete wavenumbers one to two orders of magnitude smaller.

## II.4. Vorticity Measurements in a Swirling Jet Using Ultrasound Scattering

That ultrasound scattering can be used as a non-intrusive spectral probe of vorticity and potentially as a tool for direct measurements of vorticity distributions is demonstrated in a swirling air jet by exploiting the linear relationship between the Fourier component of the scattered acoustic pressure from an ultrasonic plane wave that is propagating through the flow and the Fourier transform of the vorticity component. The measured vorticity component is normal to the plane defined by the wave vectors of the incident and scattered acoustic waves. The swirling air jet emenates from a 2.54 cm diameter nozzle and the swirl (swirl numbers up to 0.4 are realized) is generated upstream of the jet nozzle by a rotating paddle. A nominally plane ultrasonic wave field is generated normal to the jet axis by a transmitter having a 16 cm square aperture. The scattered ultrasound in the radial direction is measured at a number of streamwise and azimuthal stations. In accord with the theory, the normalized amplitude of the scattered acoustic wave is a linear function of the angular velocity of the swirl generator, and is independent of the intensity of the incident wave field. Fourier components of the uniform vorticity distribution are directly measured by varying the scattering angle and are in good agreement with theoretical predictions.

# III. SUMMARY OF ACCOMPLISHMENTS

## III.1. Fluidic Technology Based On Synthetic Jets

We have developed a radically new approach to the manipulation and control of shear flows using novel fluidic technology based on synthetic jets. These jets have the unique property of being *zero-mass-flux* in nature; i.e., they are synthesized from the working fluid in the flow system in which they are embedded. Although there is no net mass injection into the overall system, the jets allow momentum transfer into the embedding flow. The interaction of synthetic jets and an embedding flow near the flow boundary leads to the formation of closed recirculation regions and thus an *apparent* modification of the flow boundary. *These features enable synthetic jets to effect significant global modifications in embedding flows on scales that are one to two orders of magnitude larger than the characteristic length scale of the jets themselves.* Furthermore, while conventional excitation schemes have been limited to frequency bands tailored to the linear receptivity mechanisms of a given flow, fluidic actuation allows for exploitation of nonlinear mechanisms for amplification of disturbances in a very broad frequency band. These capabilities have been demonstrated in a series of pilot investigations including thrust vectoring and modification of aerodynamic surfaces.

In current implementation of these devices, nominally round or plane turbulent jets are formed in air or water normal to an orifice in a flat plate. These jets operate without net mass injection across the actuator surface and are thus comprised entirely of entrained surrounding fluid and are in effect synthesized by a train of vortices. Each vortex is formed at the edge of the orifice, and is driven by the motion of a diaphragm at the bottom of a sealed shallow cylindrical cavity under the orifice plate. The vortices, and thus the characteristic dimensions of the jets, scale with the characteristic dimension of the orifices. Because the motion of the diaphragm is extremely small and it can be driven at resonance (e.g., by a piezoelectric actuator), the electrical power input to the actuator is typically small (in recent experiments at Georgia Tech, a millimeter-scale synthetic jet actuator was used for thrust vectoring of primary jets that are at least two orders of magnitude larger where the power input of the actuator was several milliwatts).

That jet actuators are synthesized from the working fluid (gas or liquid) in the flow system in which they are embedded obviates the need for input piping and complex fluidic packaging, and makes them ideally suited for fabrication using micromachining techniques. Under support from AFOSR, we have designed, fabricated and tested microjet actuators having orifice diameters of the order of 150 μm (Coe, Allen, Trautman, and Glezer 1994). These actuators can be used to affect macro-scale events in a variety of applications: either

*directly* from the concerted action of a large number of individually controllable microjets (for example, we have demonstrated that a micromachined array of 360 phased jets can generate sufficient thrust to move a suspended, packaged silicon die containing the microjets over an excursion distance of 30 cm); or *indirectly*, by amplifying their control input through a flow system that is used as a fluidic amplifier. This control scheme is particularly attractive for microjet actuators because the energy that is necessary to amplify the control input is extracted from the flow being influenced and, as a result, will allow the implementation of cascaded control. Specifically, that microjets be used in a scaling hierarchy to manipulate millimeter-scale jets which, in turn, will control larger jets.

In the present implementation, nominally round (or plane) turbulent air (or liquid) jets are synthesized by a train of vortex rings (or two-dimensional vortex pairs). The vortices are formed at the edge of an actuator orifice by the motion of a small diaphragm that is driven by a piezoceramic disc and mounted at the bottom of a sealed shallow cylindrical cavity as shown schematically in Figure III.1-1a. During the forward motion of the diaphragm, fluid is ejected from the cavity, the ensuing flow separates at the sharp edge of the orifice, forming a vortex sheet that rolls into a vortex ring that begins to move away from the orifice under its own self-induced velocity (Glezer & Coles 1990). When the diaphragm begins to move away from the orifice, the vortex is already sufficiently removed

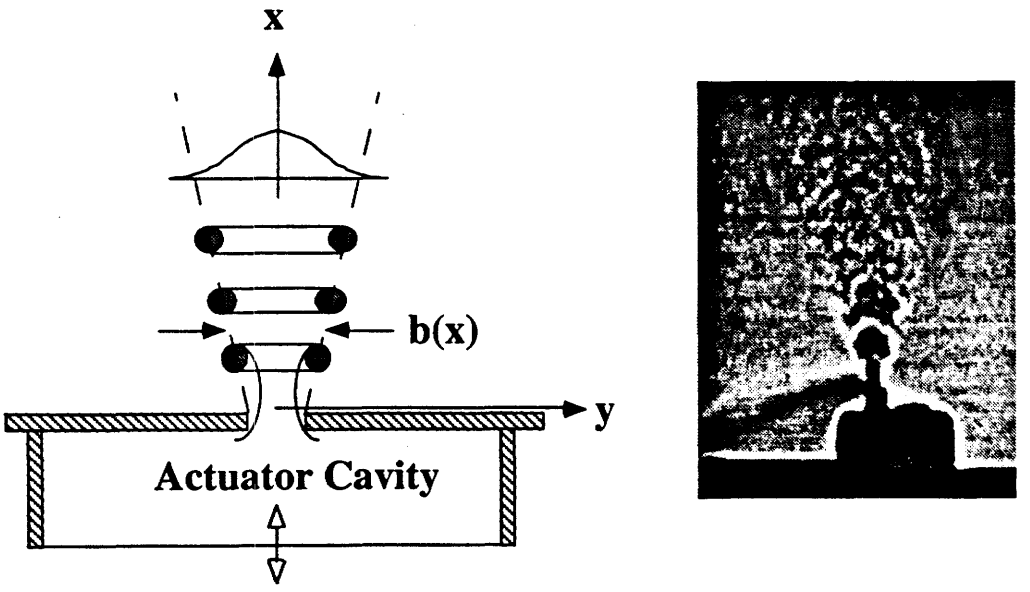


a b

Figure III.1-1

and is thus unaffected by the ambient fluid that is drawn into the cavity. Therefore, during each cycle the net mass flux out of the cavity is zero while the mass and hydrodynamic impulse of each vortex are non zero. The diaphragm is typically driven at resonance (e.g., by a piezoelectric actuator), and thus the electrical power input to the actuator is typically small (in recent experiments at Georgia Tech, a millimeter-scale synthetic jet actuator having a power input of several milliwatts, was used to vector a primary jets that was at least two orders of magnitude larger).

The jet is synthesized by the time-harmonic formation and subsequent interactions of these vortices, and, therefore, its characteristic dimensions scale with the characteristic dimension of the orifice. Thus, it is possible to synthesize jets over a broad range of characteristic cross flow length scales (two-dimensional and axisymmetric orifices have been fabricated in the millimeter and micrometer range). Furthermore, for a given amplitude of the diaphragm motion, the characteristic time scales associated with the period of the oscillations affect the total circulation of cores of individual vortices. The characteristic time scales also affect the response of the jet to changes in the amplitude of the motion of the diaphragm. Figure III.1-1b is a Schlieren image a two-dimensional synthetic air jet having a rectangular orifice that is 0.5 mm wide; it clearly shows a vortex pair formed near the orifice. The image also shows a streak of heated fluid entrained by the jet.

Cross-steam distributions of the streamwise velocity component were measured at a number of streamwise stations downstream from the orifice using hot wire anemometry. These data are plotted in Figure III.1-2a in the usual similarity coordinates and demonstrate that, at least within the streamwise domain of the present measurements, the jet is reasonably self-similar. The streamwise decay of the centerline velocity is shown in Figure III.1-2b. The streamwise decay rate of a conventional plane turbulent jet is also shown for reference. It is noted, however, that details of the flow field near the orifice and of the entrained flow far from the jet cannot be studied with any reasonable accuracy using conventional hot wire anemometry because hot wire sensors cannot resolve velocities below 0.5 m/sec or reversed flows.

Synthetic jet actuators have also been microfabricated using standard silicon micromachining techniques; they consist of an orifice situated atop an actuator cavity which is bounded by a flexible membrane. Typical microjet orifice sizes range from 150-300 microns. Vibration of the membrane using either electrostatic or piezoelectric drive results in a nominally round turbulent air jet formed normal to the microjet orifice. A cross-section of a prototypical microjet in shown in Figure III.1-3. In this design, the orifice and actuator are incorporated into the same wafer. Both electrostatic and piezoelectric drive can

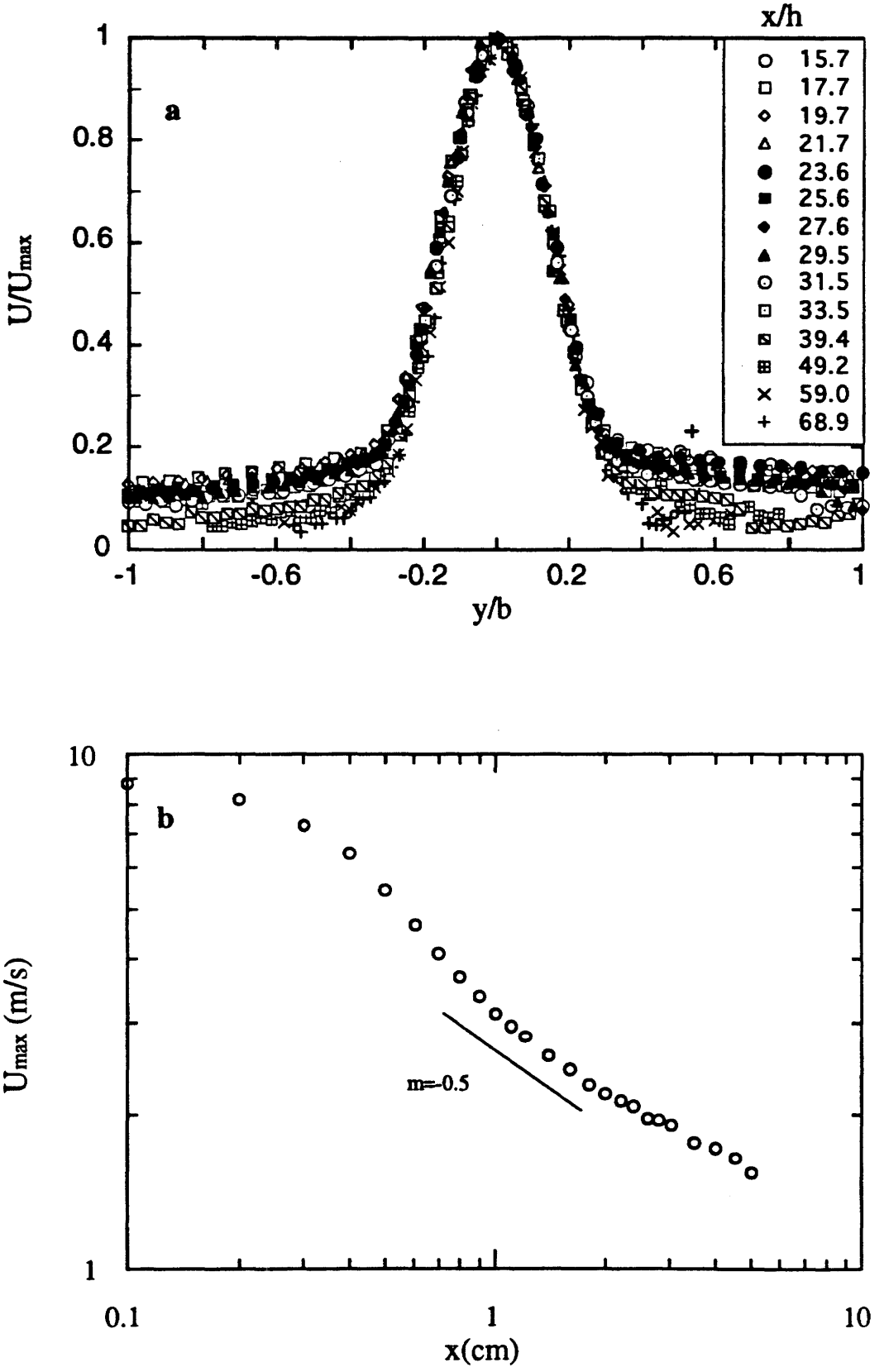


Figure III.1-2

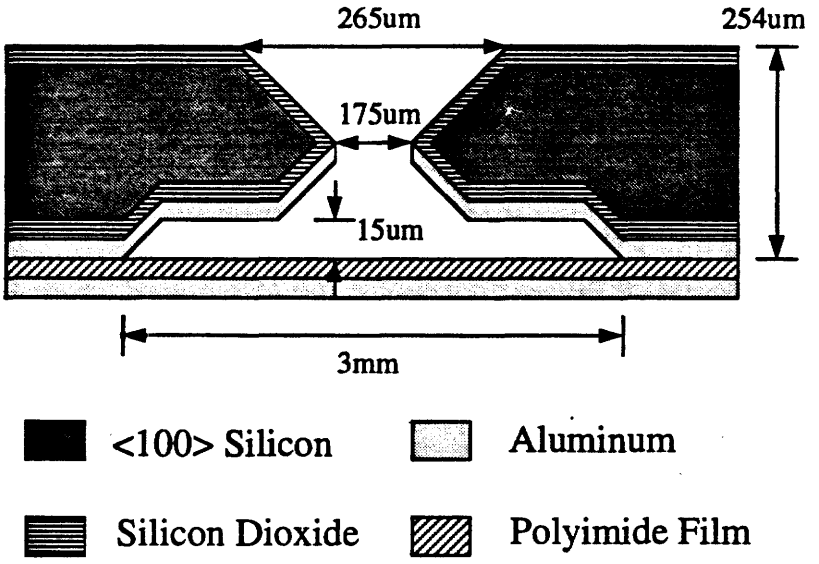


Figure III.1-3

Figure III.1-4

be used in this configuration. Although only a single jet is shown in this configuration, this concept has already been extended to addressable arrays of microjets (Coe, Allen Smith and Glezer, 1995). A smoke visualization photograph of an operational microjet where the smoke is injected radially near the orifice edge is shown in Figure III.1-4. The piezoelectric driver is operated at its nominal 1.3 kHz resonance frequency in its first axisymmetric mode of vibration. The field of view measures 89 mm in the streamwise (x) direction and thus corresponds to nearly 500 jet diameters. The jet appears to become turbulent at or near the orifice, and spreads almost linearly with streamwise diatance. Large coherent vortical structures are apparent in the far field of the jet. Jets with centerline velocities exceeding 20 m/s at a distance of 15 diameters (Re = 1400) have been realized. The Reynolds number of the jet based on the centerline velocity and its width at x/D = 15 is approximately 1400.

## III.2. Vectoring of a High Aspect Ratio Rectangular Air Jet

Eexperiments at Georgia Tech (Smith and Glezer, 1994) have demonstrated that synthetic control jets can effect substantial vectoring of primary jets having characteristic length scales and linear momentum that are at least *two orders of magnitude larger.* In contrast to vectoring by direct impingement of conventional control jets, which is directed away from the jet actuator, vectoring by synthetic jets can be effected *either* towards ("pull" mode) *or* away ("push" mode) from the actuator. Furthermore, a given synthetic jet actuator can operate in either mode by slight adjustment of its streamwise position relative to the primary jet. Although the mechanism by which vectoring is accomplished is not completely understood and is one of the foci of the proposed work, our preliminary work suggests that the vectoring is the result of a Coanda effect along mean streamlines of the combined flow.

The utility of millimeter-scale synthetic jets actuators for thrust vectoring of larger, centimeter-scale conventional has been recently demonstrated by Smith and Glezer (1994). In these experiments, the primary jet emanates from a rectangular conduit measuring 7.62 cm x 1.27 cm. While the lengths of the control jet orifice and the primary jet conduits are the same, the width of the control jet orifice is 25 times smaller. The jet actuator is placed near the exit plane and along the long side of the primary jet and can be rotated so that the angle between their respective centerlines can be continuously varied. In the experiments reported here, the centerlines of two jets are co-linear (Figure III.2-1a), the centerline velocity of the primary jet at the exit plane is 6.5 m/sec, and the ratio of the flux of streamwise momentum per unit span between the control jet and the unforced primary jet is approximately 1/35.

The interaction between the control jet and the primary jet is demonstrated in the Schlieren photographs of Figure III.2-1(b, c). The unforced primary jet is shown for reference in Figure III.2-1b. When the actuator is activated (Figure III.2-1c), the primary jet is vectored upward (i.e., towards the actuator). The vectoring is a result of a Coanda effect resulting from strong entrainment and a low pressure region that are induced by the control jet as shown schematically in Figure III.2-2. Because the control jet entrains ambient fluid on both sides, it appears that its interaction with the primary jet leads to the formation of a Coanda surface along the dividing stream lines between the two flows.

Distributions of the streamwise and cross-stream velocity components were measured using hot-wire anemometry at a number of streamwise stations. Figures III.2-3a and b show profiles of the streamwise velocity component plotted in similarity coordinates for the unforced and vectored jets, respectively. The velocity profiles of the vectored jet in Figure III.2-3b are displaced in y so that the maximum velocity at each streamwise station

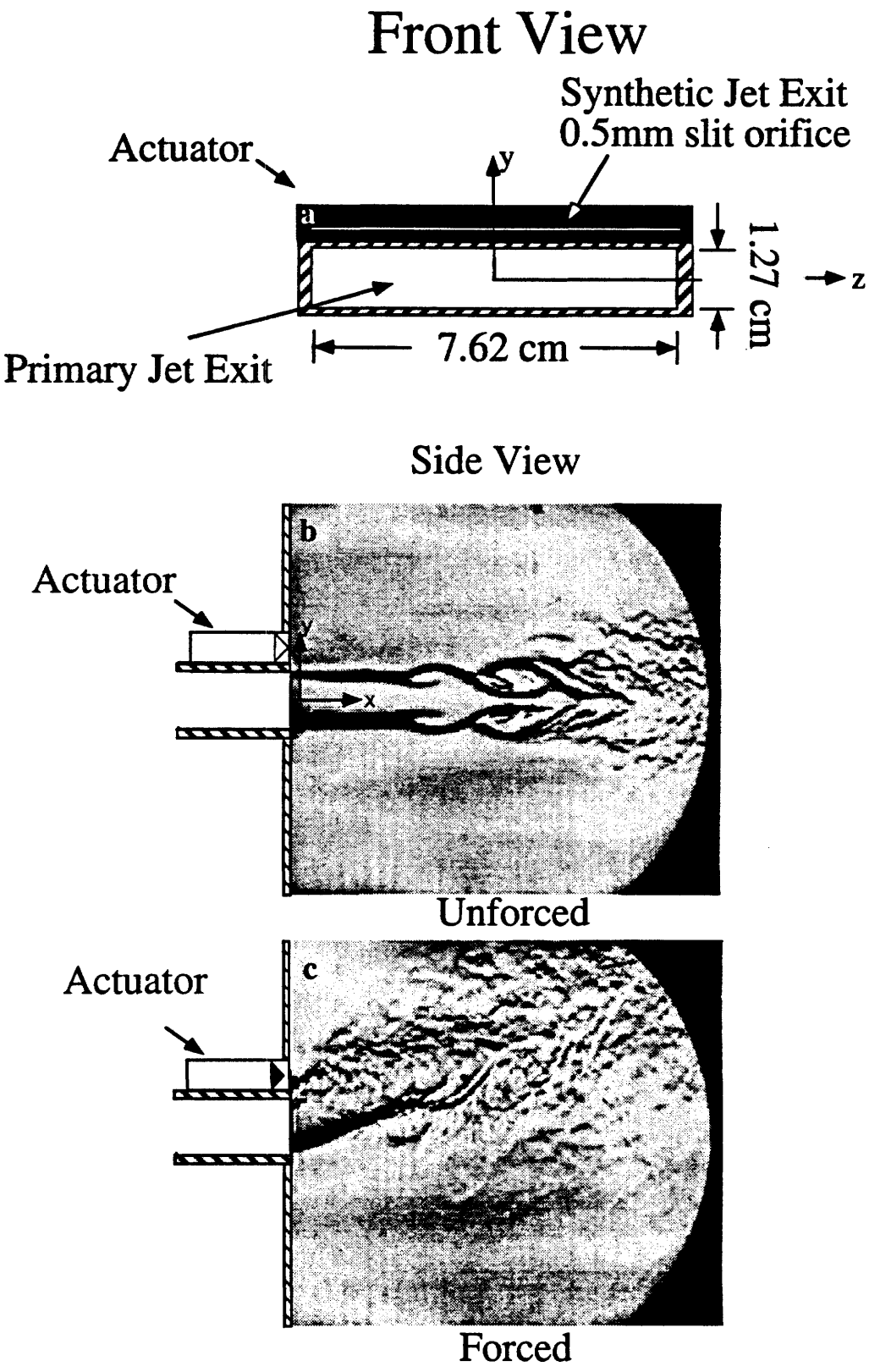


Figure III.2-1

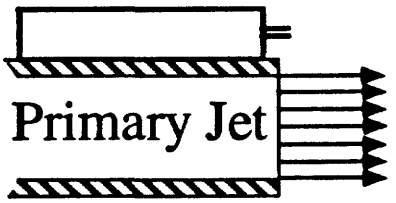


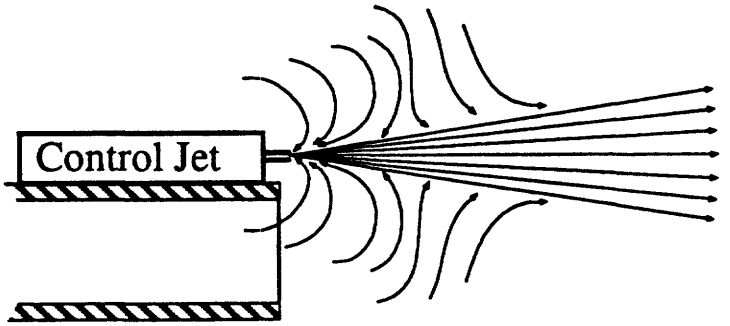


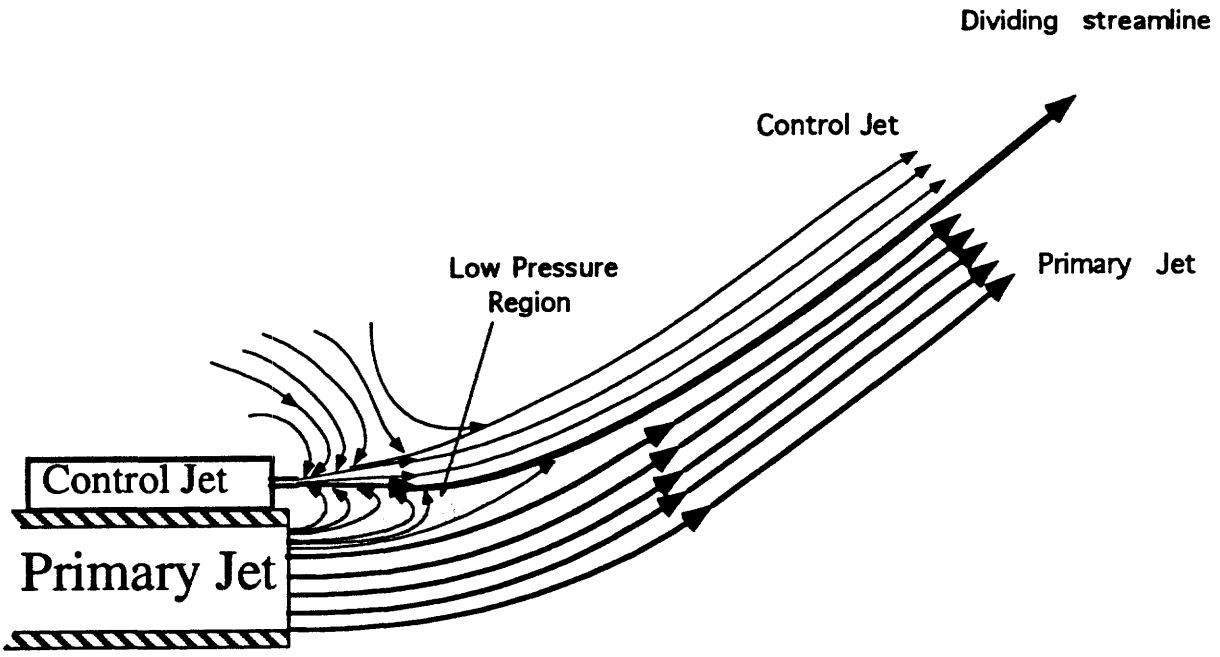


Figure III.2-2

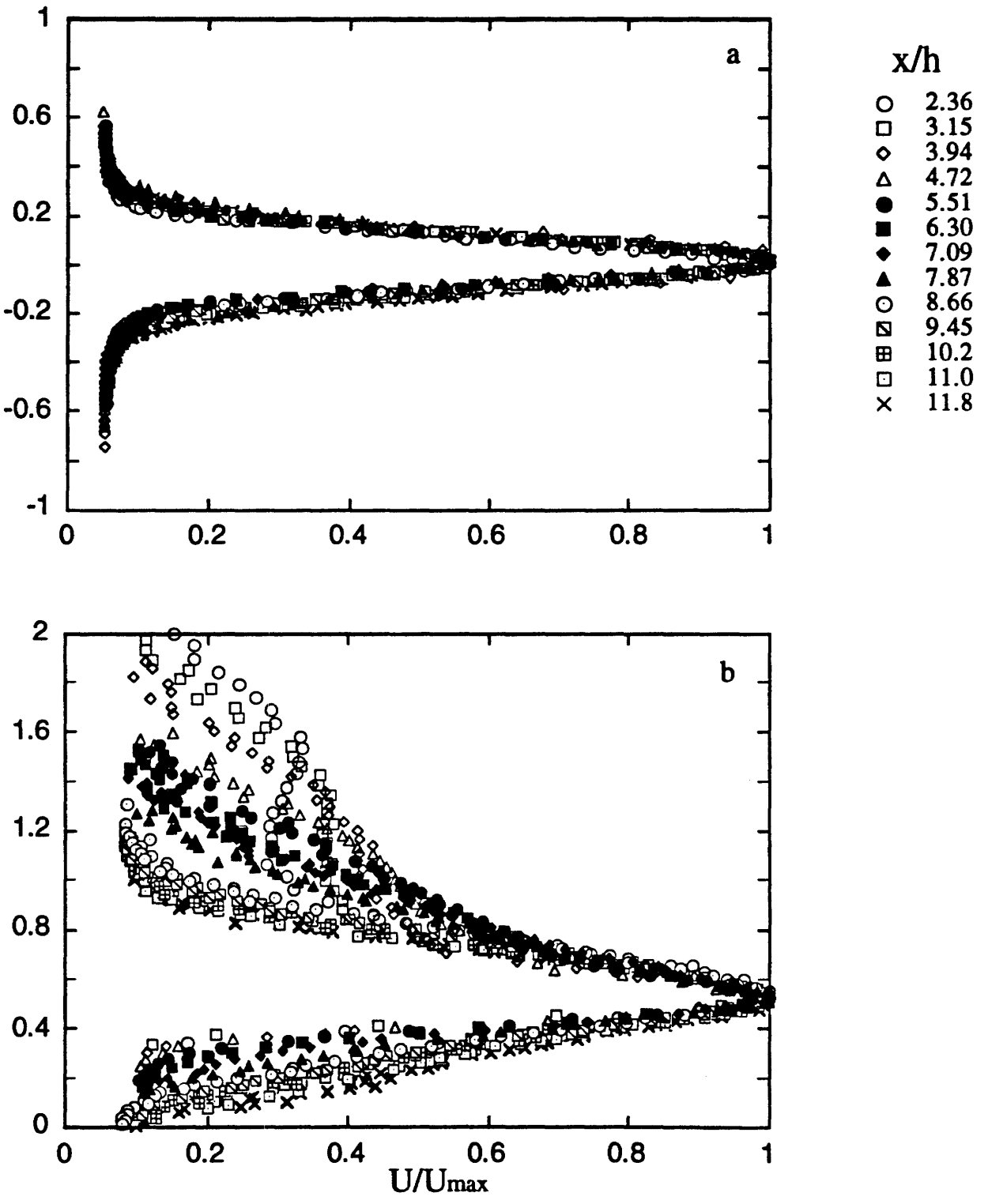


Figure III.2-3

lies at y = 0. [The present data shows that the loci of the maximum streamwise velocity in the x-y plane (x and y are the streamwise and cross-stream directions, respectively) lie on a ray that forms an angle of 28° with the x axis.] These data show that while the vectored jet is nominally self-similar along its unforced side, the forced side becomes self similar farther downstream (x/h > 8.6). This suggests that the vectoring is a near field effect and that once it is completed, the jet remains vectored and becomes self-similar.

The effect of the control jet on entrainment by the primary jet, is assessed from variation of the jet volume flowrate with downstream distance for the forced and unforced cases (Figure III.2-4). The volume flow rate of the unforced primary jet remains almost unchanged until the jet becomes turbulent and entrainment increases. In contrast, the vectored primary jet entrains substantially more fluid and its volume flow rate is over 300% larger than that of the unforced jet. The volume flow rate of the control jet is also plotted for reference and it is noteworthy that the difference in the flow rate between the forced and unforced primary jet is considerably larger than the flow rate of the control jet.

An example of vectoring in the "push" and "pull" modes is shown in Figures III.2-5(a-d). The primary jet is instrumented with a synthetic jet actuator on each side of the flow duct. The unforced jet is shown in Figure III.2-5a for reference. In Figure III.2-5b, only the top actuator is operational. Its orifice approximately coincides with the exit plane of the primary jet and it is operating in the "pull" mode. The bottom actuator is operated in the push mode by placing it so that its orifice is slightly upstream of (i.e., behind) the exit plane of the primary jet. This displacement of the actuator allows the synthetic jet to bend around the duct of the primary jet due to Coanda effect and impinge normal to the primary jet. It is remarkable that entrainment by the synthetic jet is strong enough to enable to bend around the 90° corner of the primary jet duct. The resulting vectoring is shown in Figure III.2-5c and the angle is approximately equal to that of Figure III.2-5b (about 30°). Finally, in Figure III.2-5d, the top and bottom actuators are operating in concert and the vectoring angle of the primary jet exceeds 80°.

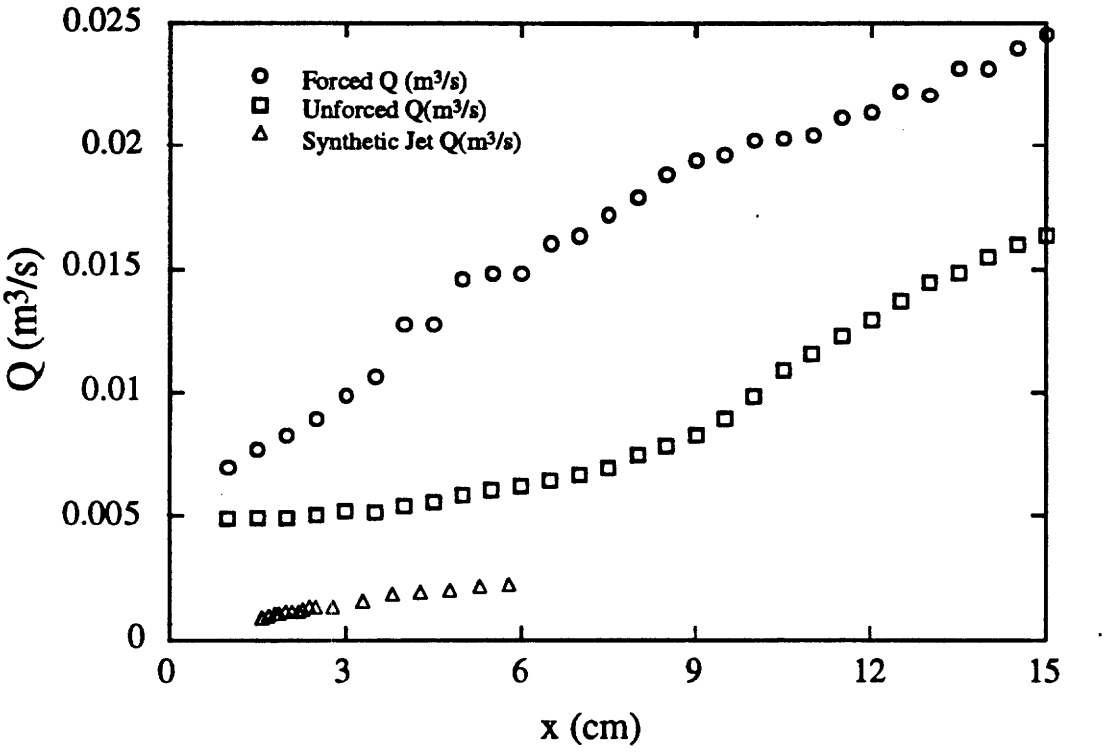


Figure III.2-4

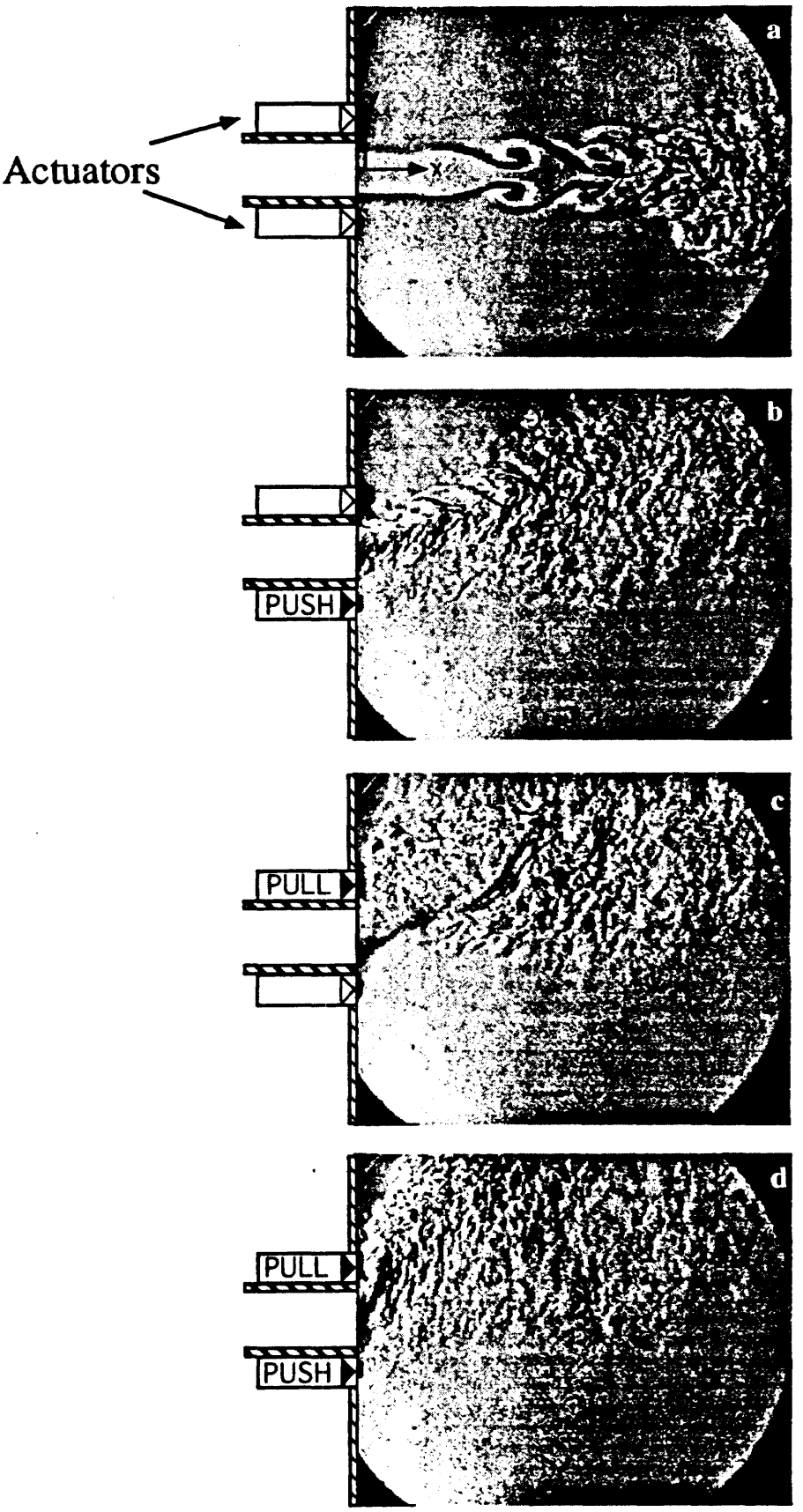


Figure III.2-5

## III.3. Direct Excitation of Small-Scale Motions in Turbulent Shear Flows

While entrainment of irrotational fluid in turbulent shear flows is effected by large-scale motions, molecular mixing ultimately takes place at the smallest scales. In most flows, this mixing is normally induced by a hierarchy of vortical structures. The traditional approach to control of mixing at the small-scale in free shear flows has been *indirect* and has relied on manipulation of global two-and three-dimensional instability modes of the base flow upstream of mixing transition with the objective of controlling mixing through the modification of the ensuing vortical structures (e.g., Roberts, 1985). Because this approach depends on the classical cascading mechanism to transfer control influence to the scales at which molecular mixing occurs, mixing at the smallest scales in fully turbulent flows is only *weakly coupled* to the control input. Clearly, more efficient control of mixing in fully turbulent shear flows might be achieved by direct (rather than hierarchical) control of both the large-scale entrainment *and* the small-scale mixing processes.

We describe below a radically new approach to mixing control, based on concurrent manipulation of *both* the small- and large-scale dynamical processes via direct long-range couplings between large- and small-scale motions in a turbulent shear flow. The concept of long-range interactions between widely disparate scales in turbulent flows (e.g., Yeung, Brasseur & Wang 1995) was demonstrated in the experiments of Wiltse and Glezer (1993, 1994), where small- to large-scale coupling was demonstrated by excitation of discrete wavenumbers within the dissipation range of a jet shear layer, leading to emergence of discrete wavenumbers one to two orders of magnitude smaller.

In the experiments of Wiltse and Glezer (1993, 1994), shear layer segments of a square air jet are forced near the jet exit plane at frequencies within the dissipation range of the base flow by planar, bimorph, piezoelectric actuators driven at resonance. Depending on the forcing frequency, these small-scale motions can have wavenumbers within the dissipation range and within one to two orders of magnitude of the Kolmogorov wavenumber of the base flow, thus enabling one to induce scalar mixing directly at the small scales, without relying on the conventional energy cascade.

In the earlier experiments, the excitation frequency was approximately one order of magnitude larger than the Kolmogorov frequency of the base flow. Figure III.3-1(a-d) shows power spectra of the streamwise velocity component measured with the shear layer of the jet downstream of the actuator. The spectrum of the unforced flow is shown for reference in Figure III.3-1a. In Figure III.3-1b, the flow is forced at the resonant frequency of the actuator (500 Hz) only. We note that although the spectral peak at resonance decays downstream, the excitation results in substantial broadening of the jet shear layer (indicative of enhanced entertainment) and a complete bypass of the natural

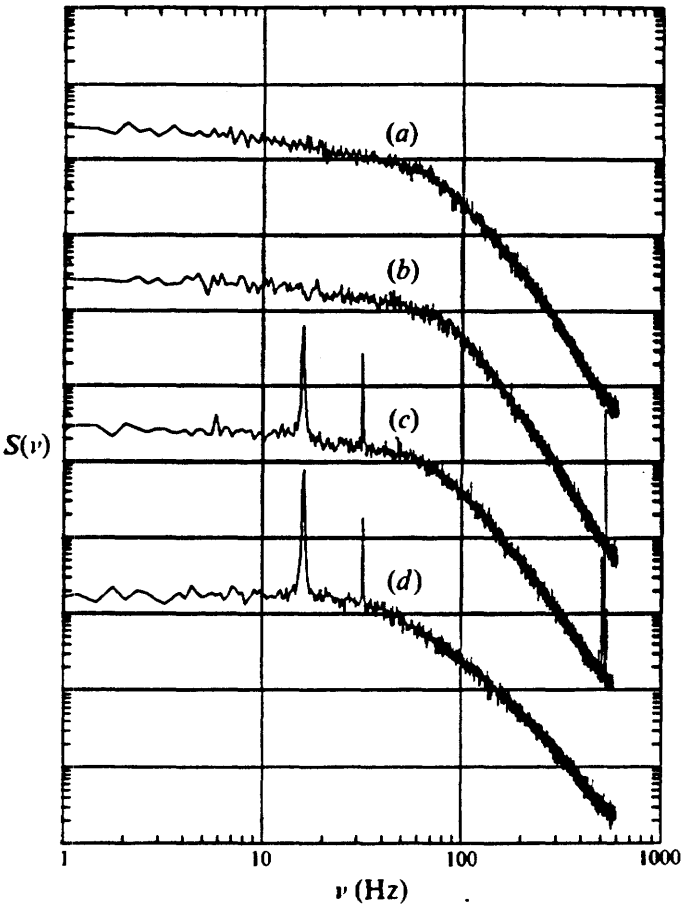


Figure III.3-1

evolution of the fundamental (Kelvin-Helmholtz) instability. The addition of discrete low-frequency sidebands to the excitation frequency by amplitude modulation of the actuator's resonance waveform (III.3-1c) results in interaction that yields low-frequency components at the sideband frequency (and its higher harmonics). This is important since the excitation input is at the high frequencies (high wavenumbers) only, and the appearance of spectral components at low frequencies (low wavenumbers) is apparently due to small-scale interactions within the base flow. The base flow is extremely susceptible to this mode of excitation, and is substantially altered by the appearance of large scale vortical structures accompanied by modification of entrainment and mixing. The large-scale structures persist downstream from the source of excitation and that the high wavenumber end of the spectrum is considerably altered along with the disappearance of the spectral peaks at the excitation frequencies (Figure III.3-1d).

Recent experiments in the same facility have focused on the effect of high-frequency excitation on a shear layer segment of the square jet where the excitation frequency corresponds to the passage frequency $f_K \equiv U_1 / 2\pi\eta$ of eddies at the Kolmogorov scale $\eta$. The Kolmogorov scale (and hence $f_K$) depend on the speed of the mean flow, and since the excitation frequency is limited to the resonance frequency of the actuators (5092.5 Hz), $f_K$ is matched to the excitation frequency by adjusting the jet exit velocity to $U_0$ = 6.5 m/s (the Kolmogorov frequency is close to the actuator frequency throughout the streamwise domain of measurements). The jet is forced using two high-frequency piezoelectric wedge actuators placed along the bottom edge of the square conduit at x = 0.5 cm so that the tip of each blade is aligned with the inner surface of the conduit. The actuators have virtually no effect on the flow when they are not in use. Although the resonance frequencies of the actuators are not precisely identical, they are close enough so that they can be operated in concert at a 5092.5 Hz. The motion of the actuators (maximum peak-to-peak displacement of approximately .27 mm at resonance) is parallel to the jet axis.

Figures III.3-2a-c show profiles of mean velocity U, r.m.s. velocity u', and turbulent dissipation per unit mass $\varepsilon$ for the unforced flow (top) and the excited ($\nu_f$ = 5092.5 Hz) flow (bottom) for x = 1 cm to x = 10 cm in increments of 1 cm. Profiles of the mean streamwise velocity U(y) and the r.m.s. streamwise velocity u'(y) demonstrate that *the mean flow is virtually unaffected by the forcing input.* The primary differences in the forced and the unforced flows is evident at large x, where the shear layer of the forced flow is slightly broader and the peak levels of u' are slightly smaller than in the unforced flow. Figure III.3-2c shows the plots of the time-averaged dissipation $\varepsilon$ for the unexcited (top) and excited (bottom) flow. By contrast to the plots of U and u', there is a substantial increase in the levels of $\varepsilon$ as a result of the forcing. In order to adequately cover the range

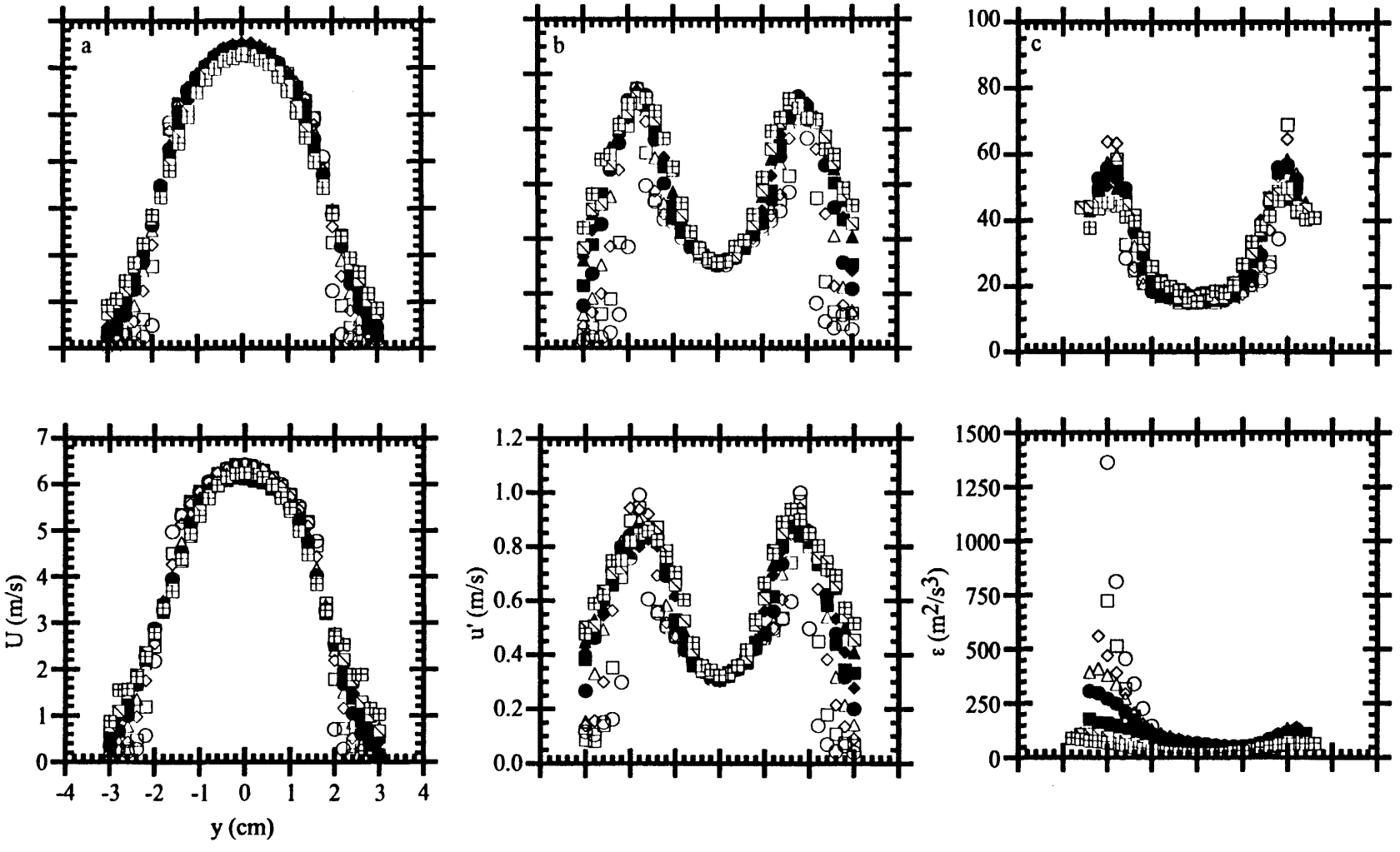


Figure III.3-2

of data, the unforced and forced flows are plotted on different scales. The peak levels of the dissipation decrease significantly with downstream distance. It should be noted that *the levels of dissipation for the forced flow are 1-2 orders of magnitude higher than those for the unforced flow.*

Based on classical notion of the receptivity of shear flows to external excitation, it is expected that the flow will not be receptive to excitation at high frequencies and that the shear layer would attenuate these disturbances as soon as they are introduced. In the present experiments the velocity perturbations (at a peak-to-peak tip displacement of 0.27 mm) is 4.3 m/s and the forcing is introduced through modulation of the mean shear. The effectiveness of the forcing is shown in velocity spectra $S(\nu)$ (Figures III.3-3a-b) of the forced and unforced flow measured at $y = 0$ cm (i.e., where $U(y) = 1/2\ U_0$) at $x = 5$ cm (Figure 8a) and $x = 10$ cm (Figure III.3-3b). Also shown for reference in the log-log plot is a line of slope -5/3. High-frequency excitation introduces a sharp increase in the amplitude of a frequency band centered around the excitation frequency (4000 Hz $\leq \nu \leq$ 7000 Hz at $x = 5$ cm). At $x = 10$ cm, the power at the spectral peak of the excitation frequency decreases by an order of magnitude but is still 4-5 orders of magnitude above the corresponding frequency of the unforced flow. This peak is present in the flow well downstream of the domain of measurement.

The dissipation $\varepsilon$ along the centerline ($y = z = 0$) of the unexcited and the excited flow is shown in Figure III.3-4. (It should be noted that the turbulence in the unforced flow is not quite fully developed: at $x = 10$ cm is $\delta \approx 1.5$ cm and $\Delta U = 6.5$ m/s and thus $Re_{\delta} = 6000$). The excited flow exhibits an increase in dissipation of more than an order of magnitude relative to the unforced flow at the upstream stations. At $x = 4$ cm, the slope (in the log-log plot) for the forced flow becomes more negative. For $x \geq 7$ cm, $\varepsilon$ is a factor of 2 higher for the forced flow than the unforced flow. The slope of $\varepsilon(x)$ appears to reach an asymptotic value approximately the same as that of the unforced flow, that is, $\varepsilon \sim x^{-0.5}$ although at a level twice that of the unforced flow. This trend extends to $x = 10$ cm, the outermost extent of the data.

While the excitation adds energy to the flow at high wavenumbers (or high frequencies), farther downstream there is actually less energy in the flow than in the unforced flow and, furthermore, the transfer of energy from the large scales to the small scales is substantially enhanced. This can be shown by considering the difference in spectral power between the excited and unexcited flow at a given spatial location. Figures III.3-5a-c shows the difference between the power spectra $\Delta S(\nu)$ of the forced and the unforced flow at $x = 1$ cm, 5 cm, and 10 cm, respectively. The difference is normalized by

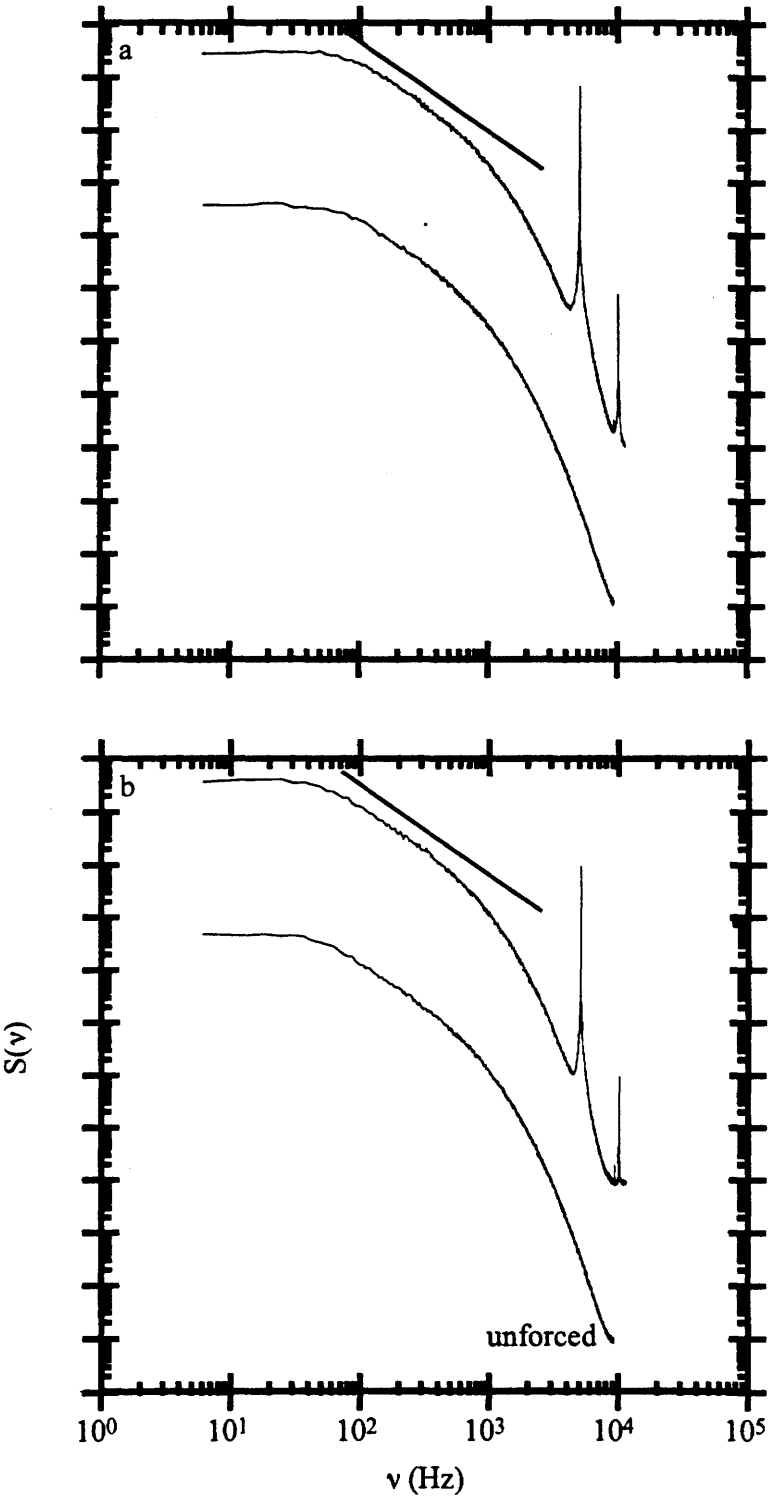


Figure III.3-3

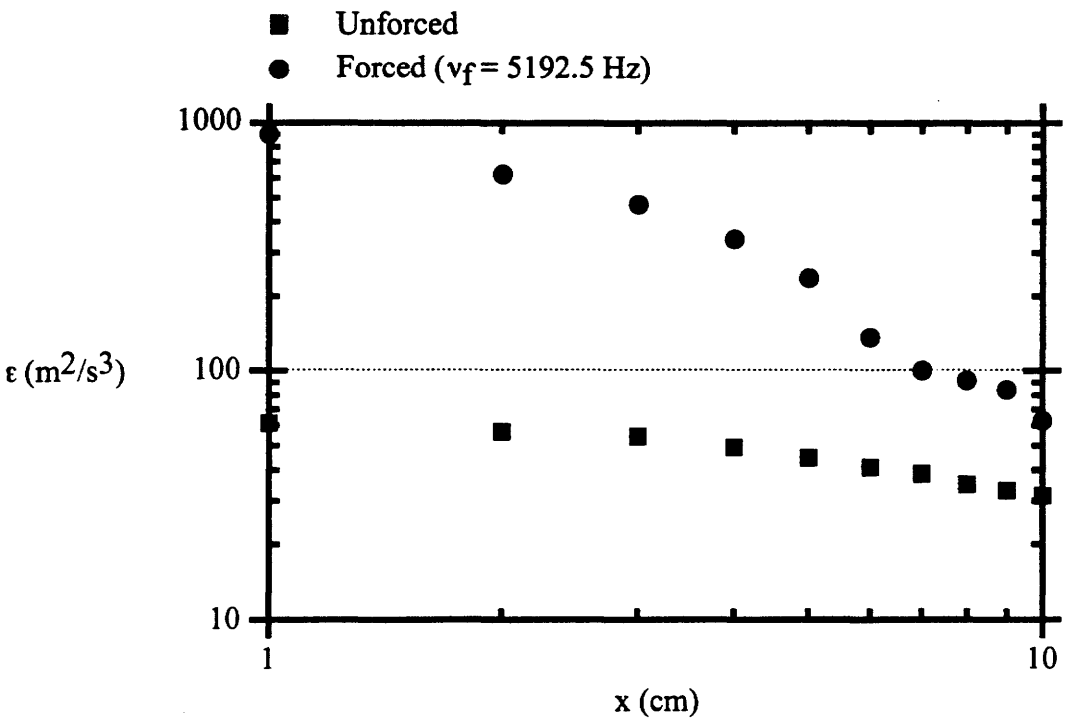


Figure III.3-4

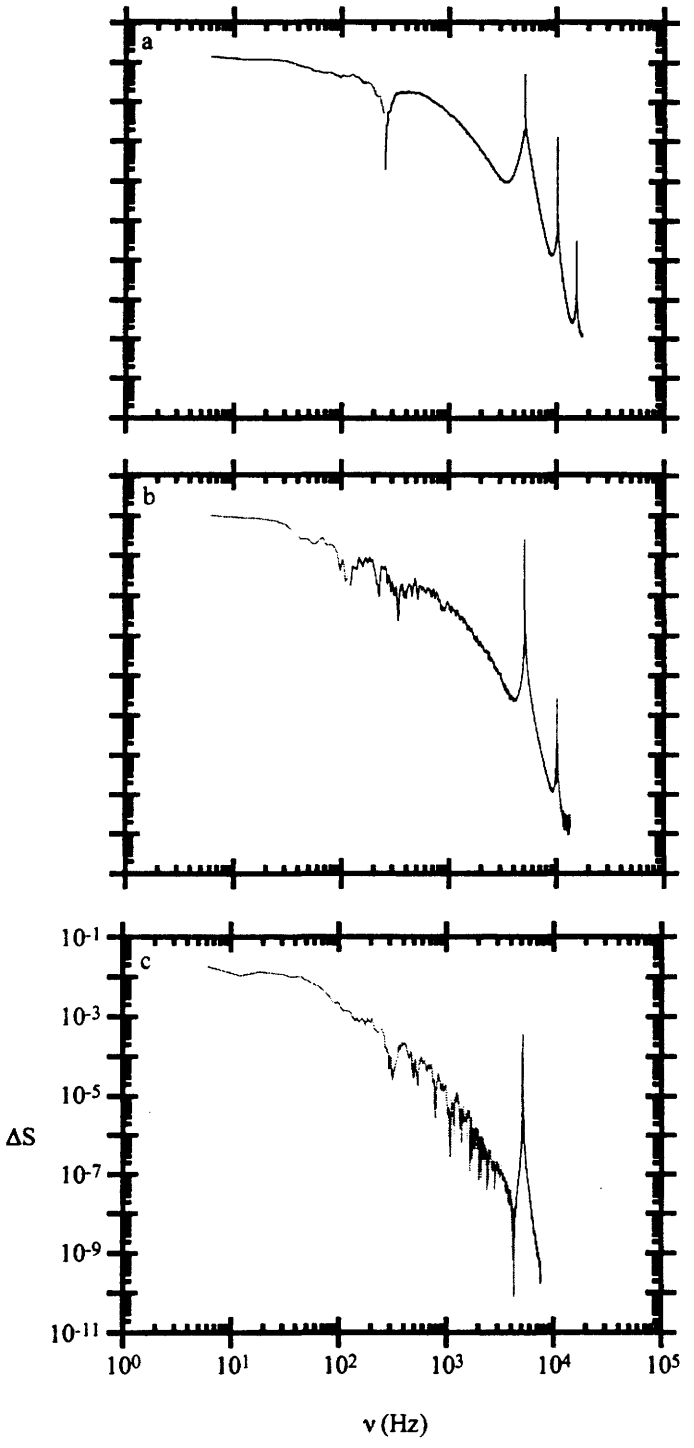


Figure III.3-5

the total unforced spectral power $u'^2$. The black and grey curves represent regions where there is more energy in the forced and unforced flow, respectively.

Immediately downstream of the actuator (figure III.3-5a), there is an increase in power at high frequencies as a result of the forcing. Although the forcing occurs at a discrete frequency (or a discrete wave) of 5092.5 Hz, the spectral power is significantly higher for all frequencies $\nu \geq 230$ Hz in the forced flow. *It is apparent that high frequency excitation alters the turbulent energy cascade.* Typically, the inertial subrange ends (and the slope of the spectrum begins to roll off from m = -5/3) at wavenumbers at which the strain rate is limited by viscosity, at wavenumbers an order of magnitude lower than those corresponding to the Kolmogorov scale. In this case, however, the forcing greatly increases the strain rate so that the roll off of the spectrum occurs at a significantly higher frequency. Figure III.3-6 shows the power spectrum $S(\nu)$ for the unforced and the forced flows at x = 1 cm. Clearly the increase of spectral power at high frequencies shown in figure 14a is attributable to the lengthening of the inertial subrange.

At x = 5 cm (figure III.3-5b), the region in which there is more power in the forced flow is restricted to $f \geq 100$ Hz, while there is less energy at lower frequencies. The magnitude of the positive part of $\Delta S$ is less than at x = 1 cm, however, setting the stage by the attenuation of spectral power further downstream. Finally, by x = 10 cm, there is a decrease in spectral power at all frequencies except those immediately surrounding the forcing frequency. Since for all streamwise stations there is less energy at low frequencies and more energy at high frequencies as a result of the forcing, it is instructive to look at $\nu_{crossover}$, the frequency at which the spectral power in the forced and unforced flows cross. Figure III.3-7 shows $\nu_{crossover}$ as a function of x. The crossover frequency slowly decreases for $2 \text{ cm} \leq x \leq 6$ cm. At this point, $\nu_{crossover}$ rises sharply, signifying the rapid transfer of energy from the large to the small scales, at which point it is dissipated.

Finally, Figure III.3-8 shows the total spectral power (equivalently, the total turbulent kinetic energy) added to or dissipated from the flow as a result of the high frequency excitation which is obtained by integrating the total power in the frequency bands $\nu \geq \nu_{crossover}$ and $\nu \leq \nu_{crossover}$. At upstream locations, the total amount of energy added to the flow in the high frequency region is more than that dissipated from it in the low frequency region. As shown before, the spectral peak introduced by the high-frequency forcing is attenuated by an order of magnitude from x = 5 to 10 cm. This is reflected in the corresponding decrease in the power in the high frequency band ($\nu \geq \nu_{crossover}$). Due to the cumulative effect of the dissipation, the energy in the low frequency band ($\nu \leq \nu_{crossover}$) increases with downstream distance. Figure III.3-7 shows that by x = 10 cm, the total energy dissipated reaches a value of 16% of the unforced turbulent kinetic energy.

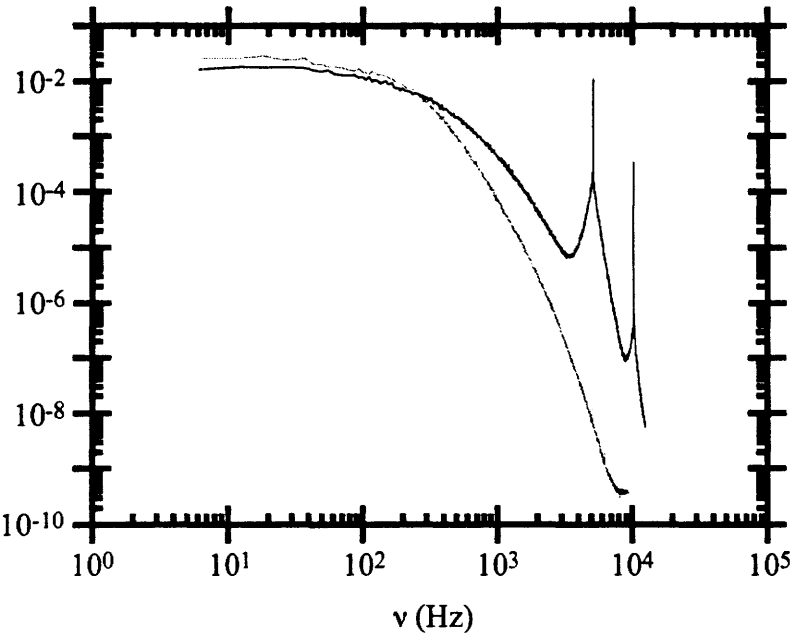


Figure III.3-6

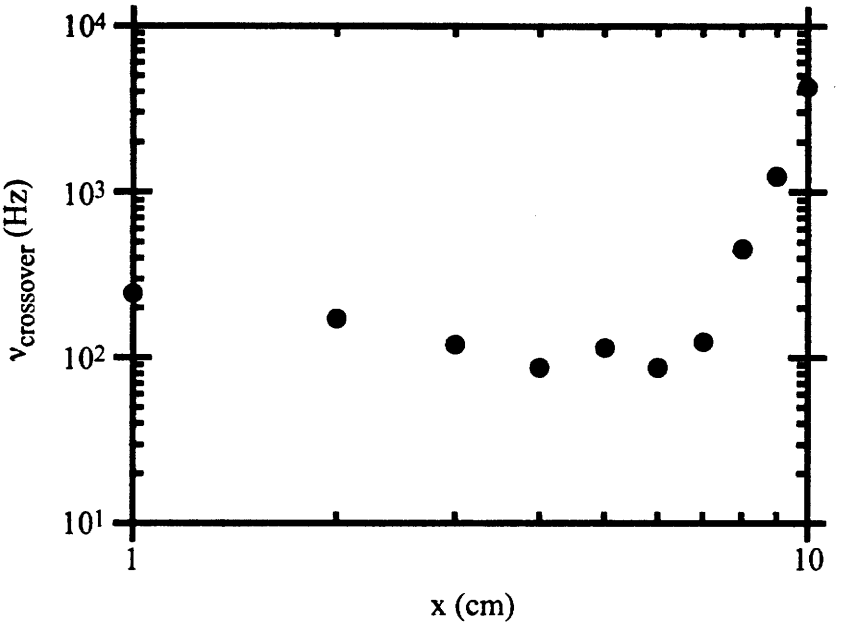


Figure III.3-7

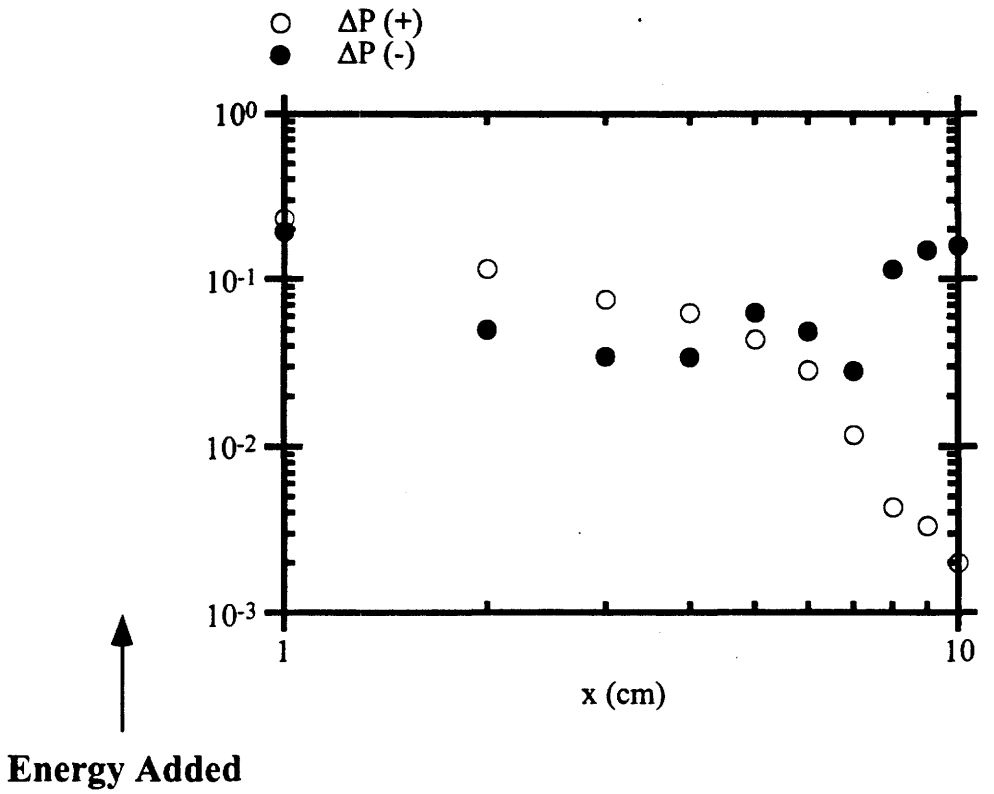


Figure III.3-8

## III.4 Vorticity Measurements Using Ultrasound Scattering

The propagation of sound waves through turbulent flow fields results in phase and amplitude distortions of the wave fronts and wave scattering (e.g., Monin and Yaglom 1980). In the atmosphere, for example, the distortion and scattering of sound waves is primarily effected by variations in the speed of sound due to turbulent temperature and velocity fluctuations and can be analyzed as for electromagnetic waves with proper modification of the medium refractive index. More recently, a new analysis of the scattering of acoustic waves by vorticity concentrations that is based on the framework of classical field theory has been developed by Lund and his co-workers (1989). This analysis makes use of the analogy between the interactions of electromagnetic radiation with charged particles and of sound with vorticity concentrations.

The work of Lund and his co-workers has shown that when a plane acoustic wave of angular frequency $\nu_0$ propagates through a rotational flow field (laminar or turbulent) there is a linear relationship between the Fourier component at a frequency $\nu$ of the scattered acoustic pressure in a given direction $\hat{r}$ and the Fourier transform, in space and time, of the vorticity component that is normal to the plane defined by the wave vectors of the incident and scattered acoustic waves at frequency $\nu - \nu_0$. This means that in principle the amplitude of the Fourier transforms, in space and time, of all three components of the vorticity field can be measured non-intrusively thus suggesting a powerful means for studying vorticity scales and energy cascades between them in various shear flows. Such data are extremely difficult to measure using conventional measurement techniques.

The present experiments are concerned with the scattering of ultrasound from a stationary vortex having a fixed diameter and axial vorticity distribution which is nominally uniform in the inner region of the jet. This vortex forms downstream of the nozzle of a swirling jet and its circulation (and hence the swirl number of the jet) are carefully controlled by the angular velocity of a four-blade paddle that is placed in the jet plenum. The axial (streamwise) and tangential velocity distributions of the jet are measured using X-wire anemometery.

That sound is scattered by vorticity is demonstrated by considering the effect of a plane sound wave on a point vortex whose axis is normal to the wave vector. The passage of the wave induces time-harmonic motion of fluid particles and, in particular, of fluid particles that are on vortex lines. The unsteady vorticity distribution results in far-field pressure fluctuations (Mohring, 1978) that can be interpreted as scattering of the incident sound wave. This fundamental mechanism can be extended to three dimensions and to vorticity distributions in finite domains.

Lund showed that the far field acoustic pressure scattered by the vorticity $\omega$ is

$$p_s(\hat{r},\nu)=\frac{p_0 \nu i\pi^2}{c^2|\hat{r}|}\frac{\cos(\theta)}{\cos(\theta)-1}e^{ik_0|\hat{r}|}\left(\hat{k}_0\times\hat{r}\right)\cdot\tilde{\omega}(\hat{q},\Delta\nu) \tag{1}$$

where $p_0$ is the amplitude of pressure of the incident wave field, $\Delta\nu=\nu-\nu_0$ is the angular frequency difference between the scattered and the incident waves, and $\tilde{\omega}$ is the Fourier transform in space and time of the vorticity. Equation (1) establishes a relationship between $p_{scatt}$ and the component of $\tilde{\omega}$ that is normal to the scattering plane (defined by $\hat{k}_0$ and $\hat{r}$). Equation (1) is valid if the particle velocity induced by the sound wave is small in comparison with the characteristic velocity of the vortical flow, which in turn is supposed to be of low Mach number, and the sound frequency is high in comparison with the inverse of the characteristic time scales of the flow. The experiments reported in the present paper verify the relationship between $p_{scatt}$ and $\tilde{\omega}$ for a uniform distribution of axial vorticity $\omega_0$ within the core of a swirling jet.

The distribution of the mean axial vorticity $\omega$ in cross-stream planes (i.e., normal to the jet axis) is axisymmetric and the scattered pressure in the radial direction at a given streamwise position is determined from

$$\frac{p_s(r,\nu)}{p_0}=\frac{\nu\pi\sin(\theta)h(\theta)}{2c^2r}\int_0^\infty\omega(r)rdrJ_0(qr) \tag{2}$$

and can be computed from a known vorticity distribution.

The jet issues from an axisymmetric round nozzle having an exit diameter $D$ = 2.54 cm and a contraction ratio of 36:1. The swirling generator is a four-blade paddle that is placed in a 15.24 cm cylindrical tube upstream of the nozzle and is rotating about the streamwise (x) axis. Low turbulence level in the plenum is achieved by air filters, honeycomb material, and screens.

The degree of swirl is usually characterized by the dimensionless swirl number $S_W$ which, for a given jet diameter, measures the ratio of streamwise flux of tangential and axial momentum. That is

$$Sw=\frac{2\int_0^\infty UVr^2dr}{D\int_0^\infty\left(U^2-V^2/2\right)rdr} \tag{3}$$

where $U$ and $V$ are the mean axial and azimuthal velocity components.

Previous investigations of swirling jets have employed a variety of swirling generators with varying degrees of effectiveness. The present swirl generator was designed to overcome some of the disadvantages of previous designs (Rose 1962, Chigier and Chervinski 1967, and Sislian and Cusworth 1984). It allows for continuous and repeatable variation of jet swirl number and for easy clockwise or counterclockwise reversal of the swirl. In the present experiments the swirl number was kept below $Sw = 0.4$ in order to avoid the appearance of a minimum of the axial velocity near the jet centerline.

Profiles of the mean streamwise and tangential velocity components ($U(r,x,t)$ and $V(r,x,t)$, respectively) were measured at a number of streamwise stations using an X-wire anemometer probe. Radial distributions of the streamwise and azimuthal velocity components at $x/D = 0.25$, 1, 2 and 3 are shown in each of Figures III.4-1(a, b) ($Sw$ = 0) and III.4-1(c, d) ($Sw = 0.24$). These velocity components are normalized by the jet exit speed $U_0$= 6.1 m/sec in the absence of swirl. Figure III.4-1a shows that in the absence of swirl the streamwise velocity distribution near the jet exit plane resembles a hat-shaped profile with a relatively thin azimuthal shear layer.

As a result of the swirl, there is a noticeable increase in the magnitude of the streamwise velocity near the jet centerline, and in the radial spreading of the jet shear layer (Figures III.4-1c and d). Figure III.4-1d further demonstrate that there is a limited region inside the jet core with a uniform axial vorticity distribution.

While the vorticity within the inner radial domain has the same sign as the angular velocity of the swirl generator, the vorticity in the outer domain is imposed by the stationary flow boundary. The net circulation of each of the axial vorticity distributions $\Gamma = 2\pi\int_0^\infty r\omega(r)dr$ is such that $\Gamma/\Gamma_0 < 0.01$ where $\Gamma_0 = \pi\omega_0 r_0^2$ is the circulation at the exit plane of the jet and $\omega_0$ is the axial vorticity on the jet centerline at $x/D = 0.25$. Figure III.4-2a shows the x-wire vorticity measured at x/D=1.0 and the quality of the least-square fit while Figure III.4-2b shows the circulation calculated from the fit.

A nominally plane ultrasonic wavetrain is generated normal to the jet axis by a Sell-type transmitter (Anke, 1974) that utilizes an electrostatically-driven thin metal-cladded polymeric membrane. The transmitter has a square aperture measuring 16 cm on the side, its frequency bandwidth (within ±5 dB) is 5 to 100 kHz and it is similar to the transmitter used by Baudet, Ciliberto and Pinton (1993). In the present experiments the frequency of the incident wave is $f_0 = \nu_0/2\pi$ = 42 kHz. The scattered ultrasound is measured by a 6 mm-diameter B&K condenser microphone type 4135. Both the microphone and the transmitter are placed on a traversing mechanism and the transmitter is traversed

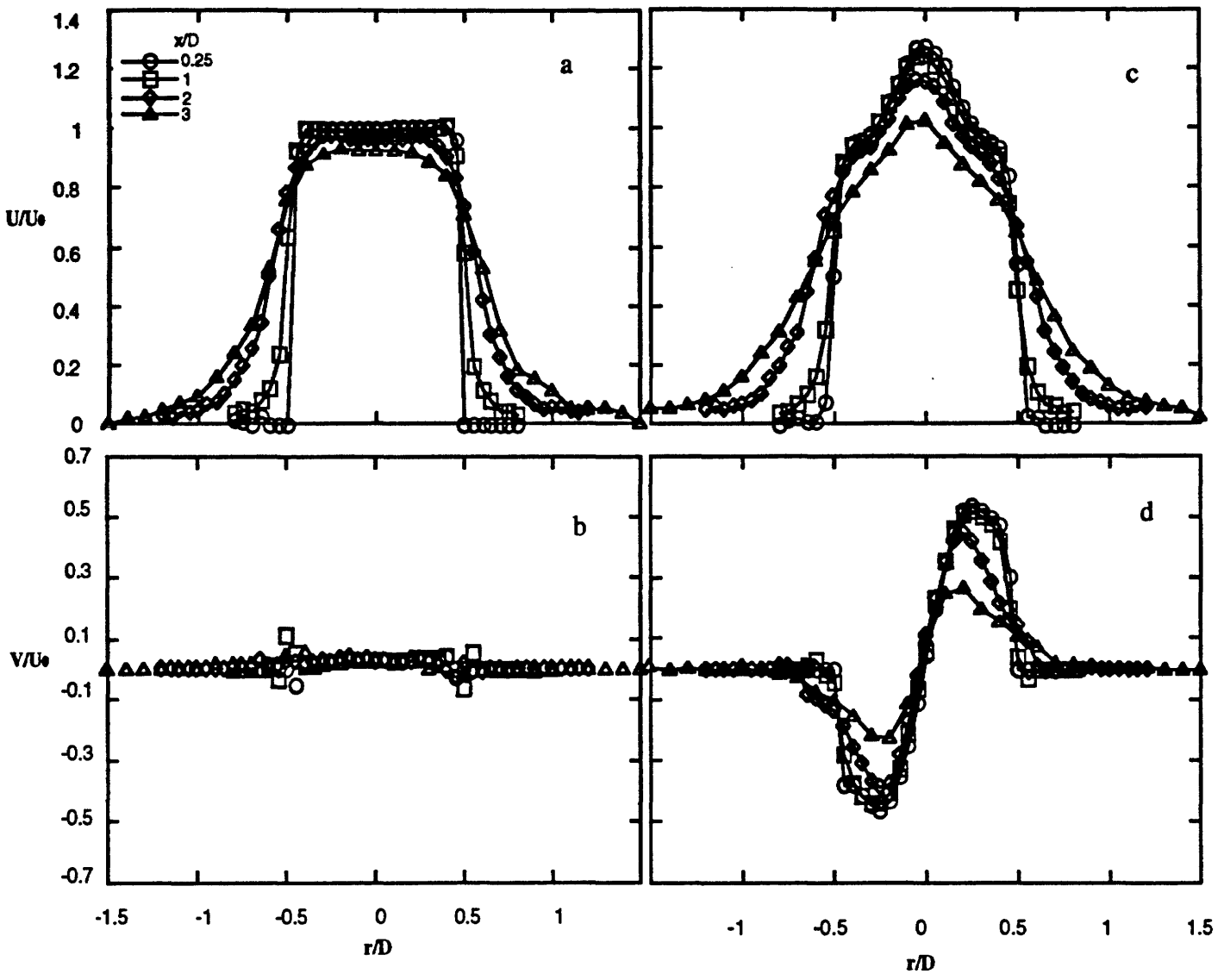


Figure III.4-1

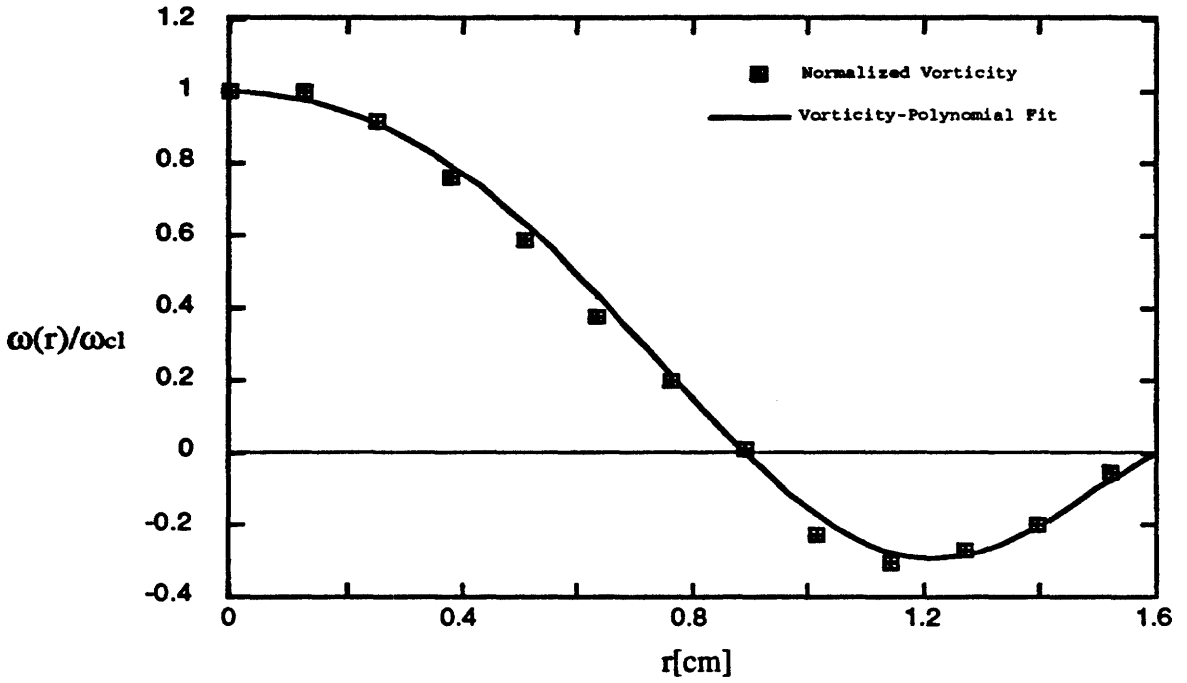


Figure III.4-2a

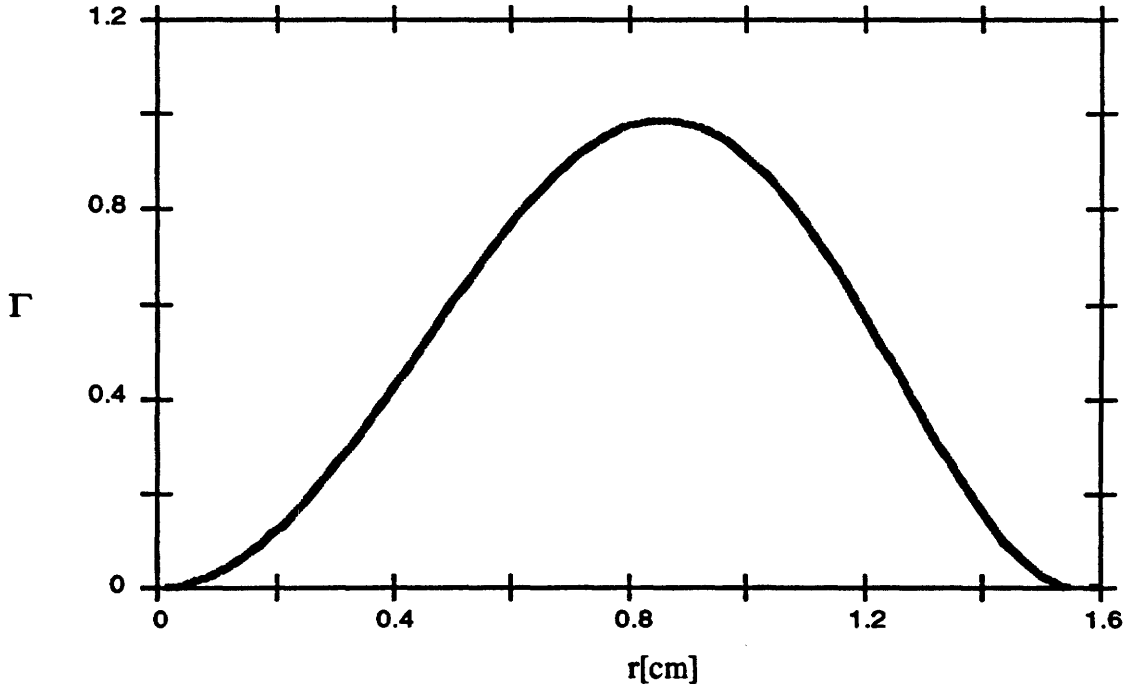


Figure III.4-2b

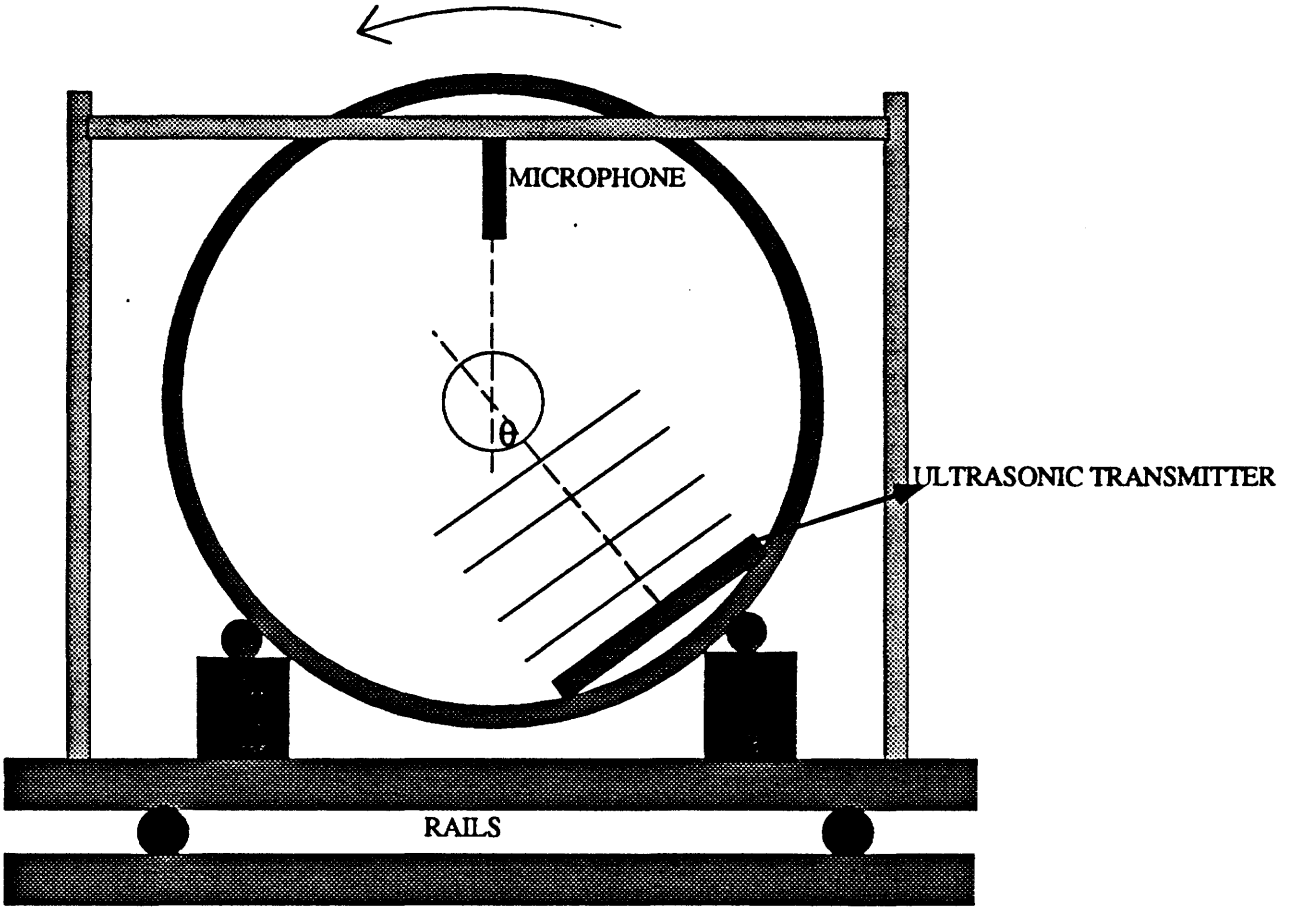


Figure III.4-3

azimuthally ( Figure III.4-3). The normalized directional response of the microphone $\Phi(\varphi)$ is measured at 42 kHz and at 5° increments.

The power spectrum of the pressure field in the absence of swirl $E^{p}_{Sw=0}(f) = |p(f)|^2$ where p(f) is the Fourier Transform in time of the acoustic pressure p(t) is measured at *x/D* = 0.25, *r/D* = 1, and $\theta = 15°$ is shown in Figure III.4-4a.

In the presence of swirl, the measured acoustic pressure is the sum of the incident and scattered acoustic pressures $\Phi \cdot p_i + p_s$.Thus, the normalized amplitude of the spectral peak at the transmitter's frequency $\eta$ is

$$\eta = \frac{|p_s|\cos(\Delta\Psi)}{|p_i|\Phi} \tag{4}$$

where $\Delta\Psi$ is the phase difference between the incident and scattered acoustic pressures

When the swirl is introduced the normalized amplitude of the spectral peak increases or decreases depending on the sign of the swirl. Thus, Figure III.4-4 demonstrate that $E_p(f_0)$ is sensitive to the sense of the swirl and that the increase and decrease in its magnitude are nominally the same (±2.5%) for CW and CCW rotation.

Based on the hot-wire measurements the axisymmetric distribution of the axial vorticity within a cylinder of radius $r_0$ can be represented as follows:

$$\frac{\omega(r)}{\omega_{cl}} = \begin{cases} \omega_p(r) & 0 < r < r_0 \\ 0 & r > r_0 \end{cases} \tag{5}$$

where $\omega_p(r)$ is polynomial fit to the measured x-wire vorticity data and $r_0$ is the radial limit of the vorticity region.

Substitution of Eqn. (5) and (2) into (4) yields

$$\eta = C\frac{h(\theta)}{\Phi(\theta)}(\Phi * (\sin(\theta)\omega(q))) \tag{6}$$

where

$$q = \frac{4\pi f}{c}\sin(\theta/2) \tag{6a}$$

In order to account for the change of $\Delta\Psi$ in calculation of the normalized amplitude of the spectral peak measurements of the difference between incident and scattered waves are performed for $\theta$ between ± 45° for r/D=6.5 ( Figure III.4-7a).

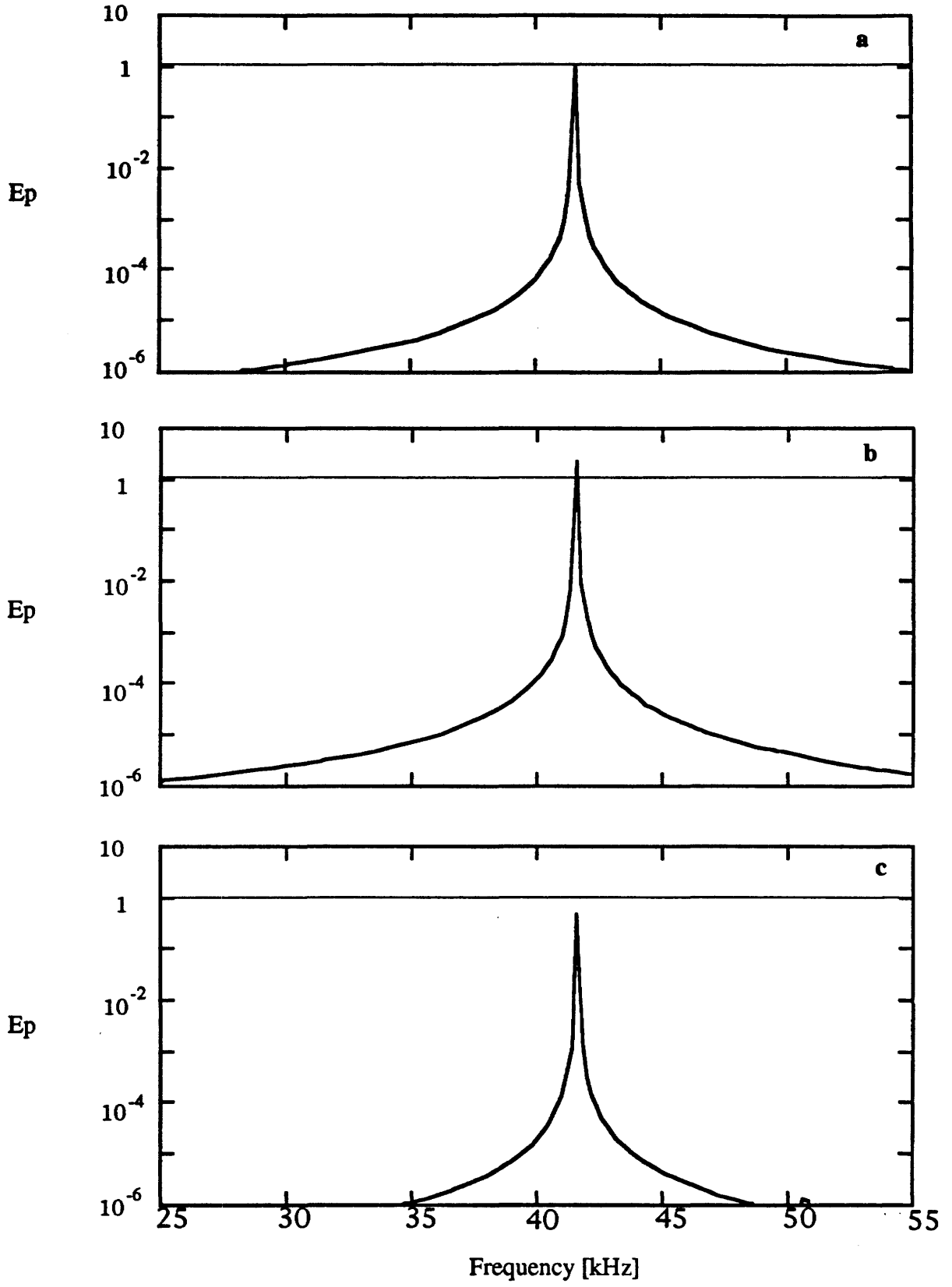


Figure III.4-4

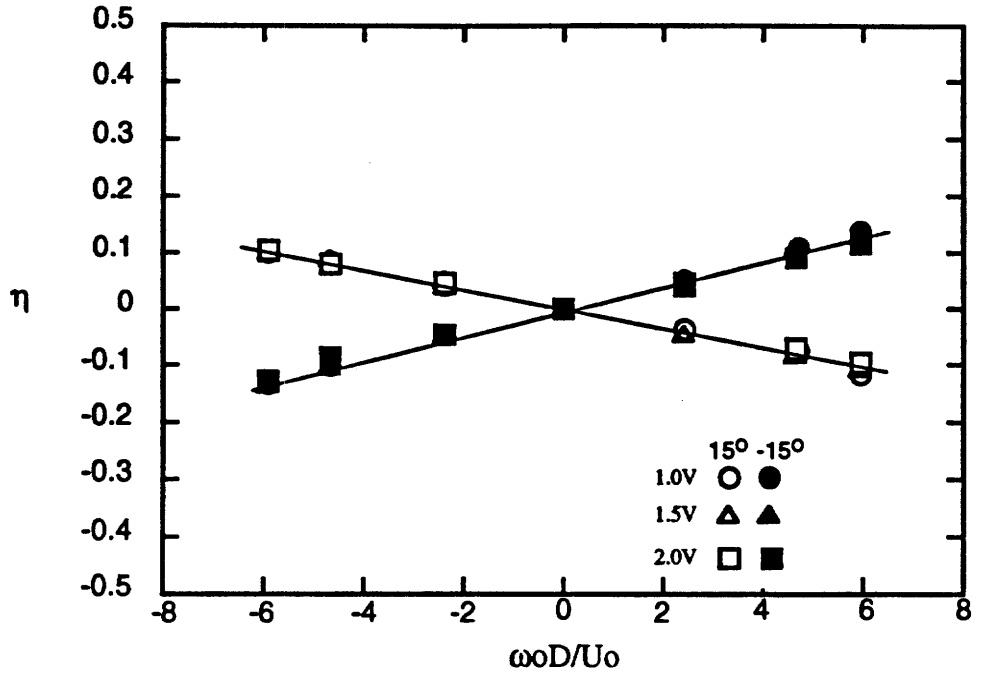


Figure III.4-5

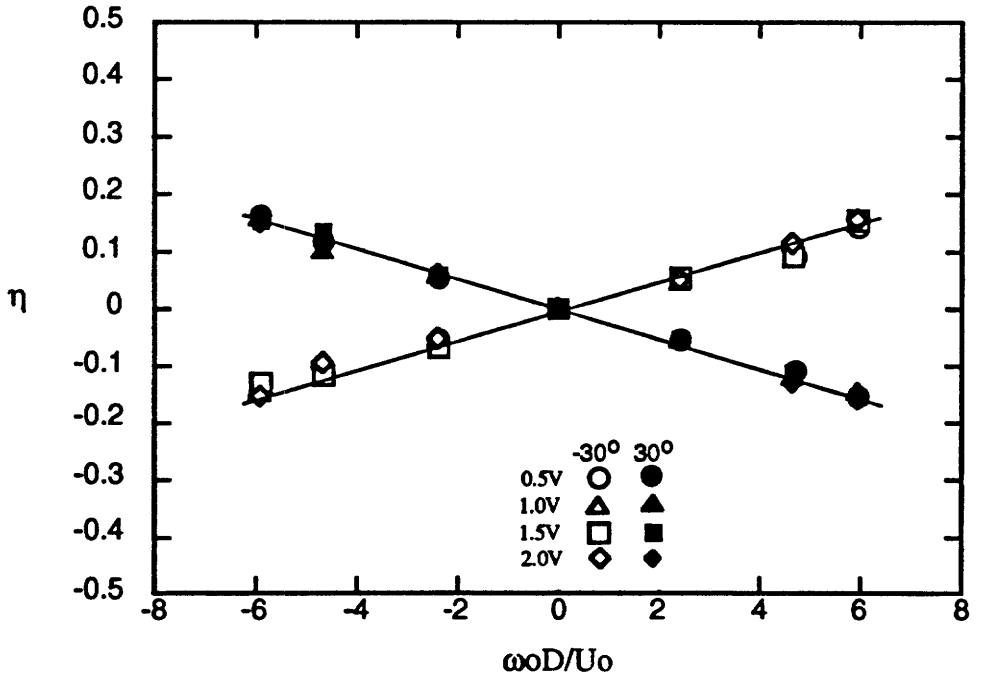


Figure III.4-6

Figures III.4-5 and III.4-6 show that for a given scattering angle ($\theta = \pm 15^0$ and $\pm 30^0$), the normalized peak of the scattered waves $\eta(f_0)$ varies linearly with $\omega_0$, the amplitude of the streamwise vorticity within the core of the jet, and that the slope of this linear dependence, $d\eta(f_0)/d\omega_0$ is independent of the amplitude (or intensity) of the incident wave field.

The hot-wire measurements shown in Figure III.4-1 are used to compare results obtained from the acoustic measurements with x-wire vorticity. The variation of the normalized amplitude of the spectral peak with the scattering angle for $x/D = 1$ and r/D=6.5 is shown in Figure III.4-7b (symbols). The receiver is more than 14 wavelengths away from the jet centerline and the far-field approximation implicit in the theory is justified. Figure III.4-7b shows that $\eta$ is antisymmetric with respect to $\theta$ and that it is positive for $0 < \theta < 14^\circ$ and negative for $15^\circ < \theta < 20^\circ$. The solid lines on Figure III.4-7b is the theoretical result for the normalized amplitude of the spectral peak calculated from the Fourier Transform of the axial vorticity measured by x-wire with the correction for the phase change between incident and scattered waves.

Note that the scattering angle dependence of $\eta$ is very similar for r/D=4.5 and r/D=6.5 indicating that results are becoming independent of the radial distance between the microphone and the jet centerline and that far field approximation can be used. Also note that for small scattering angles $\eta$ varies almost linearly with $\theta$.

It should be noted that because the Fourier transform of an axisymmetric vorticity distribution has no imaginary part, both $\omega(r)$ and $\tilde{\omega}(q)$ are real functions, and the distribution of $\tilde{\omega}(q)$ can be measured, up to one scale factor (which is obtained from the calibration of the receiver), with the present experimental set-up. In order to resolve small enough spatial scales it will be necessary to cover higher wave numbers and higher scattering angles. This we propose to do in a future experiments.

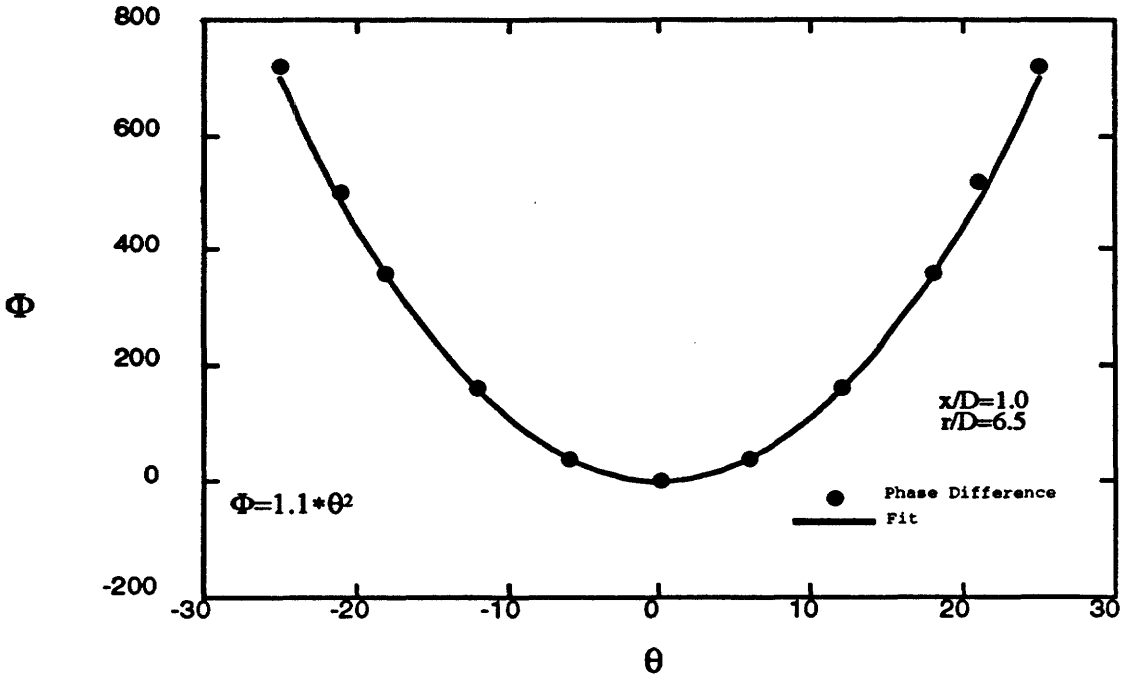


Figure III.4-7a

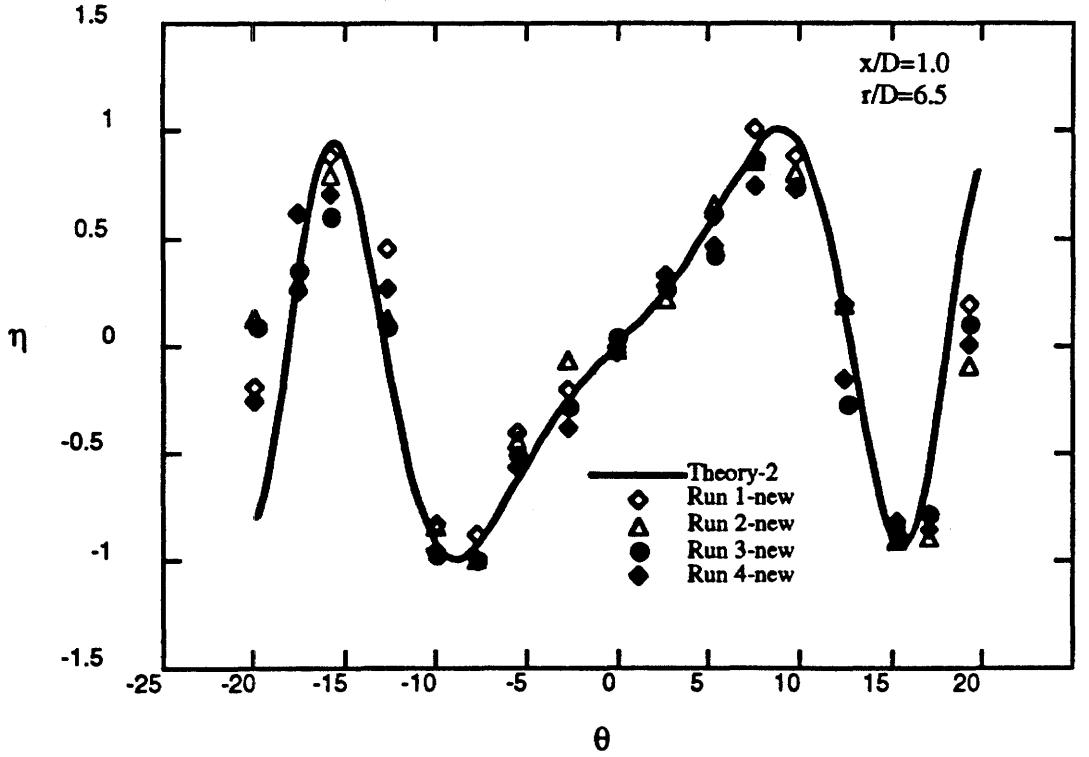


Figure III.4-7b

## IV. LIST OF PERSONNEL

**Faculty:** Ari Glezer

**Post Doctoral Fellow:** John M. Wiltse

**Graduate Students:** Myodrag Oljaca, Barton L. Smith, Mark A. Trautman

## V. LIST OF PUBLICATIONS

1. Gu, X, Lund F., and Glezer, A. "Ultrasound Scattering by a Swirling Jet," submitted to *Physics of Fluids* .

2. James, R. D., Jacobs, J. W., and Glezer, A. "A Round Turbulent Jet Produced by an Oscillating Disk" submitted to *Physics of Fluids* .

# VI. INTERACTIONS AND TRANSITIONS

## VI.1. Collaboration with McDonneell Douglas Aerospace (MDA) on Synthetic Jet Technology

In collaborative research program MDA and Georgia Tech are jointly developing a series of novel actuator concepts for mixing enhancement, thrust vectoring, and aerodynamic shape modification. Based on the research work supported by AFOSR at Georgia Tech, these concepts employ pulsatile zero-mass-flux synthetic jet actuators and cantilevered bimorph piezoelectric actuators. Fluidic actuators are used in the development of vectoring nozzle concepts by exploiting virtual Coanda surfaces for advanced-nozzle plume vectoring, while the piezoelectric actuators are used for mixing enhancement and noise control applications in high-speed flows.

These activities are a part of MDA Active Control Technology Development Program that is aimed at achieving efficient methods for manipulation and control of turbulent shear flows associated in external aerodynamics and propulsion applications. Systems requirements that have driven this work include noise reduction needs of the HSCT, temperature reduction needs associated with the C-17 nacelle redesign program, and, most recently, the intent to replace heavy, mechanically complex advanced fighter engine thrust vectoring devices with fluidic-control based vectoring schemes. MDA was recently awarded a task under the WL FLINT program whose objective is to address the issues of high speed plume vectoring as driven by the needs of advanced nozzle design. The approach intended is to further develop the technology described above to demonstrate the feasibility of vectoring for supersonic flows. The work will consist of a number of cooerdinated activities including investigations of the interaction between the primary and control jets and supersonic jet receptivity experiments, actuator development, design, fabrication and testing.

## VI.2. Other transitions of Synthetic Jet Technology

Thermal management technologies based on microjet cooling to be implemented in single- and multi-chip module packages:

NSF-ERC at Georgia Tech (R. Tummala, Director)

IBM Research Center (Dr. R. Chu)

MICOM (Army Missile Command Mr. P. Black).

## VII. PATENT APPLICATION

Glezer, A. *et al.*, "Synthetic Jet Actuator and Applications Thereof", US Patent Application, **pending.**

## REFERENCES


Anke, D. "Luftschallwandler nach dem Sell-Prinzip für Frequenzen von 50 kHz bis 100 kHz," *Acustica* **30**, 30 (1974).

Baudet, C. , Ciliberto, S. & Pinton, J. F. "Spectral analysis of the von Karman flow using ultrasound scattering," *Phys. Rev. Lett.* **67**, 193 (1991)

Chigier, N. A. & Chervinsky, A. "Experimental investigation of swirling vortex motion in jets," *J. Appl. Mech.* **34**, 443 (1967).

Coe, D.J., Allen, M.G., Smith, B.L. & Glezer, A. 1995 Addressable micromachined jet arrays. *Technical Digest: TRANSDUCERS '95*. Stockholm, Sweden.

Coe, D.J., Allen, M.G., Trautman, M.A. & Glezer, A. 1994 Micromachined jets for manipulation of macro flows. *Technical Digest: Solid-State Sensor and Actuator Workshop*, 243-247

Glezer, A. & Coles, D. 1990 An experimental study of a turbulent vortex ring. *J. Fluid Mech.* **211**, 243-283.

Ho, C.-M. & Huerre, P. 1984 Perturbed free shear layers. *Ann. Rev. Fluid Mech.*. **16**, 365-424.

Lund, F. "Response of a filamentary vortex to sound," *Phys. Fluids A* **1**, 1521 (1989).

Lund, F. & Rojas C. "Ultrasound as a probe of turbulence," *Physica D* **37**, 508 (1989).

Monin, A. S. & Yaglom, A. M. *Statistical Fluid Mechanics*, MIT Press, (1980)

Möhring, W. "On vortex sound at low Mach number," *J. Fluid Mech.* **85**, 685 (1978).

Rose, W. G. "A swirling round turbulent jet," *J. Appl. Mech.* **29**, 615 (1962).

Sislian, J. P. & Cusworth, R. A. "Laser Doppler velocimetry measurements of mean velocity and turbulent stress tensor components in a free isothermal swirling jet," *UTIAS Report*, No. 281 (1984).

Smith, B.L. & Glezer, A. 1994 Vectoring of a high aspect ratio rectangular jet using a zero net mass flux control jet. *Bul. Am. Phys. Soc.* **39**, 1894.

Wiltse, J.M. & Glezer, A. 1993 Manipulation of free shear flows using piezoelectric actuators. *J. Fluid Mech.* **249**, 261-285.

Wiltse, J.M. & Glezer, A. 1994 Small -scale mixing in free shear flows. *Bul. Am. Phys. Soc.* **39**, 1967.

Yeung, P.K., Brasseur, J.G. & Wang, Q. 1995 Dynamics of direct large-small scale couplings in coherently forced turbulence: concurrent physical- and Fourier-space views. *J. Fluid Mech.*. **283**, 43-95.